POLITECNICO
MILANO 1863

SCUOLA DI INGEGNERIA INDUSTRIALE
E DELL'INFORMAZIONE

Laser Powder Bed Fusion (L-PBF) Parameter Optimization for Stainless Steel 316L Porous Microlattices Printing

Tesi di Laurea Magistrale in
Materials Engineering and Nanotechnology

Author: **Erfan Sharghivand**

Student ID: 10698740
Advisor: Prof. Maurizio Vedani
Academic Year: 2022-2023

Acknowledgements

First of all, I would like to express my sincere gratitude to Professor Maurizio Vedani, my esteemed thesis supervisor, for his invaluable guidance, unwavering support, and profound insights throughout the entire journey of my master's thesis. His expertise, encouragement, and constructive feedback have been instrumental in shaping the present quality and depth of this research.

I extend my heartfelt appreciation to my family for their constant love, encouragement, and belief in my abilities. Their continuous support has been my pillar of strength, motivating me to strive for excellence. I am deeply thankful for their sacrifices and understanding during the demanding phases of my academic pursuit.

I would also like to express my gratitude to my friends, Kimia, Mohammad Ali, Sarvenaz, Reza, and Sara for their friendship, motivation, and shared laughter during both the highs and lows of this academic endeavor. Their support and presence have added a meaningful dimension to my time at Politecnico di Milano and helped me pass through the tough times of COVID-19.

Lastly, I extend my thanks to Dr. Marawan Abdelwahed, whose specific contributions have significantly enriched the scope and quality of this research.

This journey would not have been possible without the support, mentorship, and encouragement of the individuals mentioned above. I am truly grateful for the opportunity to pursue my master's degree at Politecnico di Milano, and I carry the gained knowledge and experiences forward into the next chapter of my academic and professional life.

Abstract

Over the last decade, porous metallic microlattice structures have been a fascinating research topic, gaining significant attention as a result of the introduction and recent developments in metal additive manufacturing. This master thesis investigates the Laser Powder Bed Fusion (L-PBF) parameter optimization for the fabrication of stainless steel 316L porous microlattices. Owing to the significant impact of printing parameters on the final product in L-PBF, seven batches of samples were printed and investigated at three different scanning speeds, with two variations of five- and ten-layer repeats in each hatch and two 90° and 45°hatch angles. Employing scanning electron microscopy (SEM) and optical microscopy (OM), the microstructural effects of varying printing parameters were systematically examined, and fractography of compressed samples was used to investigate the distinctions in the failure behavior of these batches. Compression tests, coupled with Digital Image Correlation (DIC) analysis, were employed to assess the impact of printing parameters on the lattice compressive strength. Results reveal that a lower number of layer repetitions, reduced scanning speed, and a 90° hatch angle yield optimal mechanical properties. These parameter combinations enhance microstructural characteristics, reduce porosity, and refine grain structure, contributing to improved compressive strength. The study's findings laid the foundation for further research, offering guidance for designing high-strength microlattices through the alternation of printing parameters. This study is unique in that the manufacturing of the micro-size lattices without a CAD model and directly through the control of the parameters like hatch angle, hatch spacing, and layer repetition are not applicable on an industrial scale, and they became possible because Sharebot, as an AM machine manufacturer and supplier of studied samples, has the ability to produce samples with such alternating parameters.

Keywords: Additive Manufacturing, Microlattice Structures, Laser Powder Bed Fusion (L-PBF), Stainless Steel 316L, Printing Parameters Optimization, Compressive Strength.

Sommario

Nel corso dell'ultima decade, le strutture microreticoli metalliche porose hanno costituito un affascinante oggetto di ricerca, guadagnando notevole attenzione a seguito dell'introduzione e degli sviluppi recenti nella manifattura additiva di metalli. Questa tesi magistrale indaga l'ottimizzazione dei parametri di Laser Powder Bed Fusion (L-PBF) per la fabbricazione di microreticoli porosi in acciaio inossidabile 316L. A causa dell'importante impatto dei parametri di stampa sul prodotto finale in L-PBF, sono stati stampati e analizzati sette lotti di campioni a tre diverse velocità di scansione, con due varianti di ripetizioni di cinque e dieci strati in ciascun passo e due angoli di passo di 90° e 45°. Utilizzando la microscopia elettronica a scansione (SEM) e la microscopia ottica (OM), gli effetti microstrutturali dei vari parametri di stampa sono stati esaminati sistematicamente, mentre la frattografia dei campioni compressi è stata impiegata per indagare le differenze nel comportamento di rottura di questi lotti. Test di compressione, accoppiati con l'analisi di correlazione di immagini digitali (DIC), sono stati impiegati per valutare l'impatto dei parametri di stampa sulla resistenza a compressione del reticolo. I risultati rivelano che un minor numero di ripetizioni degli strati, una ridotta velocità di scansione e un angolo di passo di 90° producono proprietà meccaniche ottimali. Queste combinazioni di parametri migliorano le caratteristiche microstrutturali, riducono la porosità e affinano la struttura granulare, contribuendo a una migliorata resistenza a compressione. Le conclusioni dello studio hanno gettato le basi per ulteriori ricerche, offrendo indicazioni per la progettazione di microreticoli ad alta resistenza attraverso l'alternanza dei parametri di stampa. Questo studio è unico poiché la produzione dei reticoli di dimensioni microsenza un modello CAD e direttamente attraverso il controllo dei parametri come l'angolo di passo, lo spaziamento del passo e la ripetizione degli strati non è applicabile su scala industriale e è diventato possibile grazie a Sharebot, in quanto produttore di macchine additive (AM) e fornitore dei campioni studiati, che ha la capacità di produrre campioni con tali parametri alternati.

Parole chiave: Manifattura Additiva, Microreticolati, Laser Powder Bed Fusion, Acciaio Inossidabile 316L, Ottimizzazione dei Parametri di Stampa, Resistenza a Compressione.

Contents

List of Figures

List of Tables

Acronyms

Variable	Description
AM	Additive Manufacturing
LPBF	Laser Powder Bed Fusion
PBF	Power Bed Fusion
SLM	Selective Laser Melting
SLS	Selective Laser Sintering
DMLS	Direct Metal Laser Sintering
SLA	Stereolithography
EBM	Electron Beam Melting
DED	Direct Energy Deposition
FDM	Fused Deposition Modeling
MJ	Material Jetting
ASTM	American Society for Testing and Materials
LED	Linear Energy Deposition
VED	Volumetric Energy Deposition
BCC	Body Centered Cubic
FCC	Face Centered Cubic
HCP	Hexagon Close-Packed
CAD	Computer Aided Desig
SEM	Scanning Electron Microscope
OM	Optical Microscope
DIC	Digital Image Correlation

Introduction

Nowadays, in the scientific community, additive manufacturing is one of the most frequently used terms. Despite all the limitations, it has absorbed a significant amount of attention in recent years, and many companies and research labs are actively developing AM methods to overcome these limitations and enable industries to utilize AM for mass production. These developments could be classified into two categories: AM hardware, which concentrates on the improvement of printing machines, and AM software, which mainly focuses on the development of AM programming software.

Laser powder bed fusion (L-PBF) previously called selective laser melting (SLM) is one of these AM methods that is known as a metal 3D or powder bed fusion (PBF) printing method that has gained lots of attention in recent years, and huge efforts have been made to industrialize this printing method. Achieving low production costs, high printing speed, high efficiency, and having a final product with satisfying mechanical and surface properties are the aims that have been followed through the continuous development of additive manufacturing in recent years.

One of the fields in which the L-PBF printing method has received considerable attention is metal lattice structure manufacturing. These structures have been studied for many decades, but since the start of AM development, they have been developed in various sectors and became important due to their remarkable high-performance properties, including high strength accompanied by a relatively low mass, considerable acoustic and thermal insulation properties, and great energy absorption. As far as the L-PBF process significantly impacts the resultant properties, like microstructure, porosity, and thickness of the struts, which all affect the mechanical properties, it is important to find the optimal L-PBF parameters. In the available literature that previously studied the L-PBF-produced metal lattice structures, few known powders have been studied: titanium Ti6Al4V powder, stainless steel 316L, and aluminum alloys AlSi10Mg and AlSi12Mg [15, 16, 60].

The purpose of the present study is to take a step in the AM industrialization road by considering all the above-mentioned data and investigating the effect of printing param-

eters on the mechanical properties of stainless steel 316L micro lattices printed through laser powder bed fusion (L-PBF). The importance of this work is that it is one of the most unique and pioneering works on the mentioned topic since it employed printing parameters, such as hatch angle and hatch spacing, as lattice design and manufacturing means, deviating from the conventional use of CAD and STL files. Most of the articles in this field studied the effect of lattice structure or different materials on the mechanical properties of the lattices printed based on the STL-developed files, but in this work, we investigated the effect of scanning speed, number of layers, and rotation angle on mechanical properties of the microlattices produced through the chose of printing parameters. This is what made the current research special and also more difficult because there were not too many articles that could be used as references. To have a more organized report, this work is divided into four chapters.

Chapter 1: State of the art

This chapter provides a literature review of the topics, which is divided as follows:

Part 1.1: Additive Manufacturing:

Additive manufacturing, its history, techniques, limitations and challenges, and future prospects are discussed.

Part 1.2: Laser Powder Bed Fusion (L-PBF):

This part discusses Laser Powder Bed Fusion (L-PBF) in more detail, including its principles, applications, and limitations.

Part 1.3: Lattice and Porous Metallic Lattice Structures:

This part studies the lattice structures, including their progress, development, design, and properties, with a special focus on their production drawbacks and benefits through L-PBF additive manufacturing.

Part 1.4: Stainless Steel:

This part discusses stainless steel, and its properties, and reviews the recent literature on using stainless steel 316L in additive manufacturing.

Chapter 2: Methodology

Part 2.1: Materials:

The powder characteristics and the design approach that has been used for the understudy lattice production are clarified in this part.

Part 2.2: Sample Preparation:

A comprehensive explanation of the employed steps in sample preparation for further analysis is reported.

Part 2.3: Characterization Tests:

A detailed explanation of the characterization methods and utilized equipment have been described.

Chapter 3: Results and Discussion

All the acquired data from the operated experiments are presented in this part, and an interpretation of the results is presented. In order to have a more focused and organized presentation of the data, the chapter has been divided into three main sections, as follows:

Part 3.1: As-Build Samples: Dedicated to the acquired OM, SEM, and EDS results from the as-built samples

Part 3.2: Compressed Samples: Dedicated to the OM, SEM, and the acquired stress-strain graphs from the employed compression tests

Part 3.3: Digital Image Correlation (DIC): dedicated to an extensive report of acquired results from the DIC analysis operated on compression tests.

Chapter 4: Conclusion

A conclusion on the question of the thesis about the optimal printing parameters to get the best mechanical properties is responded to in this part.

1 | State of the art

1.1. Additive Manufacturing

Introduction

In the past few decades, there has been a revolutionary movement in manufacturing that is altering industries and redefining the possibilities of design and production. This driving force is known as additive manufacturing (AM), a technology that has received a lot of attention and investment in recent years. As we start on our trip through the state of the art in additive manufacturing, it is critical to set the stage and provide the framework for our study.

This chapter serves two objectives. Firstly, it provides a comprehensive review of the current state of additive manufacturing. In today's technology world, where innovation moves at a rapid pace, understanding the state of the art is critical for academics and researchers. Since it lays the groundwork for our thesis, it provides the background and knowledge basis that are required to confront challenging issues and contribute to the advancement of this field.

Secondly, understanding the present status of additive manufacturing is critical to our thesis. It provides us with insights into the field's strengths, weaknesses, opportunities, and problems. This knowledge enables us to develop research questions and hypotheses and identify areas where our contribution can make a meaningful impact. Investigating what has been accomplished and what challenges remain can reveal the path that should be followed in our research to provide a suitable impact on the goal area.

The following outline provides a complete overview of what will be presented in this chapter:

1. History of Additive Manufacturing: This section includes a brief recap of how additive manufacturing has evolved, from its early beginnings to its current state.

2. Additive Manufacturing Technologies: This section provides a comprehensive look at

the different AM technologies. Each technology has been studied in detail, including its fundamental work principles, exclusive properties, applications, materials, benefits, and limitations.

3. Challenges and Limitations in Additive Manufacturing: Aside from all the benefits and drawbacks that are mentioned for each additive manufacturing, this part discussed the main fundamental challenges that AM technology has been facing in recent years.

4. Future Directions and Development Trends in Additive Manufacturing: The first part of this chapter will conclude with a look into the future of additive manufacturing, where the upcoming technologies, prospective trends, and the role of additive manufacturing in the industry are discussed.

Following the outlined topics for this section will provide us with a comprehensive review of the state of the art in additive manufacturing, gathering insights, information, and knowledge that will shape the present thesis frame as our contribution to this dynamic area with these primary subjects.

1.1.1. History of Additive Manufacturing

Conventional manufacturing limitations have for decades restricted design engineers' innovation. Truly ideal designs were unable to be manufactured; instead, they were substituted with designs that adapted to the production capabilities of the time. These production restrictions have recently been dramatically reduced as a result of advances in additive manufacturing (AM) [15, 56].

The roots of additive manufacturing may be traced back to the 19th century when AM-like technologies laid the foundation for modern AM technologies [2, 3]. However, the 20th century witnessed significant advancements in AM technologies. Emanuel Sachs and his colleagues at MIT invented and popularized 3D printing (3DP) technology in 1939, which used computer-controlled systems to build wax models layer by layer. While this technique provided the groundwork for additive manufacturing, it was mostly used for prototyping and did not receive widespread attention [44].

As we moved into the 1980s and 1990s, the promising potential of this new technology was quickly realized, and patents began to be filed in this area. Charles Hull, widely considered one of the founding fathers of modern AM, invented stereolithography (SLA) in 1987, which includes utilizing UV light to solidify photopolymer resin layer by layer, producing three-dimensional objects. This development indicated the beginning of commercial AM

technologies and initiated the exploration of their applications across industries [19].

Marshall Burns introduced "automated fabrication" (Autofab) as an AM-like technology in the early 1990s [14]. Afterward, two other revolutionary AM technologies emerged. First, Carl Deckard and James Beaman invented selective laser sintering (SLS) at the University of Texas in 1992, which included utilizing a laser to sinter powdered materials layer by layer to form a net structure. Therefore, SLS opened up possibilities for printing with a variety of materials [15, 23].

Later, on the other hand, Scott Crump invented fused deposition modeling (FDM). For the production of the objects, FDM technology extrudes thermoplastic material layer by layer. This technique proved to be highly adaptable, and it is now employed in both professional and consumer-grade 3D printers [8]. Hull and Crump used these patents to launch 3D Systems and Stratasys, two companies that continue to dominate the polymer 3D printing market today.

At the beginning of the twenty-first century, industries began to understand the potential of additive manufacturing, which is its ability to construct complex structures that cannot be manufactured by using traditional processes and is game-changing for rapid prototyping, customized manufacturing, and even mass production [45]. Researchers, designers, and engineers from multiple fields began to investigate the potential of additive manufacturing (AM) and build novel solutions for the conventional limitations of AM. After which the most efficient and powerful AM technologies developed, methods like Laser powder bed fusion (L-PBF) were introduced, and the range of additive manufacturing materials broadened [15]. Companies like SLM Solutions, 3D Systems, Stratasys, EOS, and others became pioneers in AM commercialization.

To summarize, the history of additive manufacturing has been a developing adventure, and the route to modern AM is marked by creativity and persistence. These mentioned foundational inventions set the path for the diverse and dynamic field of additive manufacturing that we see today.

1.1.2. Additive Manufacturing Technologies

The general term additive manufacturing (AM) refers to a group of innovative manufacturing technologies that are defined by the American Society of Testing and Materials (ASTM) as "the process of joining materials to make objects from 3D model data, usually layer upon layer, as opposed to subtractive manufacturing methodologies; synonyms: 3D printing, additive fabrication, additive process, additive techniques, additive layer manufacturing, layer manufacturing, and freeform fabrication." [40]. AM techniques have been

invented and developed since the initial introduction of this method, and according to the ASTM, the range of AM technologies is classified into several categories, as indicated in Figure 1.1: binder jetting, material jetting, direct energy deposition, sheet lamination, material extrusion, powder bed fusion, and vat photo-polymerization. [6, 40, 43].

This section investigates the mentioned AM technologies, detailing their types, history, inventors, applications, restrictions, and developments. It is critical to comprehend the mentioned details in order to choose the optimal technique based on the desired application and properties. Furthermore, since this study is in the metal additive manufacturing field, the AM techniques that mainly employ polymers or materials other than metal will not be fully addressed in this section, and just a brief overview will be provided.

Process categories	Technology	Materials
Binder Jetting	3D Printing Ink-jetting S-Print M-Print	Metal Polymer Ceramic
Direct Energy Deposition	Direct Metal Deposition Laser Deposition Laser Consolidation Electron Beam Direct Melting	Metal: powder and wire
Material extrusion	Fused Deposition Modeling	Polymer
Material Jetting	Polyject Ink-jetting Thermojet	Photopolymer Wax
Powder bed fusion	Selective Laser Sintering Selective Laser Melting Electron Beam Melting	Metal Polymer Ceramic
Sheet lamination	Ultrasonic Consolidation Laminated Object Manufacture	Hybrids Metallic Ceramic
Vat photopolymerization	Stereolithography Digital Light Processing	Photopolymer Ceramic

Figure 1.1: AM techniques ASTM classifications (2012) [40].

Material Extrusion Techniques

There are a few well-known AM techniques based on material extrusion, such as Robocasting for the manufacturing of complex ceramic components. However, fused deposition modeling (FDM) is by far the most prevalent extrusion-based AM method that was invented and patented in 1989 by Scott Crump the founder of Stratasys, USA [8, 37] The FDM technique, in its physical principles, is quite comparable to that of the hot glue gun and is relatively easy. This technique uses a heating chamber to liquefy polymer that enters the system as an extruded filament. The filament is pushed and driven through

a nozzle of decreased diameter and then deposited layer by layer on the construction platform, as shown in Figure 1.2 that depicts the core idea of FDM [6, 53].

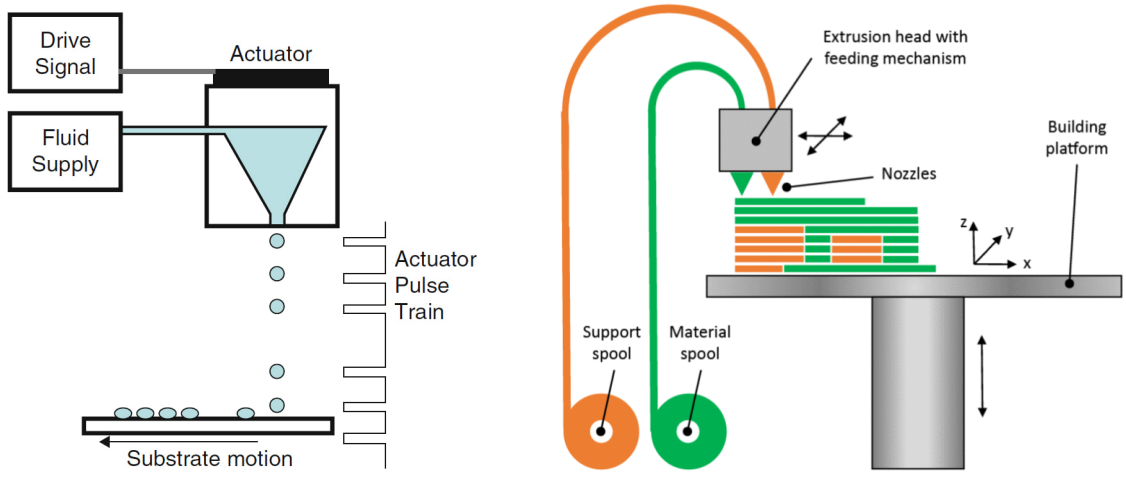

(a) (b)

Figure 1.2: Scheme of the FDM process (b) [6], and DOD materials jetting (a) [15].

Materials: ABS (acrylonitrile butadiene styrene) is the most common material and can be utilized on all current Stratasys FDM machines. According to the latest developments, depending on the configuration of FDM machines, they can use ABS together with other polymers like polycarbonate (PC), PLA, PET, etc. Detailed information on the mentioned blends will be avoided in this section since FDM is not the main focus of this thesis, but a wide range of different blends are reported in the literature [8, 37, 57].

Applications: Fused Deposition Modeling (FDM) is utilized in various sectors, including rapid prototyping, aerospace lightweight component manufacturing with complicated geometry, medical prosthesis creation, and orthodontic device creation. It is also used in developing ceramic part fabrication processes using solidified ceramic pastes, making it a versatile tool in various industries [4, 15].

Benefits and Drawbacks: FDM is an affordable, accessible, and user-friendly method for producing complex components, with the possibility of having a multi-material product by adding an extra extruder. However, it has limitations, such as the fact that providing very high-resolution components can be challenging, which makes it unsuitable for applications that require extreme precision. It is also limited in terms of materials, so it is not an ideal choice for applications demanding high-temperature resistance. In addition, parts

created with FDM may require post-processing to enhance their mechanical properties or improve their surface finish [4, 6, 53].

Material Jetting Techniques

In the late 1980s, Scott Crump, inventor of FDM, developed material jetting (MJ), which involves the preparation of materials in liquid form and loading them into print heads or nozzles. The procedure includes jetting precise droplets of material, which solidify or cure on earlier layers. Support structures may be jetted for overhang stability. Depending on the machine design and preferred printing method, multiple printing patterns are available, like the drop-on-demand (DOD) system shown in Figure 1.2 [6, 15].

Materials: Polymers have been the primary materials used in the AM technique since its inception, starting with candelilla wax studied by Gao et al. [12]. The latest polymers introduced for this method are UV-curable polymers like urethane acrylate. Recent developments introduced ceramics like alumina as a suspension, in the wax carrier and studied low-melting-point metals and alloys like solders, which are available in the literature [15].

Applications: Beginning with metal printing as the primary focus of this study, current MJ development has exploited MJ in the electronics industry for the production of traces, connections, and soldering on IC test boards. Polymers, on the other hand, have been developed to serve a wide range of industries, including printing parts in aircraft, automotive, medical, and sports goods [6, 15].

Benefits and Drawbacks: Material Jetting (MJ) has various advantages, including low cost, high speed, easier scalability, and the capability to print different materials and colors in high resolution. While MJ provides notable benefits, it is currently subject to material limitations, mainly restricted to waxes and photopolymers on a commercial scale. Additionally, in comparison to FDM and VAT photopolymerization, MJ may demonstrate reduced part precision for bigger components [6, 15, 55].

Vat Photopolymerization Techniques

VAT Photopolymerization, also known as stereolithography (SLA), is one of the first additive manufacturing techniques, patented by Charles W. Hull in 1986 [20]. To have a basic definition of the process, it involves a chain reaction on a resin or monomer solution using UV light or an electron beam. Monomers, often acrylic or epoxy-based, transform into polymer chains, solidifying a pattern inside the resin layer as can be seen in Figure

1.3. By the end of the process, unreacted resin is removed, and the final product is revealed [37, 39].

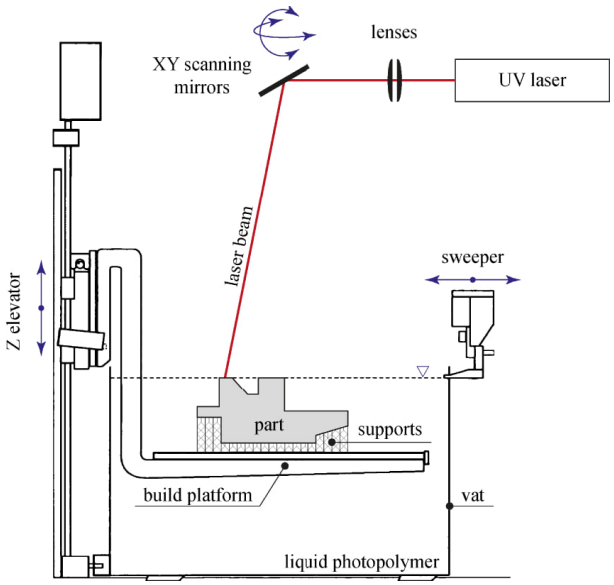

Figure 1.3: Scheme of the Vat photopolymerization process [6]

Materials: Material selection is crucial in SLA since it directly affects the mechanical characteristics, appearance, and suitability of the products. Acrylic and epoxy resins are common polymer materials used in SLA. New epoxy-based and hybrid polymers (epoxides with some acrylate component) with improved qualities were launched at the start of the development of SL technology [6, 55]. Furthermore, polymer-ceramic composite products can be created by dispersing ceramic particles such as alumina in the resin [39].

Applications: Aside from all of the regular applications, SLA may be useful for the additive manufacturing of complicated nanocomposites due to the high-resolution surface finishing in the final product [39]. This technology could be used in chemical engineering for microtransducers, micropumps, and heat exchangers with millimeter-sized internal channels. Furthermore, the common clinical application of SLA in dentistry is for creating surgical templates for dental implant planning and placement [6].

Benefits and Drawbacks: SLA printing technology has the ability to print high-quality parts at a fine resolution, which, besides its great flexibility in supporting many different machine configurations, size scales, light sources, and scanning patterns, are its main advantages. In the meantime, the selection of materials is primarily limited to photopolymers, which may not be suitable for having optimal mechanical properties or

high-temperature resistance in the final product. Together with the slow and expensive operation, these are the main limitations of this method [15, 37, 55].

Directed Energy Deposition (DED)

Directed energy deposition (DED), a fusion-based AM technique, is a common method for printing metal alloys that was pioneered in the mid-20th century. The process involves the precise deposition of material, often in powder or wire form, using a focused energy source, such as a laser or electron beam. The working principle is the melting and fusing of material, which is deposited layer by layer, allowing for the creation of complex 3D structures which has been improved in term of efficiency through the introduction of the combination of AM and subtractive processes within the same machine as is shown in Figure 1.4. Laser power, laser scanning, and spot diameter are the important elements that affect the mechanical properties of the DED processes [26, 31].

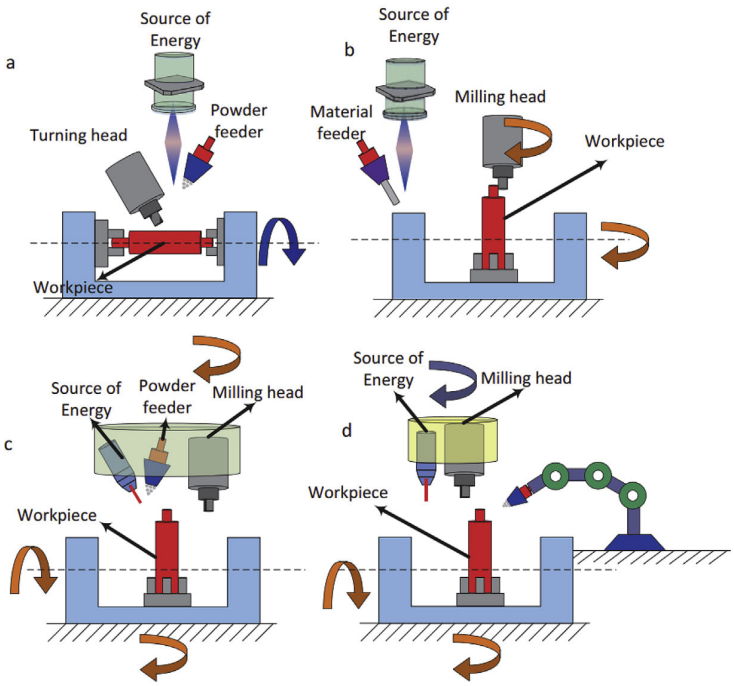

Figure 1.4: Scheme of the hybridized DED process with (a) turning, (b) multi-axis milling, (c) integrated milling system, and (d) separated multi-axis milling system [31]

Materials: Metal alloys having a wide range of characteristics in powder form, such as titanium, copper, gold, aluminum, and iron, are common materials to be used in this method. However, this method has developed in terms of material hiring and has lately expanded to include plastics, ceramics, and composite materials. Furthermore, early-stage machines used wire feedstock, but more recent DED systems utilize powders, which

provide wider material possibilities and precision [26, 31].

Applications: Direct energy deposition technologies find widespread use in various industries. It is used for the production, repair, and refurbishment of worn components in various sectors such as aerospace (turbine blades, engine components, and brackets), medical (implants, scaffolds, and earplugs), automotive (gear, gearboxes, and bumpers), and oil and gas industries. Finally, it is crucial in the production of large metal parts, including molds and dies for industrial applications [15, 26, 31].

Benefits and Drawbacks: This AM method offers benefits like repairing and enhancing existing components, reducing material waste, and working with various materials like metals and ceramics. However, issues with surface texture, mechanical properties, and accuracy still exist. Regarding surface finishing, this technique uses a support structure that causes poor quality in certain areas. Additionally, shrinkage, lack of fusion, and a non-optimal material flow rate cause irregular pores. Processing parameters like feeding rate and scanning speed can induce or maximize distortion, porosity, and residual stress and result in undesired mechanical properties [15, 26, 31].

Powder Bed Fusion (PBF) Techniques

Powder bed fusion (PBF) processes were among the first commercialized AM processes. The concept of powder bed fusion can be traced back to the 1980s, when Dr. Carl Deckard and Dr. Joseph Beaman, both from the University of Texas, pioneered the selective laser sintering (SLS) process, which was the first commercialized PBF process [22].

To put it simply, the fundamental principle backing PBF, demonstrated in Figure 1.5, involves the selective fusion of powdered materials using a high-energy source, most commonly a laser or electron beam. This energy source is precisely controlled to selectively sinter or melt one layer of material powder at a time based on 2D slice data from 3D CAD data and stack multiple layers in order to generate a three-dimensional structure [35, 38].

All the PBF processes share this basic set of characteristics and only change one or more details to improve machine productivity, meet the different energy source requirements, and enable the possibility of processing different materials. Due to these adjustments and the high compatibility of PBF methods, they are widely used and have a broad range of materials, including polymers, metals, ceramics, and composites [15].

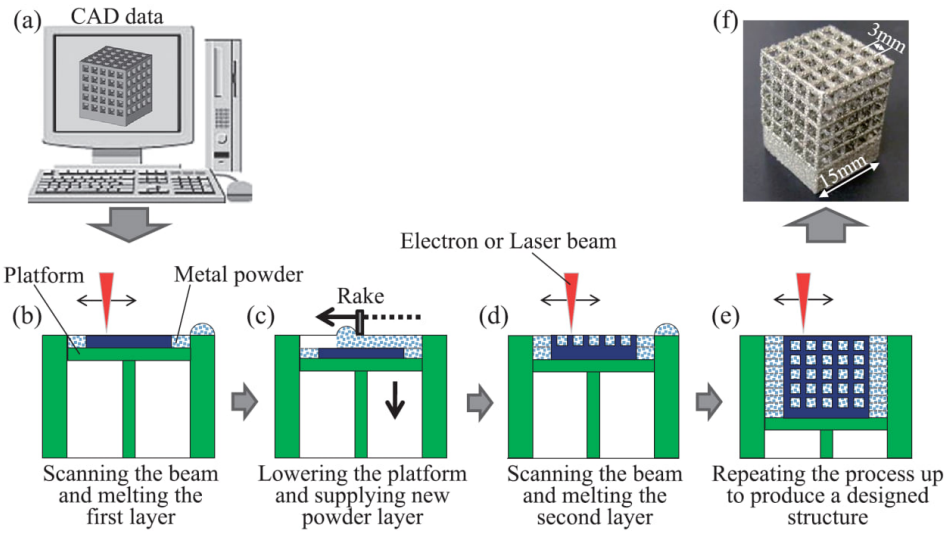

Figure 1.5: Scheme of the powder bed fusion (PBF) in fabricating a metallic product [38].

Materials: Generally speaking, all the materials that can be melted and resolidified can be used in the PBF processes [15]. To be more specific, in polymers, thermoplastic polymers like polyamide are well-suited for powder bed processing, unlike thermoset polymers, since they do not melt and will just degrade. In metals, any metal that can be produced in powder form and welded is considered a good candidate for PBF methods. Ceramics, metal-ceramic composites, and biocompatible materials are other materials that have been introduced to PBF methods in recent developments [6, 15, 18].

In the following parts, the most commonly used PBF sub-methods that are tailored for specific materials and applications will be introduced. There are just a few small differences between these methods and their materials, and they share the same fundamental principle. These differences are mainly the operating materials and the energy source that each method uses, which can be laser bases, such as selective laser sintering (SLS), direct metal laser sintering (DMLS), selective laser melting (SLM), or electron beam base method, which is electron beam melting (EBM) [6, 15].

One point that needs to be mentioned is the laser powder bed fusion (LPBF) concept, which is commonly referred to as SLM in the literature. However, LPBF is a concept that not only includes SLM but also covers other laser-based PBF sub-methods like SLS that are employed to operate materials other than metals [18].

Selective Laser Sintering (SLS):

As previously stated, selective laser sintering (SLS) was the first powder-bed-based process conceptualized by Dr. Carl Deckard and patented in 1989 [22]. This method was a milestone in the AM domain. Because of its capability to produce complex 3D shapes with precision and detail, it has had a significant impact on product design, manufacturing, and innovation. This feature allows engineers and designers to have more efficient, lightweight, and high-performance components [15].

Similar to other AM methods, selective laser sintering (SLS) is a layer manufacturing process that generates complex 3D parts by selectively sintering successive layers of powdered materials [54]. Similar to the scheme previously indicated in Figure 1.5, the process begins with a thin layer of powdered material spread evenly across the build platform. A high-powered laser selectively sinters or fuses the specific points, binding the powders to form the desired layer based on the cross-section calculated from the 3D CAD model. The build platform then descends, and a new layer of powder is spread on top. Then the layer-by-layer process continues until the entire 3D object is created [18, 23, 54].

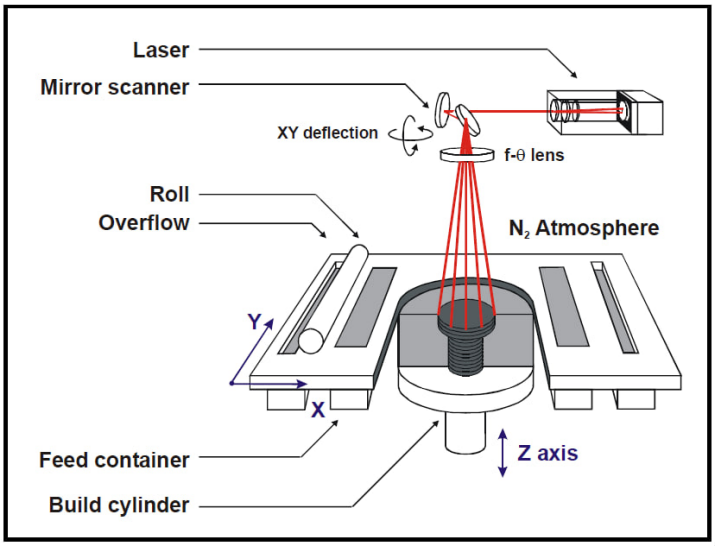

Figure 1.6: Scheme of a commercial selective laser sintering machine [23].

As shown in Figure 1.6 as a scheme of a commercial SLS machine, each commercially developed machine has multiple elements that need to be altered based on the desired application and requirement of the in-use material. For instance, the way that the powder is deposited (roller or scraper), the atmosphere (Ar or N2), and the kind of laser employed (CO2 laser, lamp or diode-pumped Nd:YAG laser, disk or fiber laser) are parts that differ from case to case [23].

Materials: Since its launch, selective laser sintering (SLS) has evolved to include an extensive range of materials. In its early days (1980s), SLS primarily utilized amorphous or semi-crystalline polymers, such as nylon and polyamide [22]. Following the continued development of SLS machines, technology has been extended to include metals such as aluminum and steel for functional components. Ceramics, composites, and biocompatible materials for medical uses have been added to the material palette since the 2010s [18, 22].

Applications: As mentioned, recent developments, through providing diversity in materials, have made SLS an optimal option in a variety of sectors, including aerospace, automotive, healthcare, and consumer products. Its ability to produce functional and durable components makes it ideal for prototyping, end-use parts, and complicated geometries. Manufacturing lightweight aerospace components, personalized medical implants, and complex architectural models are a few examples of the sectors in which SLS has been deployed so far [18, 54].

Benefits and Drawbacks: Selective laser sintering (SLS) has many advantages, including the ability to utilize a broad range of materials, from plastics to metals, making it adaptable. SLS does not require support structures, which reduces material waste, and it is capable of producing complex shapes. However, there are disadvantages, including longer build times, when compared to other PBF techniques such as SLM or DMLS. The surface finish may be rough, and post-processing is frequently required. Furthermore, when compared to technologies like SLA, SLS may have problems achieving fine feature resolution [18, 23, 54].

Direct Metal Laser Sintering (DMLS):

Direct metal laser sintering (DMLS) is a powder bed fusion technology and an extension of the SLS method that was patented and commercialized by EOS, a German company founded by Dr. Hans J. Langer in the late 1990s. In simple terms, DMLS was developed to specifically apply SLS to metal powders to create metal components [32]. Although both SLS and DMLS employ laser sintering, DMLS is far more closely aligned with SLM in terms of material used and their special concentration on metal components, whereas typical SLS is strongly related to polymers and plastics. Aside from the material difference, the SLS process fuses or sinters powdered material just below its melting point, whereas the SLM and DMLS methods employ molten materials to bind and create the final product [18, 32].

The working principle and the setup are nearly similar to what was previously discussed

for PBF (Figure 1.5), but the terminology and specific details related to materials and process parameters could be more specified. To be precise, the energy delivered by the laser melts the particle's exterior while leaving its core solid. The molten metal acts as a binder, connecting the particles. Due to the binding mechanism, the parts are porous with reasonable mechanical properties that make them useful for the production of filters or gas storage systems [54].

Materials: However, while the DMLS method is limited to using only metals, it can offer significant flexibility to work with a range of metal powders, including titanium alloys, stainless steel, cobalt-chrome alloys, and Inconel superalloys [18, 38].

Applications: Direct Metal Laser Sintering (DMLS) has several applications in a variety of sectors. It is frequently used in the aerospace and robotics industries for the production of complicated and lightweight components such as airplane parts, engine components, and brackets [32]. DMLS is used in the medical profession to create personalized implants and orthopedic devices [18]. DMLS is used in the automobile sector for manufacturing complicated parts for engines and exhaust systems, as well as in research and development for quick prototyping and tooling [38].

Benefits and Drawbacks: DMLS, like SLS and SLM, can generate complicated geometries without the need for support structures, decreasing the waste of material [18]. However, DMLS stands out because of its high accuracy in metal component fabrication, while SLS is more adaptable with a wider range of materials. DMLS, requires post-processing for surface finishing, although DMLS may reach better detail in metal products in the end. On the other hand, DMLS has greater costs because of the equipment and materials, and it may take longer to manufacture than SLS and SLM [23, 32].

Elecctron Beam Melting (EBM):

Electron Beam Melting (EBM) is a Powder Bed Fusion (PBF) technology that melts and fuses metal powders layer by layer using an electron beam. The first patent for this technique was issued in 1992 [28]. However, Arcam AB, a Swedish company, produced the first commercial EBM system in 1997 [54]. In EBM, instead of a laser, a high-power (about 4 kW) electron beam is employed as the power source, which can only be used on conductive metals. The fact that the energy per volume unit (energy density) is greater than that of laser equipment and that the electron beam is controlled by electromagnetic coils (Figure 1.7) allows for enhanced melting capability, resulting in higher productivity as compared to SLM machines [6, 15].

There are a few important differences between the EBM method and the LPBF method that are worth mentioning. The first fundamental difference between SLM and EBM processes is that the EBM chamber works in a vacuum atmosphere, thus reducing any contamination picked up during the process. The other important difference is that the electron beam, thanks to its high scanning rate, allows a general preheating of the powder before melting, which reduces the thermal stresses in the final product. This results in a stress-relieving component, thus limiting the risk of crack formation. [6, 15, 18].

Materials: The Electron Beam Melting (EBM) process is versatile and covers a wide range of conductive materials. Two of the most commonly used metals are Ti6Al4V and CrCo used for the production of orthopedic implants by EBM [18]. Notable materials for EBM include gamma-TiAl alloys, Titanium alloys, nickel superalloys (Inconel 718 and Inconel 625), cobalt superalloys, copper, stainless steels, and pure niobium for special applications [6].

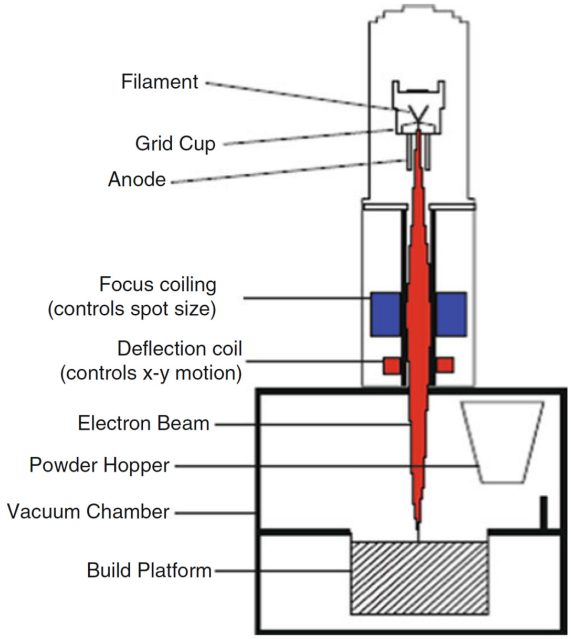

Figure 1.7: Scheme of the Electron Beam Melting (EBM) [15]

Applications: EBM, due to its final products having low residual stress and applying to a wide range of special superalloys, has seen applications in two main fields: aerospace and orthopedic implants. Concerning orthopedic implants, EBM is used to produce parts such as acetabular cups, knee, maxillofacial plates, hip, jaw replacements, etc. [18, 35]. Regarding aerospace, it covers the production of multiple components such as titanium aluminide low-pressure turbine blades and is employed in automotive with the production

of titanium aluminide turbochargers and even in the production of superconducting radio frequency cavities using high-purity niobium [6, 15].

Benefits and Drawbacks: EBM offers the advantage of producing complex parts with desirable microstructures and also different porous structures in different parts of a single component. In addition, as mentioned before, residual stresses in EBM-produced samples are much lower than the products of other LPBF methods [6, 15]. Moreover, in the laser-based methods, the output energy for the same input is much less than in the EBM, and the same energy laser is much more expensive [15]. The main drawback is the intensive computational modeling required for process optimization and control, as well as the fact that only conductive materials could be used [18]. Although the operation of printing in a vacuum environment has benefits, it also causes problems, which can be mentioned as having very expensive costs and the limitation of components due to the small size of the vacuum chambers. On the other hand, the process can also be time-consuming. As a limitation, EBM methods also need the addition of supports, but the mass of these supports is an order of magnitude less than other LPBF methods [15, 43, 54].

Laser powder bed fusion (L-PBF):

Laser powder bed fusion (L-PBF) previously called selective laser melting (SLM) is a powder bed fusion (PBF) process that employs one or multiple laser beams to selectively fuse and melt regions of a powder bed in a layer-upon-layer manner using computer-aided design (CAD) data. The L-PBF process consists of a series of steps that are quite similar to those of other PBF technologies (Figure 1.5), beginning with the creation of CAD data and ending with the removal of the produced components from the building platform. On the other hand, it has distinctions such as different energy sources than EBM and different levels of fusion in comparison to SLS but similar to DMLS [6, 34].

The first L-PBF system was introduced by Fockele and Schwarze in the 1990s, which was a stainless steel powder-based system developed in collaboration with the Fraunhofer Institute. Then the first generation of L-PBF systems was exploited in the 1990s and 2000s by small-scale spin-off companies such as SLM Solutions and MCP in Germany [13].

In recent years, L-PBF has taken over selective laser sintering (SLS) and gained lots of attention due to the availability of fiber laser technologies and the other beneficial capabilities of this method [34]. Since this method is the main topic of this research, a brief recap of its applications, materials, and advantages is addressed in the following, while a detailed description of all its capabilities and points that need to be considered is

mentioned in the second section of this chapter 1.2.

Materials: In terms of materials, L-PBF is mostly employed with metals. While metals such as titanium, aluminum, and stainless steel are used in the majority of L-PBF applications, there have been ongoing developments that have extended the range of materials, including ceramic particles such as zirconia and composites that incorporate non-metallic particles into the metallic matrix to improve product properties. These developments extended the diversity of the materials to be used in the new L-PBF applications [10, 13].

Applications: L-PBF, as a leading metal 3D printing method, is primarily used for producing complex, high-performance metal parts in industries such as aerospace, which includes the production of lightweight aircraft components; automotive, which covers high-speed prototype design and customized components; and healthcare, which encompasses the production of patient-specific metallic or ceramic implants and other high-value medical device components or low-volume, high-value applications. L-PBF metal printing has numerous potential uses, and with its present rate of development, the variety of its applications will expand day by day as manufacturing costs are reduced through machine efficiency improvements [13, 34].

Benefits and Drawbacks: High accuracy and resolution, high part density, design flexibility, and the ability to build complicated, unique geometries are among the advantages of L-PBF. It is preferred for quick prototyping and end-use part manufacture. On the other hand, L-PBF has limitations, including size restrictions and the requirement for post-processing to eliminate support structures. Furthermore, multiple operating parameters that affect the final product's properties, like poor roughness and residual stress, might be problematic [13, 23, 34].

1.1.3. General Challenges in Additive Manufacturing

As previously mentioned, each additive manufacturing (AM) method has drawbacks that limit its applications and the range of materials that can be employed through this method. Apart from the mentioned individual limitations, the AM industry has general limitations that need to be solved through further investigations. The most important drawbacks can be briefly mentioned as follows [6, 13, 15, 18, 34, 46].

1. **Limited Material Options:** One of the key challenges that are shared among all the AM methods is the availability of suitable materials.
2. **Post-processing and Surface Finish:** Most AM methods require post-processing

to achieve desired surface finishes and tolerances. To be more specific, powder bed fusion (PBF) technologies like SLM or L-PBF often require support structures that must be removed after printing.

3. **Speed and Scalability:** AM processes like SLM and SLS are relatively slow compared to traditional manufacturing techniques. While methods like FDM are faster, but might compromise precision. Continuous and large-scale production is more challenging with some AM methods due to their layer-by-layer nature. Balancing speed and scalability is still a critical challenge.

4. **Precision and Resolution** The level of accuracy and resolution required for different applications varies, and it is challenging to improve the AM method's resolution because it is dependent on many factors and requires further investigation.

5. **Certification and Regulatory Compliance** One of the most discussed challenges of AM products that have not been mentioned in this research yet is the strict regulations that some industries have. To be more precise, in industries like aerospace and healthcare, components must adhere to strict regulations and certifications, like the biocompatibility of the AM-produced implants.

6. **Material Recycling and Waste Reduction:** While additive manufacturing is often regarded as environmentally friendly due to its potential to minimize waste and energy consumption, some processes, such as powder-based techniques, create excessive, non-reusable materials. However, reducing waste and recycling used AM materials has been an ongoing study in recent years.

7. **Final Product Properties:** The mechanical, thermal, and chemical properties of AM-produced parts often vary from those of conventionally manufactured components. These characteristics depend on many parameters, including AM materials, printing parameters, and component geometry, that have been one of the main research topics over the past decade. It is worth mentioning that the effect of printing parameters on mechanical properties is the focus of this study.

To sum up, AM involves several limitations, and each AM approach has its own set of advantages and disadvantages. However, overcoming these challenges will keep driving innovation in the AM industry and broadening its applications across other industries, as well as the developments that have been introduced to this field in recent years.

1.1.4. Future Directions and AM Development Trends

As a matter of fact, additive manufacturing has been a transformative and developing technology since its beginnings in the 1980s and still is one of the focuses of research centers and industries. Considering the present challenges that the AM sector is experiencing (1.1.3), and the market demands from AM technology to reduce costs and increase production speed, future potential developments may be categorized into three general areas, as mentioned in the following lines.

1. AM Machine Development
2. AM-related Software Development
3. AM Materials Development

AM Machine Development: As mentioned so far, each of the AM methods has limitations that should be considered in future developments first to improve the efficiency of the method and second to expand its applicability to an extended range of materials and applications. It is also valid that the development of AM methods is closely related to the development of other technologies like laser, CNC machines [15], and 3D scanning systems [2] that contribute to the improvement of AM methods' efficiency.

AM-related Software Development: Although additive manufacturing machines, namely AM hardware, have been introduced to great developments since their inception, AM software has not gotten attainable focus from researchers and developers. It is worth mentioning that improvements in scanning methods for 3D models, STL file interpretation, and the preparation of printing files are fields that could be studied more in future projects. Apart from the mentioned topics, improvements in scanning strategies, control of printing parameters, powder spreading methods, and design of supports are fields that could be further investigated [13, 15, 34].

AM Materials Development: The introduction of new AM materials is a highly beneficial field of study since it provides a broader range of new applications for which AM methods were previously not applicable. The properties of the AM materials that affect the final product, such as the adaptability of materials to be produced through the AM methods, the absorption of lasers by materials, and particle size distribution could be the objective of future studies [13].

As an effective and recent example of the new AM materials, high-entropy alloys (HEAs) have been studied in recent years to be produced through AM methods like L-PBF and are known as AM-HEAs. The introduction of AM-HEAs suits both HEA materials, as

AM solves the conventional manufacturing problems of the materials, and AM, since it introduces a wide range of applications and markets to AM methods [61].

To summarize, additive manufacturing is progressing, and its limitations are actively being investigated at research institutes at a growing pace. Through the development of additive manufacturing, products can be brought to markets through product conceptualization, product creation, and product propagation carried out by individuals in any location. AM allows digital designs to be converted into physical objects at the same location or anywhere in the world (i.e., "design anywhere, build anywhere") [15].

1.2. Laser Powder Bed Fusion (L-PBF)

Along with other PBF techniques, a basic overview of Laser powder bed fusion (L-PBF) or previously called selective laser melting (SLM) has been presented in 1.1.2. However, a more detailed description of this method, which is highly required for understanding the purpose of this thesis, including fundamental work principles (1.2.1), specific pros and cons (1.2.2), applications (1.2.3), and printing parameters (1.2.4), is extracted from the current state of the art and mentioned in this chapter.

Introduction

SLM, or selective laser melting, also known as laser beam melting (LBM) and laser powder bed fusion (LPBF), is the most widely used powder bed-based (PBF) AM technique [61]. The SLM process was developed in the 1990s by Dr. M. Fockele and Dr. D. Schwarze in collaboration with the Fraunhofer Institute to produce metal components from metallic powders using a high-intensity laser as an energy source to melt selectively a fine metallic powder in a layer-by-layer manner following the computer-aided design (CAD) data as previously shown in Figure 1.5 [6]. The technology has witnessed substantial development milestones, starting in the 1990s and early 2000s with small-scale spin-off companies such as SLM Solutions in Germany, which are referred to as the "First generation" of SLM machines, followed by further development of the technology around 2010 by Renishaw, which is most commonly referred to as the "Second generation" in the literature [34].

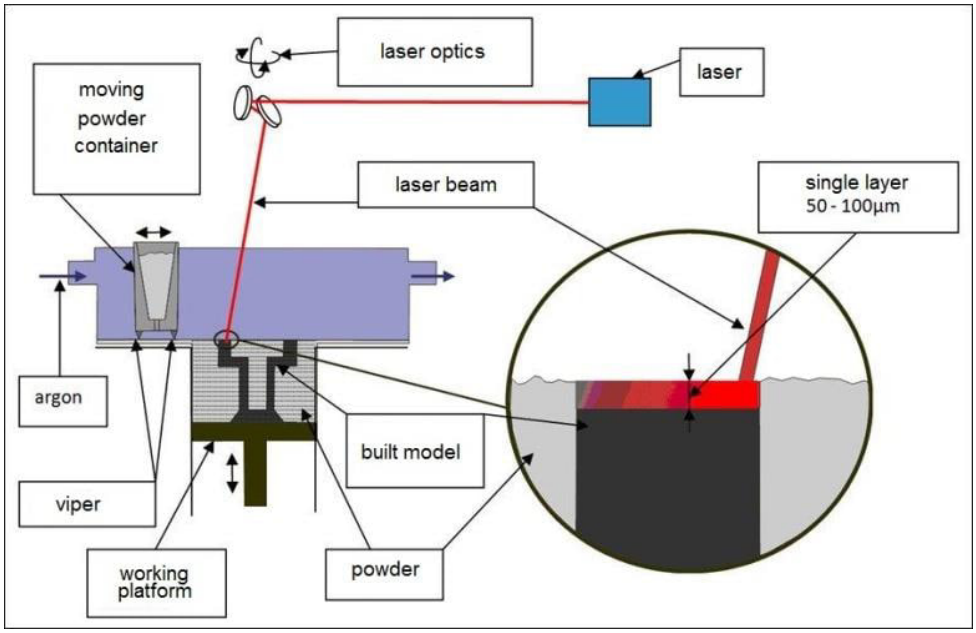

Figure 1.8: Scheme of the Laser powder bed fusion (L-PBF) machine [24].

1.2.1. Fundamental Work Principles

Principal Steps

The Laser powder bed fusion (L-PBF) procedure consists of several sequential stages, starting with the preparation of 3D CAD data and concluding with the removal of fabricated components from the building platform. Prior to the uploading of 3D CAD data into the L-PBF machine, the STL (Standard Tessellation Language) files had to be processed by software. These files serve the purpose of creating support structures for any overhanging features and generating slice data, which represents 2D cross-sections for laser scanning of individual layers. The actual production process starts with the application of a fine layer of metal powder onto a substrate plate within a dedicated building chamber. Subsequently, a high-energy density laser is employed to selectively fuse areas according to the processed data. After the laser scanning of a given layer is finished, the building platform descends by the thickness of a layer, and a new layer of powder is deposited from a movable container and laid on top of the previous one, providing a permanent connection across the entire object, and then the laser scans this new layer. This repetitive process continues until the components are fully constructed [13, 34].

As can be seen in Figure 1.8, the laser beam is controlled by the scanner on the XY plane, and the platform is moved in the Z direction [24]. Also, it is shown that the process operates in an argon environment. The presence of this protected environment is due to the fact that, because of the high temperatures required for melting, the components are created in a controlled oxygen environment using an inert process gas, argon or nitrogen, to prevent oxidation and other issues that might affect the mechanical properties of the produced part throughout the L-PBF process [6].

It is worth mentioning that it is crucial to have a precise evaluation of the amount of the required powder and the volume of the powder container, to ensure the process will not stop to avoid subsequent problems [33]. Further detail in this regard is provided in the following sections.

Binding Mechanisms

One of the critical discussions in AM technology is the binding mechanisms and the principle of particle attachment. These mechanisms are strictly related to the materials' properties and the selected AM method. To be more focused on the LPBF methods, namely, SLS, DMLS, and SLM, binding mechanisms in these techniques can be classified into four different categories, as shown in Figure 1.9 [23, 33].

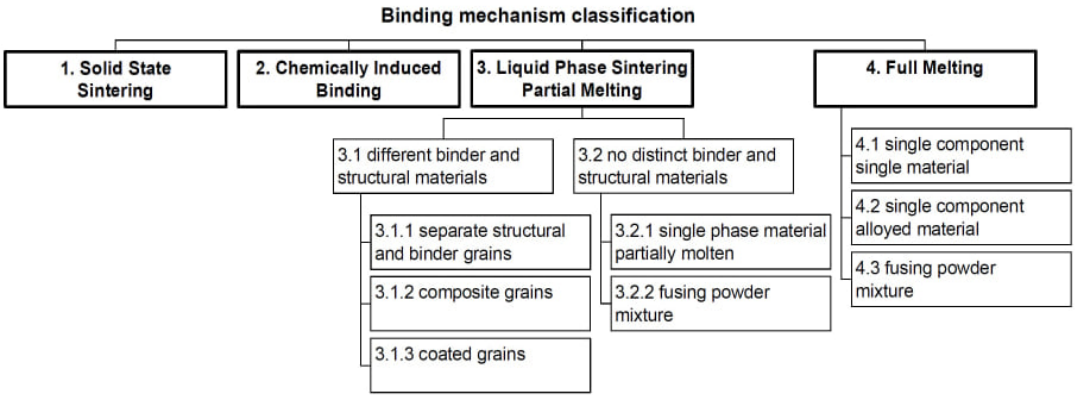

Figure 1.9: Classification of LPBF-technologies according to binding mechanisms [23].

Since the focus of this thesis is on the L-PBF method and the active binding mechanism in this technique is full melting, other mechanisms are not discussed further. In recent years, the idea of "Full Melting" metal powders has been explored, since the rapid melting and solidification of AM metal alloys result in unique mechanical properties that are much better than those of early-time SLS parts and sometimes even more desirable than cast or wrought parts made from identical alloys [15, 23].

1. Single component single material
2. Single-component alloyed material
3. Fusing powder mixture

1. Single component single material Studies carried out at Fraunhofer Institute ILT and Leuven University on pure Titanium powder, showed the L-PBF-printed part had a density of almost 100 percent, however, it also indicated signs of thermal stress [23].

2. Single-component alloyed material These powders are made up of a single type of grain, which is built up of alloyed materials such as stainless steel 1.4404, tool steel 1.2343, and titanium alloy TiAl6V4. Many different alloys have been studied, and some of them are now commercially available. A case study on Stainless Steel 1.4404 conducted by Fraunhofer Institute ILT indicated that the mechanical characteristics are equivalent to bulk material except for the ductility, which is significantly reduced [1, 23].

3. Fusing powder mixture Depending on the degree of melting, some processes use powder mixtures under selective laser melting (all powder particles melt) or partial melting, in which some powder particles remain nonmolten, and the border between ‘partial melting’ and ‘full melting’ is unclear [15].

Laser Beam

As introduced in 1.1.2, many early additive manufacturing (AM) systems used lasers as high-intensity energy sources. To specify, there are two classes of laser processing in AM: curing and heating. For polymer-based machines, the laser usually works in the ultraviolet range to solidify and "cure" the resin. Lasers employed for heating, on the other hand, aim to transmit enough thermal energy to melt metal powder, as seen in L-PBF technology. The laser system is the core of the Laser powder bed fusion (L-PBF) process, as it is the main tool for selectively melting and solidifying the metal powders in each layer [15, 33]. While the effective laser parameters are discussed in 1.2.4, this section is dedicated to the structure and working principle of the lasers used in the L-PBF method.

L-PBF systems predominantly employ three types of lasers: carbon dioxide (CO2) or tube lasers, Nd:YAG lasers, and fiber lasers which are described briefly with a special focus on fiber laser as the most used one in almost all AM machines.

1. **CO2 or tube Lasers:** CO2 lasers, used in earlier polymer-based AM machines, are less commonly used in L-PBF methods due to their lower energy efficiency, which can result in higher operational costs. CO2 lasers offer advantages such as suitability for processing thicker materials and lower initial costs; however, they may not provide the same level of detail and precision as fiber lasers due to their larger wavelength [15].

2. **Nd:YAG Lasers:** The Nd-YAG laser was used by Fraunhofer for the first time instead of the CO2 laser, resulting in improved absorptivity for metal powders. Nd:YAG lasers, work on the concept of stimulated emission. When activated by a flash lamp or another laser source, the Nd:YAG crystal generates a monochromatic and extremely coherent laser beam that can be successfully focused to a small spot size. This concentrated laser beam selectively melts and fuses metal powder layers in the L-PBF method with fine resolution [15, 33].

3. **Fiber Lasers:** Almost all metal AM machines employ fiber lasers, which are less expensive, easy to maintain, more compact, better beam quality than Nd:YAG lasers, and more energy-efficient, which can lead to lower operational costs over time. They generate an extremely fine focal point, allowing the manufacturing of complicated and small components. Because of this accuracy, fiber lasers are perfect for applications requiring complex and detailed components. Furthermore, they are also noted for longer lifespan of diode pumping sources thus longer operational time. It is critical to remember, however, that fiber lasers can be far more expensive than CO2 lasers [15, 33, 34].

Working Principle, To have a complete understanding of the fiber laser work principle, the optical pump diodes are coupled onto an active laser fiber with a special reflective coating and Bragg gratings that reflect the laser light back and forth along the length of the fiber, to create a coherent beam of light at the output of the laser. Beam delivery is often accomplished using additional optical fibers that provide a durable, flexible, fully enclosed beam path for delivery and containment of the light energy. Final beam delivery includes optical elements and lenses to condition and focus the beam after it leaves the optical fiber. Manipulation of the beam in L-PBF is often accomplished by magnetically driven mirrors using galvanometers rather than CNC motion which is common in other am methods. This method allows the rapid movement of the beam impingement location within the build volume in a controlled manner with the use of directional mirrors [33].

To start the laser beam's action, the beam moves over the building surface and starts the selective melting of metal powder based on the layer cross-section given in the STL file. As is indicated in figure 1.10a, the laser beam moves through a defined path, also called the scan pattern, heads toward the metal powder, and leaves solidified metal behind.

A few points in this figure that need to be considered can be mentioned, such as the difference between the powder layer thickness and the deposit layer thickness, which is due to the density difference between the two layers. The excessive powder will be removed by the end of the layer scan. The second point is the melt penetration depth, which exceeds the thickness of the deposit layer and melts a part of the lower layer of the material. The depth of this penetration is highly dependent on multiple process parameters and can be beneficial [33, 34]. The key to a good result is to melt the material in a controlled fashion without creating too much heat so that when the laser energy is removed, the molten material rapidly solidifies again. [15].

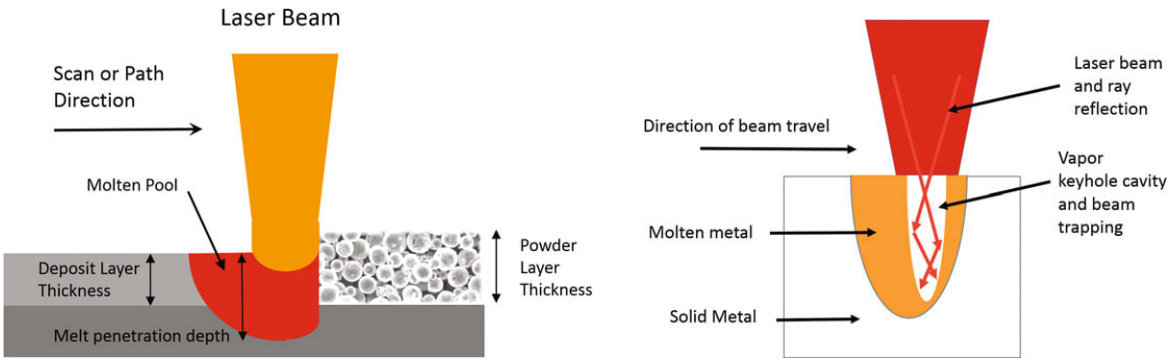

(a) (b)

Figure 1.10: Scheme of laser beam scanning effect(a), Laser keyhole vapor cavity (b) [33].

The interaction of a laser beam with the molten pool is very complex and requires extensive knowledge. To give a general description, the absorption of laser energy by molten metal is often much greater than for solid metal. However, plumes of vaporized metal or plasma can form above a molten pool, absorbing laser energy and detrimentally preventing it from reaching the molten pool. If this effect is not enough, then the pressure of the cloud of vaporized metal and superheated gas can create a sink toward the molten pool, trapping laser energy and further enhancing absorption. This vapor cavity is often called a **Laser Keyhole**, which is shown in figure 1.10b, and may extend deeply into the metal and deepen the melt penetration depth. This keyhole melting may also create defects such as porosity, spatter, balling, or entrapped voids and should be controlled [33].

Heat absorption and melting, keyhole melting, and plume formation can be very abrupt from small changes in laser power, travel speed, focal spot size changes, or other parameters. Careful selection of the laser technology, process parameters, and materials is required to maintain a stable, repeatable process [33]. The superior setting in the L-PBF machines in this regard is the use of inert gases in the working environment. As mentioned, the presence of this protective atmosphere prevents oxidation; additionally, it affects the formation of plasma, which inhibits the absorption of the beam in the treated material. The weakening effect of the laser beam on the plasma is smaller for gases with higher ionization potential. Differences in the depth of penetration of the material can be considerable, especially when used with a high-power beam [13, 15, 33].

1.2.2. Advantages and Disadvantages

Selective laser melting, as the most used powder bed fusion method, has advantages and disadvantages that bring it to the edge of being the best manufacturing option for many applications. Having a clear vision of the strengths and weaknesses of L-PBF in comparison to other AM methods is suitable for the selection of this method for the right application.

Previously, a description of the benefits and limitations had been mentioned (1.1.2, 1.1.3). However, the benefits and drawbacks of the LPBF method, have been studied in the recent state-of-the-art, and a brief overview of them in comparison to other additive manufacturing methods is given in this section.

Advantages: As previously said, L-PBF can develop structures with complex shells, internal lattice structures, internal cooling channels, or complex superstructures, through which it can minimize the use of metal, optimize strength, or extend functionality [13].

In addition, advantages that make L-PBF the superior option in comparison to other methods, as can be seen in 1.11, are briefly explained in the following lines [15, 33, 34].

- A big advantage of the PBF processes is the wide range of CAD software that can be used to generate STL files for these machines. The wide availability of STL file editing software allows for fixing, editing, slicing, and preparation for 3D printing and utilizing the build volume effectively.
- In L-PBF machines, the laser scanning optics rely on magnetically driven mirrors using galvanometers, which allow rapid movement of the beam location within the building volume (Figure 1.8). This use of the mirror to move the laser beam avoids the movement of the entire mass of a laser head to the melting position that is done in some AM methods like DED-L and causes production delays.
- L-PBF offers the opportunity to build multiple instances of the same part at once. In addition, multiple instances of different parts may be built at the same time. The optimization of the positioning of parts within the build volume with various virtual objects, all to be built at once, is done with the provided software.
- The other advantage of the L-PBF method, after recent developments, is the increased processing speed by heating the powder and also the higher purity of the inert gas that is used to accelerate cooling after the process is completed.

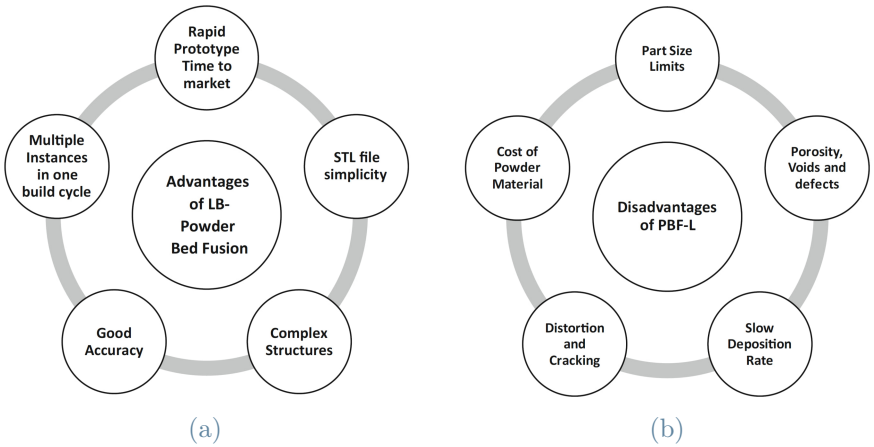

Figure 1.11: Advantages(a) and disadvantages(b) of laser powder bed fusion (LPBF) [33].

Disadvantages: In the following line, a few important shortages and limitations that selective laser melting is currently facing have been explained. Although these problems are critical issues, this method is still an optimal choice for many metals and applications, and mentioning these problems in the provided literature just gives directions that future

research should follow [9, 13, 15, 33, 34].

- One of the main limitations of the L-PBF method is that many process parameters can significantly affect the quality of the final product, and there is no comprehensive database for these parameters and their expected results. Unfused regions of powder, low density, the presence of porosity, and many other characteristic problems are examples of results caused by inadequate parameter selection.
- In L-PBF, the part's orientation and support location are crucial for setting up a build, as it is typically constrained to a substrate at the bottom of the build platform to prevent warping, and it also necessitates an additional step to detach the part from the substrate.
- High residual stresses during the L-PBF process necessitate the use of support structures to prevent excessive warping. This problem necessitates post-processing, which increases processing time, cost, and material waste. This counts as a shortage compared to polymer PBF methods, since in those, the loose powder can be a sufficient support material.
- The L-PBF method faces a significant size limit issue, as the watchmaker's required building volume is significantly smaller than a jet's backbone production line, and this difference forces the LPBF machine producers to specialize the machine for the application, resulting in high equipment costs.
- The other limitation of the L-PBF method is its proper metal powder. As explained in 1.2.4, only metal powders with spherical morphology could be used in the L-PBF method, and since achieving such morphology is not possible through the common commercial powder preparation methods, this limits the L-PBF-specialized powder to an expensive range of powders.

1.2.3. Applications

The momentum in AM metal advancements is quickly changing and evolving toward the manufacturing of high-value components produced by advanced materials. This is noteworthy because the applications that AM metal technology covers, especially by L-PBF, are expanding to new industries on a daily basis, and as a result, the list of below-mentioned L-PBF applications will continue to grow and expand even before the release of this research.

Medical: The major field of use for L-PBF may be summarized in the following manner: customized parts with short fabrication series [43]. One potential category that fits well

within this criteria is biomedical components. Considering it is a novel approach, it still requires testing and certification, and currently, the use of L-PBF in the medical sector is defined as the use of personalized implants (Figure 1.12a,1.12b). However, according to a great number of research and publications that have been done in this field [1, 10, 18, 35, 38], it can be expected that it will occupy an important share of the implant fabrication market in the near future [33].

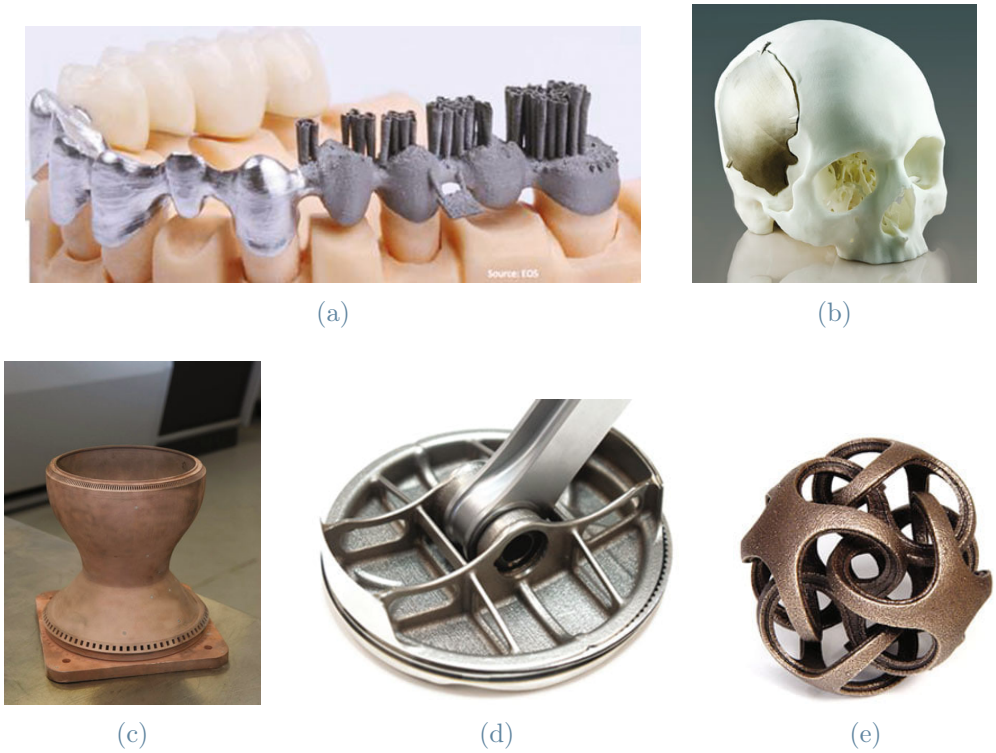

(a) (b)

(c) (d) (e)

Figure 1.12: LPBF produced components, (a,b) Personalized prosthesis,(c) Rocket Nozzle, (d) Automotive piston, (e) Metal Sculpture [33].

Aerospace: Aerospace applications require strict procedures and certification for processes and components. L-PBF additive manufacturing, apart from the ability to tailor the mechanical and corrosion properties of the components, has the potential to provide economic benefits in aerospace applications that can be mentioned as follows [7, 33].

- The reduction of the number of certified parts and processes, such as joining, is achieved by producing the whole process in one unique part, which also avoids the common mechanical problems in the joint points.
- The reduction in weight of lightweight components can result in significant fuel savings during commercial aircraft flights.

- The reduction in material waste during the fabrication of expensive materials such as nickel-based alloys or titanium.

Moreover, L-PBF has been studied and used for specialized applications like heat exchangers [7], and rocket engine parts, like rocket nozzle (Figure 1.12c) [33].

Automotive: Similar to the advantages emphasized by L-PBF in aerospace, the use of the L-PBF approach in the automotive industry provides the same benefits. Some empirical studies compared typical aerospace and automotive production techniques (gravity die casting, cross drilling, electrochemical deburring, and hole blanking) with selective laser melting. It was demonstrated that the nearly identical objects, developed by selective laser melting, had the same mechanical characteristics while using 40 percent less material [43].

As can be seen in Figure 1.12d, multiple engine parts of the cars, specifically Formula One race cars, that are produced in limited quantity, need high mechanical properties, and are made from expensive materials are produced through the L-PBF method. Furthermore, along with the rapid prototyping of functional test parts of automotive components, the production of special and hard-to-find parts, such as those used in historical car restoration, is frequently requested [15, 33].

Tooling: However, the mentioned applications are three main sectors that the L-PBF method serves; it can also be used in the tooling sector for mold making. One of the principal tasks in mold making is to provide adequate cooling, and metal additive technologies, namely, L-PBF, can fabricate the free-form cooling channels. These channels are designed to follow the mold cavity surface and provide a completely homogeneous heat transfer, which helps to provide better quality to injected parts. There are many research works that demonstrate the performance enhancements that can be achieved by using novel heat sink designs fabricated with selective laser melting as compared to conventional pin fin arrays [15, 43].

Art and Jewelry: Following the enormous developments that metal additive manufacturing has experienced, the use of this method became more widespread with cheaper machines, software, and materials. The metal printing machines for creating artwork and jewelry that have been developed in recent years, do not require the same levels of certification and control that are used for the medical, automotive, and aerospace sectors.

Artistic designs that cannot be produced in metal by any other method are made possible while using less material and streamlining the production of custom-made-to-order pieces. Hollow structures with internal supports like Figure 1.12a, allows the fabrication of larger

pieces with the desired strength but without the weight or cost of the solid piece. These systems feature small build volumes ideal for the rapid fabrication of small pieces and minimizing the total volume of precious metal powder stock. A small laser focal spot size provides excellent detailed resolution and allows the creation of fine features and structures [13, 15, 33].

1.2.4. Printing Parameters

Laser powder bed fusion (L-PBF) involves over 100 process parameters that impact the process's accuracy and final product quality. Some additive manufacturing machine manufacturers offer more control over these parameters, while others only provide "proven" materials and parameters [15]. Proper analysis of process parameters is crucial for achieving optimal results. Unlike AM hardware, there has been less focus on this aspect since the beginning of additive manufacturing. However, it has gained significant attention in recent years and, meanwhile, is the main focus of this research [15, 24].

The study of process parameters is more important in the L-PBF method due to the use of metal powders and their special properties, such as high thermal conductivity, propensity to oxidize, high surface tension, and high laser reflectivity, which make metal powders significantly more difficult to process in comparison to polymeric materials. Second, by optimizing the L-PBF settings, products can achieve as-deposited densities of up to 100

Worth mentioning that the parameters that will be described in this section are interrelated and have significant effects on each other. Multiple case studies include developed formulas, graphs, and scientific evidence and confirm this interrelation between the main parameters (1.2.5). However, it is necessary to study each single parameter, its effect, and its optimal range before discussing their relations.

To have a better understanding of the L-PBF processing parameters, they are classified into five major categories that can be mentioned as follows:

1. Laser-related parameters (laser power, spot size, pulse duration, pulse frequency)
2. Scan-related parameters (scan speed, scan spacing, and scan pattern)
3. Powder-related parameters (particle shape, size, distribution, powder bed density, layer thickness, material properties, etc.)
4. Temperature-related parameters(powder bed and powder feeder temperature.)
5. Atmosphere-related parameter (inert gas)

In the next paragraphs, a short description of the most important parameters of each

category will be introduced.

Laser-related Parameters

Laser Power (p): Laser power is one of the four most critical and effective parameters in the L-PBF system (Figure 1.14). This value determines the choice of other parameters of the process and directly influences the amount of energy delivered to the powder bed (1.1), thus affecting the degree of fusion, depth of melt pool, and part density. Higher power can lead to faster processing, but it may also cause excessive vaporization and increase the risk of defects. Typically, it varies in a range from 100 to 500 watts. However, the optimal value depends on the scan speed, material absorptivity, and geometry[7, 17, 48]. It is shown in figure 1.13 that an incorrect laser power selection, regardless of other parameters that are kept constant, can result in an undesired structure where signs of balling defects are clearly visible around the fused strut structure with lower laser power [52]. The other point to consider is the fact that laser absorption increases upon melting and may vaporize low-melting-point elements of an alloy, such as aluminum, magnesium, or lithium, thus changing the chemistry of the deposit, which is a parameter that should be considered in laser power settings to be prevented [33]. It should be mentioned that the selection of laser power is closely related to the size of the focused spot laser[24].

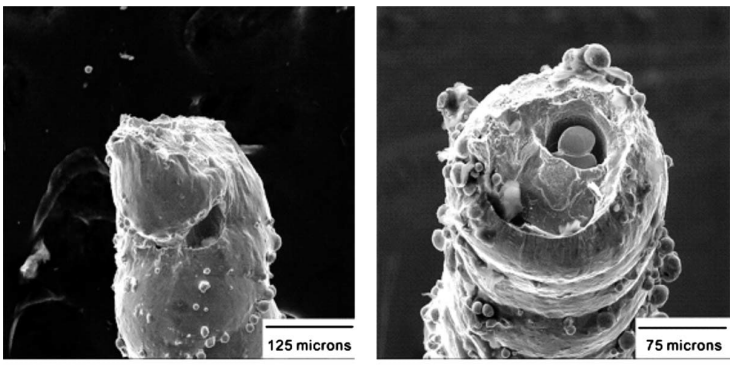

Figure 1.13: SEM micrographs of the failure surfaces of struts with an exposure time of 1000μs and different laser powers following uniaxial tensile loading [52].

Spot Size The size of the laser spot determines the resolution and accuracy of the build. Smaller spots yield finer details and higher resolution but might slow down the process. Larger spots can increase build speed but may compromise precision and are preferred for larger features. The spot size usually ranges from 50 to 200 micrometers, with 50–100 μm dedicated to smaller spots and 100–200 μm to larger spots. The spot size is highly related to the laser technology, laser power, and other parameters [13, 24, 33].

Pulse Duration The pulse duration, or laser dwell time, controls the exposure time of each spot. It impacts melting efficiency and material properties like porosity and mechanical strength. The longer the laser dwells in a particular location, the deeper the fusion depth and the larger the melt pool diameter, so the optimal value should be selected in correlation with other parameters [15]. Optimal pulse duration ranges from 20 to 200μs which shorter pulses create a finer feature, while longer pulses enhance melting efficiency. The optimal spot size and pulse duration balance resolution and efficiency [24, 33].

Pulse Frequency In particular, the tendency of molten metal to form disconnected balls of molten metal rather than a flat molten region on a powder bed surface can be partially overcome by pulsed energy [15]. The pulse frequency sets the rate at which laser pulses are applied. Finding the right balance between pulse frequency and power is critical for controlling the heat input and preventing overheating or insufficient melting. Pulse frequencies range from 50 to 1000 Hz. The choice depends on the desired heat input and material properties. Higher frequencies reduce overheating risks [13, 24, 33].

Scan-related Parameters

Scanning Speed (v): Scanning speed is the speed at which the laser moves over the powder bed and is also one of the four important parameters in the L-PBF system (Figure 1.14) and is also one of the most important parameters that highly affects the quality of components, microstructure, process time, and resolution. The typical scan speed ranges from 500 to 2000 mm/s, and slower speeds ensure better heat input control, while faster speeds are chosen for quicker builds but may impact the quality of the part due to reduced heat input [34]. In addition, it has a direct relationship with laser power, and to acquire the same result from the process with a higher scanning speed, higher laser power is required, and vice versa. On the other hand, the scanning speed is in reverse relation to the amount of energy that is delivered to the surface, as will be explained in equation 1.1, an increase in scanning speed decreases the amount of delivered energy [7, 48].

Scan Hatch Spacing (h): Scan hatch spacing defines the distance between adjacent scan lines (Figure 1.14) and affects surface finish by eliminating or reducing overheating issues. Spacings often range from 50 to 200 µm, where smaller scan spacings result in more precise parts and a higher surface finish, but they also increase build time. Larger spacings can accelerate build speed but may also weaken the bonding due to the low heat input. [33, 46]. Scan spacing should be selected to ensure a sufficient degree of melt pool overlap between adjacent lines of fused material to ensure robust mechanical properties. [15]. Hatch spacing, along with laser power and scanning speed, is one of the four main

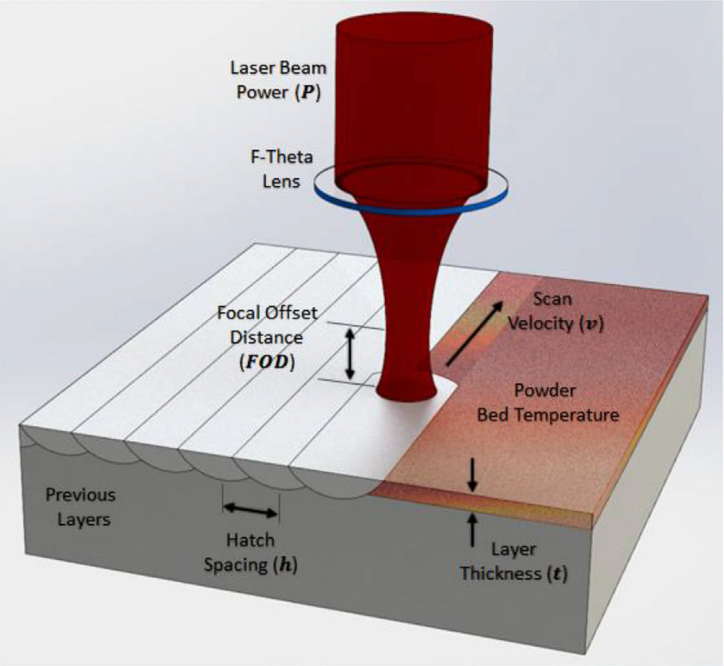

Figure 1.14: Illustration of the L-PBF main operating parameters [48].

parameters that play a crucial role in the printing process and has a reverse relation with the delivered energy to the powder bed (equation 1.1).

Scan Pattern The scan pattern is one of the most important parameters and settings in L-PBF that has a significant impact on mechanical properties like residual stress, anisotropy, tensile strength, fatigue resistance, and thermal behavior. A proper pattern selection is an essential step for the L-PBF method and has to be done based on the goal application, used material, part geometry, and the desired mechanical properties [15, 33]. Due to the importance of this parameter and since it is also a varying parameter in this research, fundamental principles and the most used patterns that have been reported in the literature are discussed in depth in the following paragraphs.

Generally speaking, it is repeatedly stated in the literature that in L-PBF, the choice of scan strategy significantly affects the generation and level of residual stresses. To be more precise, the scan vector length has the maximum influence on residual stress, and the greatest stresses are generated parallel to the scanning vector due to the high thermal gradients. “The increase in scan vector length leads to an increase in residual stress." This is the principle behind the design of the new scanning patterns. In most cases, the patterns are defined to reduce the length of the scan vector, since this limiting reduces the time that passes between the depositions of two successive tracks. In such circumstances, the heat has not been fully dissipated, and so the second track is deposited on the warm

material, which leads to a reduction in the thermal gradient [13, 15, 33, 48]. As a reported case study, the increase in the scan area size from 1 to 3 mm^2 increases the maximum stresses generated from 189.3 to 305.2 Mpa [42].

- **Hatch Pattern** Also called the zigzag pattern in some literature, it is one of the most chosen and widely used patterns. The hatch pattern involves scanning the laser back and forth in straight lines along a single direction for each layer, as indicated in Figure 1.15.a [48]. This pattern is known for its simplicity and efficiency in terms of build speed. The hatch pattern is often used as the default scanning pattern in many L-PBF machines because it provides good coverage of the build area and can help achieve a relatively uniform energy distribution during the melting process. This pattern, in comparison to more developed patterns, has less qualification in terms of induced residual stress; however, alternatively, the scan pattern can be rotated, generally by 90°, between subsequent layers to produce parts with reduced residual stress and prevent anisotropy [15, 33, 42].
- **Island Pattern** Also called partition pattern in some literature [13], is a scanning strategy that subdivides the component into smaller areas that are scanned individually, and the scan strategy of each sub-section can be independently chosen, as can be seen in Figure 1.15.b [48].This is advantageous as there is no preferential direction for residual stresses, so the anisotropy of L-PBF-fabricated components can be reduced. In comparison to strategies like the zigzag pattern, which has longer scanning vectors, the island pattern induces lower stress throughout the part [15, 33].
- **Fractal Pattern** Is a scanning strategy through which a layer of short scan tracks are deployed with multiple orientations (Figure 1.15.c). This scan pattern results in only half the residual stress compared to the zigzag pattern. However, due to the complexities of the software implementations, it is not commonly used [48].
- **Helix Pattern** It starts scanning from the outside of the part and moves inwards or vice versa (Figure 1.15.d). Although this serves to reduce the scan vector length and alter the vector orientation, the magnitude of residual stresses is not that different from the zigzag pattern. However, it is suitable for processing complex models where the curvature changes a lot and every layer is irregular and inconsistent [48].

A critical concept that is defined within the scan pattern parameter is called **Hatch Angle** and requires close attention in order to reach the optimal process. The hatch angle θ is defined as the angle between laser scanning directions on consecutive layers, as shown in Figure 1.16a [17].

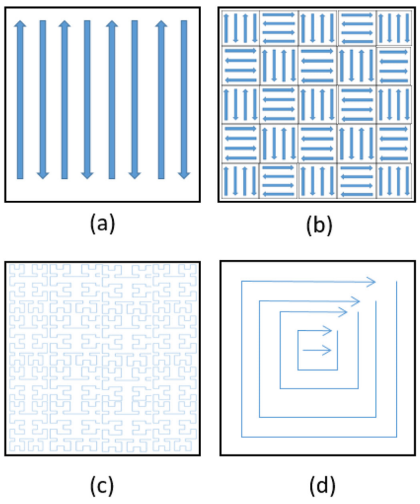

Figure 1.15: Most common patterns a.Zigzag b.Island c.Fractal and d.Helix [48]

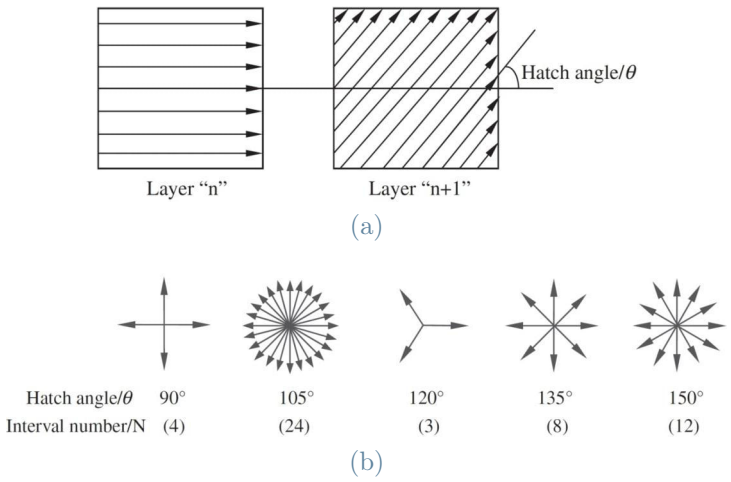

Figure 1.16: Illustration of Hatch Angle θ (a), The diagram of interval numbers (N) under different hatch angles (b) [17].

For instance, a hatch angle of 90 °, which is also applied in this thesis, means that the building surface at the end of the scan of the layer rotates 90 ° around the axis perpendicular to the surface, and then the next layer starts to operate. After the deposition of four layers, the orientation of the melted row in the fifth layer is the same as the rows of the first layer. Figure 1.16b indicated a parameter that in the literature is referred to as interval number (N), which indicates that after how many layers, the direction of the melting line matches the direction of the line in the initial layer depending on the examined hatch angle [15, 17, 27, 33]. As reported in the referenced study, the hatch angle of 105 ° in the SS 316L samples that are printed by the L-PBF method has the most satisfactory mechanical properties in many applications [17].

It is important to mention that the anisotropy of mechanical properties is difficult to remove, but the situation could be improved in the desired direction by selecting the optimal hatching angle[15].

Powder-related Parameters

Powder shape, size, and distribution are critical for a successful and repeatable process since they strongly influence laser absorption characteristics as well as powder bed density, powder bed thermal conductivity, and powder spreading [33].

Particle Shape Metal powders, produced by conventional methods like water atomization, might be angular, irregular, or agglomerated, which are unsuitable for L-PBF processes. Powders currently used in the L-PBF process most commonly have a spherical shape, allowing powder bed machines to spread a fine layer of powder evenly and deliver an inert gas-fed stream of powder smoothly without nozzle clogging.

Particle morphology has a significant impact on the powder bed packing density and, consequently, on the final component density. Spherical or regular, equiaxed particles are likely to arrange and pack more efficiently than irregular particles, where the more irregular the particle morphology, the lower the final density. This limits the use of potentially cheaper powder production routes such as HDH (Fig. 1.17.a) and gas atomization (Fig. 1.17.b), and more expensive powder manufacturing technologies with spherical shape powder production are preferred, such as plasma-based technologies (Fig. 1.17.c,d) [9, 15].

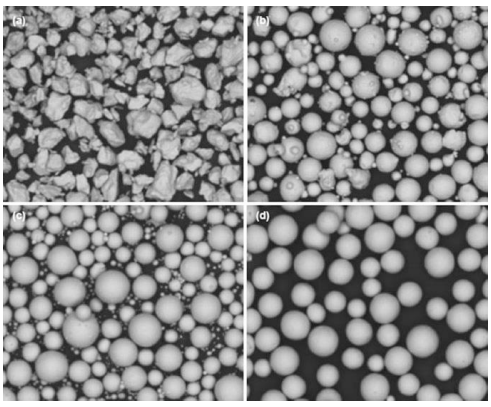

Figure 1.17: Typical particle morphologies obtained using (a) HDH process (b) gas atomization (c) plasma atomization and (d) plasma rotating electrode process [9]

Powder Size: Finer particles provide a larger surface area and absorb more laser energy than coarser particles. Finer particle sizes result in smoother, more precise components,

but they are more difficult to distribute and control. Larger particle sizes make powder processing and transportation easier, but they degrade surface quality, minimum feature size, and minimum layer thickness [15]. Metal powders generated by conventional methods, such as water atomization, have diameters varying from submicron to well over 100 microns, making them unsuitable for AM PBF procedures. The ideal powder size varies with the L-PBF machine, but it typically ranges from 15 to 75 microns [33]. It is important to note that the size of the powder affects the smoothness and thickness of the powder layer, which are critical parameters [13].

Particle Size Distribution (PSD): The particle size distribution of the powder used in L-PBF has an obvious impact on both the minimum layer thickness and the resolution of the finest detail in the component. L-PBF uses a finer PSD in comparison to EBM, which is between 15 and 45 microns. A wide PSD and a high fine content produce components with a higher fractional density, however, which could be dangerous from a health and safety point of view, especially in the case of using reactive powders like titanium [9, 13].

Flow Properties Powder flowability is a critical technological need in L-PBF, and the powder shape, size, and distribution are effective. The final part's density homogeneity is dependent on thin and uniform layers accurately deposited by the feeding system, which cannot be done in powder with limited flowability. Spherical or bigger particles are more free-flowing. Cohesive powders or the presence of moisture content cause poor flowability and make producing homogeneous density layers difficult [9].

Powder Bed Density Powder bed density, as determined by powder shape, size, distribution, and spreading process, can have a significant impact on part quality. Powder bed density for most commercially available powders is generally between 50 and 60% but can be as low as 30% for irregular powders. In general, the higher the powder packing density, the greater the heat conductivity of the bed and the better the mechanical characteristics of the component [15].

Layer Thickness: The layer thickness is also one of the four most critical parameters (Figure 1.14) that can not only have a significant effect on the process and final product quality but also affect other parameters and change their optimal values. For achieving the same energy delivery (Equation 1.1), the laser power, hatch spacing, and scanning speed should be alternated for different layer thicknesses [48]. The selection of an optimal and homogeneous layer thickness helps to control and improve the quality of the built

part. The use of a proper feeding system facilitates the control of the deposited layer [7].

Material Properties: Properties such as thermal conductivity, absorption coefficient, melting point, and coefficient of thermal expansion are intrinsic properties of the employed powder and cannot be classified as process parameters [24]. However, these properties can affect the process and need to be studied properly before the start of the process. For instance, the powder chemical composition can interfere with the surface tension of the melt pool, affect the melting kinetics, and cause porosity in the final product. The low thermal conductivity results in better accuracy as melt pool and solidification are more controllable, and part growth is minimized when heat conduction is minimized [9].

Temperature-related Parameters

Regarding the importance of the temperature-related parameters, it is universally accepted that the use of preheating during L-PBF reduces residual stress, and many studies even suggest that another laser could be used to locally pre-heat the powder [48].

Chamber Temperature It is noted in the literature that the temperature in the building chamber can be set between 22 and 300 degrees Celsius. The higher temperature is better since the flowability of metal powder is higher and benefits the creation of layers, and it is also easier to melt powder layers based on the preheating concept [24].

Powder Bed Temperature The powder bed temperature (Figure 1.14) should be uniform and constant to achieve repeatable results. For metals, the temperature ranges from 250°C to 500°C, depending on the material. Maintaining a consistent temperature prevents defects and provides heat dissipation and uniform layer formation [33]. A balance between bed temperature and laser power for high-laser-power/high-bed temperatures produces dense parts but can lead to part growth and poor recyclability. Low-laser power and low-bed temperatures produce better dimensional accuracy but may result in lower-density parts and layer delamination. Finally, high-laser power and low-part-bed temperatures can cause nonuniform shrinkage and an increase in residual stresses [15].

Powder Feeder Temperature The temperature of the powder feeder influences the consistent flow of the powder and avoids the clogging of the powder nozzle. The feeder temperature is adjusted, typically between 50°C and 70°C, to ensure a smooth powder flow into the build chamber [9].

Atmosphere-related parameter

The atmosphere in which the process takes place is the next important thing that can benefit the process in two ways. First, the protected environment prevents the passage of oxygen inside the chamber. The presence of oxygen can damage the component firstly through oxidation and secondly through reacting with the present carbon at the solidification step and generating prose. The most commonly used protective gases in L-PBF processes are nitrogen, argon, and helium. The correct application of the inert gas can allow the system to operate the oxygen-vulnerable materials, and the incorrect selection and application of a protective environment can lead to decarburization and a reduction in the hardness of the entire sinter, which has a negative effect on mechanical properties.

Other than oxidation prevention, as previously mentioned, the presence of a protective atmosphere affects the formation of plasma, and the weakening effect of the laser beam by the plasma is smaller for gases with higher ionization potential. As can be seen in figure 1.18, the differences in the depth of penetration of the material can be considerable, especially when used with a high-power beam [15, 24, 33]

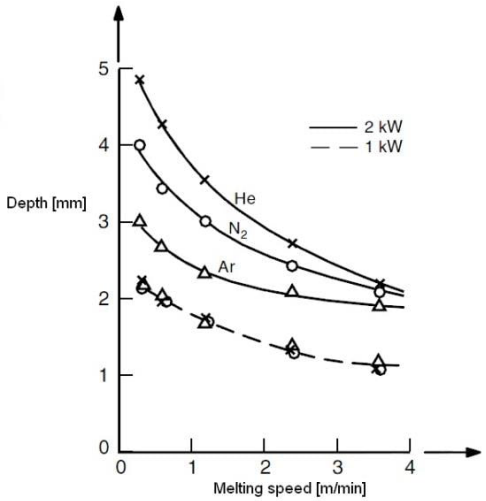

Figure 1.18: Effect of plasma on the penetration depth during melting process [24].

1.2.5. Parameter Optimization

In order to have superior parameter optimization, it is important to first know the main parameters and their effects individually that have been introduced in the previous section (1.2.4). Second, the effect of these parameters on each other and their interrelations is necessary to know since most of these parameters are strongly interdependent and mutually interacting. Finally, the defects that can be generated in the L-PBF due to incorrect

parameter selection need to be discussed, as they can reveal the incorrect parameter.

Parameters Interrelation

A trial-and-error method in the development of process parameters may be required to optimize the deposited material and minimize defects [33]. In this regard, lots of studies have been carried out in recent years that investigated these relations and discussed the effect of main parameters on defects, the quality of the product, and the mechanical properties. Due to limitations, the focus of the current section is only on the most important parameters that have been studied repeatedly in multiple studies.

The main process parameters of the L-PBF in most of the literature are the laser power (p), the scanning speed (v), the hatch spacing (h), the thickness of the layer (t), and the scan strategy, which were earlier schematically represented in Figure 1.14. In early developments, these parameters are used to calculate a fundamental process parameter called Volumetric Energy Density (VED), which defines the amount of energy that is delivered to the powder bed and is calculated by equation 1.1 [7, 48].

$$VED = E_p = \frac{p}{v \cdot h \cdot t} \tag{1.1}$$

In this simplified model, applied energy increases with increasing laser power and decreases with increasing velocity, scan spacing, and layer thickness. It should be considered that this equation only provides the simplest analytical approach since does not include powder absorptivity, the heat of fusion, laser spot size, bed temperature, or other parameters [15].

The interrelation of the parameters is challenging because the change of each single parameter affects the others, the whole system, and thus the final product [7]. For this reason, it is essential to keep all the parameters constant while one or two understudy parameters vary which is the methodology of most of the studies. A few case studies are introduced in the following paragraphs.

Figure 1.19, as a first case study, studied the amount of porosity for different sets of parameters to define the optimal combination of laser power and scanning speed in a constant layer thickness and also the effect of layer thickness on the same combination parameters. As a result, the increase in laser power reduces porosity at the same scanning speed, and similarly, but more significantly, the increase in scanning speed at the same laser power leads to reduced porosity. On the other hand, the same laser power and scanning speed values for the lower layer thickness in comparison to the higher layer thickness indicated that the lower layer thickness causes lower porosity [24].

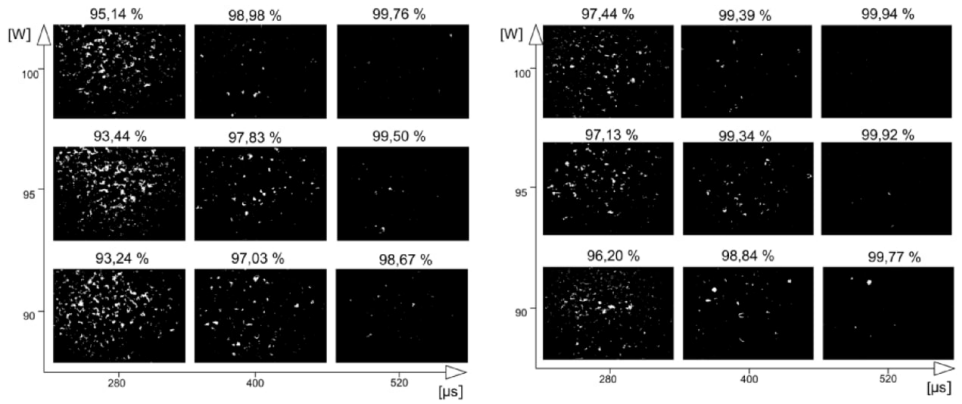

Figure 1.19: Influence of Laser power, scanning time, layer thickness: 80μm distance between scanning, a) 75μm layer thickness (left), b) 50μm layer thickness (right) [24].

Another study indicated in Figure 1.20 shows the images of the 12 L-PBF printed single tracks of stainless steel 316L. The study investigated the influence of scanning speed and laser power on the coherency of the printed track individually. As reported by the author, the laser spot size (55 μm) and layer thickness (75 μm) were kept constant throughout the experiment. Having a close look at the result indicates that the increase in scanning speed is not desirable for neither of the laser powers and for 100 W laser power, a continuous track at 100 mm/s scanning speed and 242 L/mm^3 energy input (Eq. (1.1)) turns to an irregular track at 200 mm/s speed and 242 L/mm^3 energy input and at the end has a balling effect at the 500 mm/s speed and low 48 L/mm^3 energy input. Similarly, it is reported that increasing the laser power for similar scanning speeds is not desirable [46].

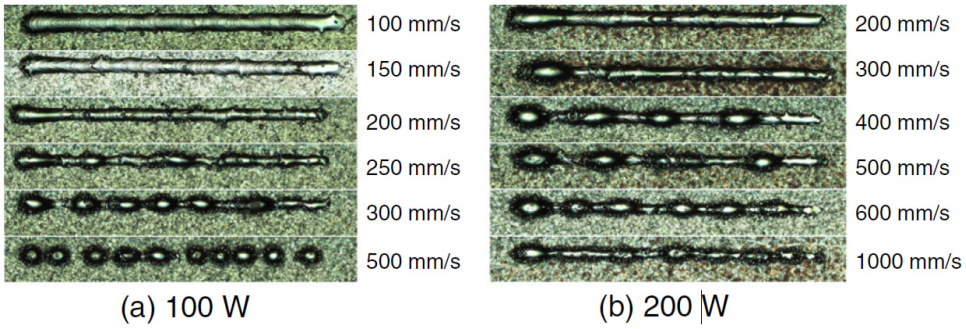

Figure 1.20: Influence of Scanning speed on printing consistency [46].

The other relevant study is the investigation of the layer thickness influence on the level of porosity shown in Figure 1.21. As reported by the author, the overall porosity and the size of pores increase continuously with increased layer thickness. As shown in the graph, there is little effect on porosity for layer thicknesses between 20 and 40 μm as the optimal

value. However, at 60 μm, the top surface displayed open pores, thus increasing porosity considerably for layer thicknesses greater than 60 μm [48]. It is well-accepted that the stability, dimensions, and behavior of the melt pool determine the extent of porosity. Therefore, as also previously mentioned in the first introduced case study (Figure 1.19), laser power and scanning speed which have the greatest effect on the melt pool, have the maximum influence on the induced porosity [15, 24, 48]

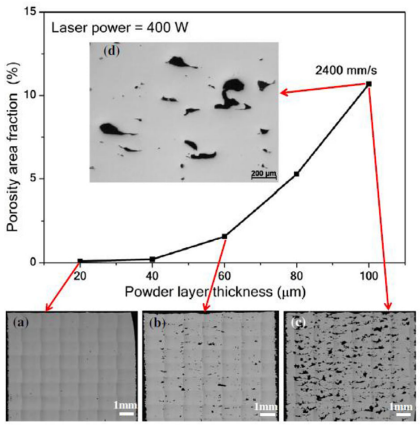

Figure 1.21: Influence of powder layer thickness on porosity [48].

The results of the final case study regarding the effect of parameters' interaction is presented in Figure 1.22, investigated the influence of hatching space and layer thickness. It is confirmed by experimental data that the layer thickness (t) and the hatching space (H), which both have a reverse relation with the delivered energy to the powder bed (Eq. 1.1), have a reverse relation with each other. It is well accepted that to acquire the same results, an increase in hatching distance requires a decrease in layer thickness since the VED is decreased [7].

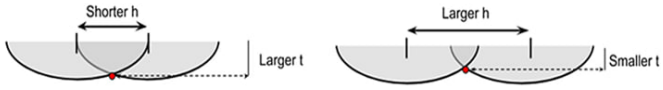

Figure 1.22: Influence of process parameters on lack of fusion defect [7].

To sum up, the optimization of process parameters is a unique task that should be done exclusively in each project through consideration of all the external and internal effective variants, such as material properties, L-PBF machine, goal applications, and desired mechanical properties. The mentioned case studies are introduced only to have a clear vision of the effect of parameters on each other; otherwise, the mentioned values are highly dependent on the material properties and other parameters.

Defects

Porosity is the most common defect encountered during an L-PBF process and can be distinguished in several configurations, which are caused by incorrect process parameter selection. Figure 1.23 is an indication of the areas where an ideal product or a component with a specified type of porosity exists, which is a function of laser power and scanning speed. However, this graph is schematic, and each L-PBF material needs to have an exclusive map including more parameters to achieve a defect-free structure [7, 15].

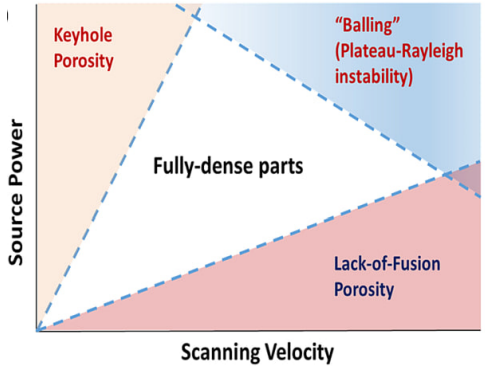

Figure 1.23: Influence of process parameters on defect of SLM technology [7].

A brief review of the most commonly identified porosities and other defects in L-PBF products is given in the following lines:

- **Balling Defect:** Too little delivered energy to the melt pool or too short a time of laser melting can cause balling phenomena, leading to an incomplete and disconnected laser track [7].
- **Microstructural Defect:** The incorrect selection of process parameters and the formation of dendritic structures are undesired segregations and precipitations during the process. The existence of alloying element segregation zones and undesirable phases might cause a component to fail during the operational phase [7].
- **Lack of fusion:** Is one of the more common defects that occurs when insufficient energy is applied, leading to incomplete fusion of the metal powder into adjacent tracks or the substrate and can be avoided through reduction of hatch spacing or layer thickness and also reduce scan speed or increase laser power [7, 33].
- **Satellites Defect** In the occurrence of this defect some solid powder grains that are connected with the melt pool do not melt and are surrounded by the liquid metal and trapped inside the solidified part [24].

- **Shrinkage and distortion:** Occurs as a result of localized melting and solidification. The result stresses can increase and lead to warping and distortion. Proper design and selection of materials and parameters can reduce or eliminate the risk of this defect [33].
- **Metal Evaporation:** The very high delivered energy causes the evaporation of alloying elements at very high temperatures. These defects can cause a change in the chemical composition of the final component and also decrease its mechanical properties. This can be prevented by reducing laser power, increasing scan speed, and increasing hatch spacing or layer thickness [7, 15].
- **Keyhole Deffect:** This is a void or pore that can result from incomplete melting and fusion of powder particles and may compromise the structural integrity of the part but can be avoided by reducing laser power or increasing scan speed [7].

There are a variety of different defects that can be induced in the L-PBF products and affect the surface quality and mechanical properties of the final product, which are not covered in this part, but it is essential to comprehend these defects to have the proper optimization of process parameters and achieve optimal results.

1.2.6. Conclusion

In conclusion, Laser powder bed fusion (L-PBF) also called Selective Laser Melting (SLM) stands as a transformative force in additive manufacturing technology that is driving its adoption across the globe through offering various advantages like reduced material waste and enhanced design freedom, besides its ability to create complex and high-performance components.

However, similar to any other technologies, L-PBF still has shortages and there are more fields to be developed such as high equipment costs and the complex parameter optimization to achieve desired results. L-PBF with its versatility is reshaping various industries and extending its application list in aerospace, healthcare, automotive, and many other sectors day by day versatility. A thorough understanding of the printing parameters and their optimization is crucial for achieving the full potential of L-PBF in the manufacturing sector. The future of L-PBF is undoubtedly promising. Researchers and engineers are continuously working to fine-tune parameters and materials and push the boundaries of current limitations. As the L-PBF process evolves, an even wider range of applications, materials, and phenomenal properties are expected.

1.3. Lattice and Porous Metallic Lattice Structures

Introduction

In recent years, the manufacturing of metallic lattice structures has become increasingly feasible with improvements in additive manufacturing technologies such as electron beam melting (EBM) and Laser powder bed fusion (L-PBF) [50]. Lattice structures together with porous metal lattice structures manufactured by Laser powder bed fusion (L-PBF) have received increasing interest in the scientific community over the last few years because of their advantageous stiffness-to-weight ratio, a wide range of possible applications, and their difficult producibility by other means of manufacturing. Applications ranging from shock absorbers, heat exchangers, medical implants, acoustic dampers, and lightweight engineering have made the metallic lattice structure an interesting research field [16, 56].

Despite many definitions that have been provided for lattice structure, there is still no unified description, because the structure of lattice is not limited to only changing the size of struts and connection mode of cells. However, as introduced in the literature, lattice structures are three-dimensional structures composed of consecutively and repeatedly arranged interconnected cells [34].

To provide sufficient knowledge for the advancement of this thesis, this section of the first chapter is dedicated to reviewing the current state of the art in L-PBF-produced lattice and porous metal lattice structures, with an extended focus on their advantages and drawbacks, applications, mechanical properties, and controllable process parameters.

1.3.1. Cellular Materials

Initially, it is important to note that the lattice structure, which is the main topic of this research, is a subcategory of a larger material class called cellular structure materials. As a general definition, a cellular material is composed of many repeating unit cells. The main cellular materials presented in classic literature are honeycomb and foam structures [34]. However, as indicated in Figure 1.24, the modern cellular material is divided into stochastic and nonstochastic classification based on the spatial arrangement of the unit cells. Stochastic cellular materials are often referred to as open and closed foams in the literature. On the other hand, the indicated nonstochastic 2D class is mostly referred to as a honeycomb structure [50]. A brief description of these concepts is provided.

Stochastic Foams: Also called open- or closed-cell foams, they are characterized by unit cells where the specific topology cannot be precisely controlled and have a random-

ized, heterogeneous structure. This random, irregular structure in shape and orientation provides exceptional properties and performance for various applications. The porosity of the foam structure ranges from 40% to 98% [34, 41]. Open foams have energy-absorbing capabilities, while closed foams are usually characterized by stiffness and strength [50].

Honeycomb Structures: In contrast to foam structures, honeycomb configurations are known for their regularity. Unit cells within honeycombs possess the same shape, resulting in two-dimensional cellular structures with a consistent geometry. The possibility of various cell shapes offers innovations that enhance performance and broaden the range of applicable applications [34, 41].

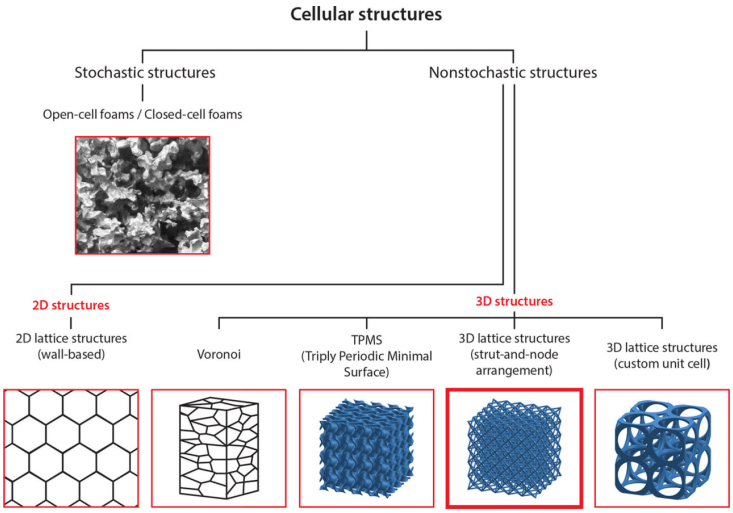

Figure 1.24: Cellular Structure Classification [50].

Finally, the nonstochastic 3D structure is the lattice structure that is different from foams and honeycombs, and the difference in structure mainly lies in unit cell topology, scale, and properties [50]. In fact, compared with foams and honeycombs, lattice structures have better mechanical properties and can improve compressive and shear strength which is discussed in deep detail in the following parts.

1.3.2. Lattice Design

Investigating lattice structural components reveals that design is a crucial step that significantly affects the quality of the final product. It has a notable impact on the mechanical properties, density, and weight of the produced component, and on the other hand, proper design and optimization of the lattice structure can save energy, material, and time in the manufacturing process thus reducing the finishing costs. [21, 34]. The design of the lattice

structure can be divided into two different steps that have to be looked at individually. The primary step is the design of the unit cell, which is highly effective on the mentioned parameters. The second step is the arrangement of the designed unit cells in order to form the goal lattice structure.

Starting with the possible arrangements of designed unit cells, multiple authors divided lattice structures into three categories regarding this subject [41]:

1. Random lattice structures: A random distribution of unit cells in the design space with different topological structures and sizes (Fig. 1.25.a).
2. Periodic lattice structures: A periodically repeated arrangement of lattice cells with certain shape, topology, and size (Fig. 1.25.b).
3. Pseudo periodic lattice structures: A periodic repeated arrangement of unit cells that only have the same topology but whose size is different (Fig. 1.25.c).

There is also a class of lattice structure named graded lattice, which shows a gradient in the size of the unit cell inside the structure [50]. Graded lattices have gained significant attention in recent years with the development of additive manufacturing for specific applications like metallic filters and have been extensively studied in the literature [58, 62].

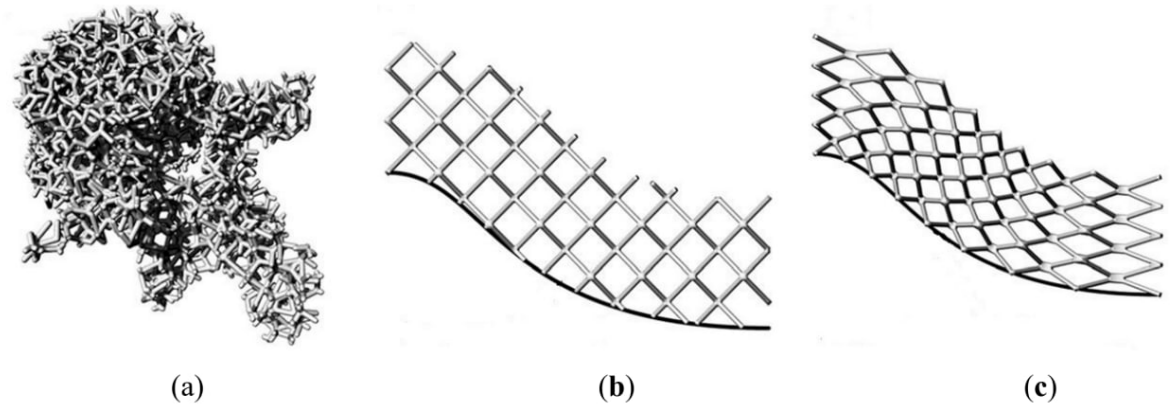

Figure 1.25: Classification of lattice structures (a) Random lattice structures (b) Periodic lattice structures (c) Pseudo periodic lattice structure [41].

As can be seen in Figure 1.24, there are four main categories for the possible design of unit cell and lattice structure in non-stochastic 3D class, Voronoi, TPMS, Strut-and-node arrangement, and Custom unit cell. Strut-based unit cells consist of a network of often prismatic struts connected at nodes, similar to truss structures. Surface-based unit cells are mathematically defined as the surface connecting a set of points for which a given

function has a constant value, that is, an iso-surface [50].

Different forms of lattice structures have been designed so far and implemented by AM methods like SLM, EBM, SLS, and SLA, among which SLM, due to its capabilities that were previously mentioned, is the optimal manufacturing method for metallic lattice structures. Based on the literature review, multiple materials employed by the SLM method for lattice preparation can be noted as Ti-6Al-4V, AlSi10Mg, CoCr alloy, In718, and Stainless Steel 316L [3, 34, 41].

It is important to mention that the combination of each of the above-mentioned materials, design approaches, and manufacturing methods has exclusive beneficial characteristics that lead to superior mechanical properties. For this reason, it is important to study the performance of each design with the specific material and production method that suit the goal of the research. To be more focused, only the most common strut-and-node designs are addressed based on the case studies that have been done on L-PBF-produced stainless steel 316L lattices.

As can be seen in Figure 1.26, the most commonly used unit-cell designs in the literature with the Strut-and-Node design are introduced as Body-Centered Cubic (BCC), Body-Diamond, Tetrakaidecahedron [62], Face-Centered Cubic (FCC), Vertex-Centered (VC), and Edge Center Cube (E) [59]. Other dominant lattice designs can be mentioned as Body-Centered Cubic with Zigzag (BCCZ) [50] and Hexagonal Close-Packed (HCP) [51].

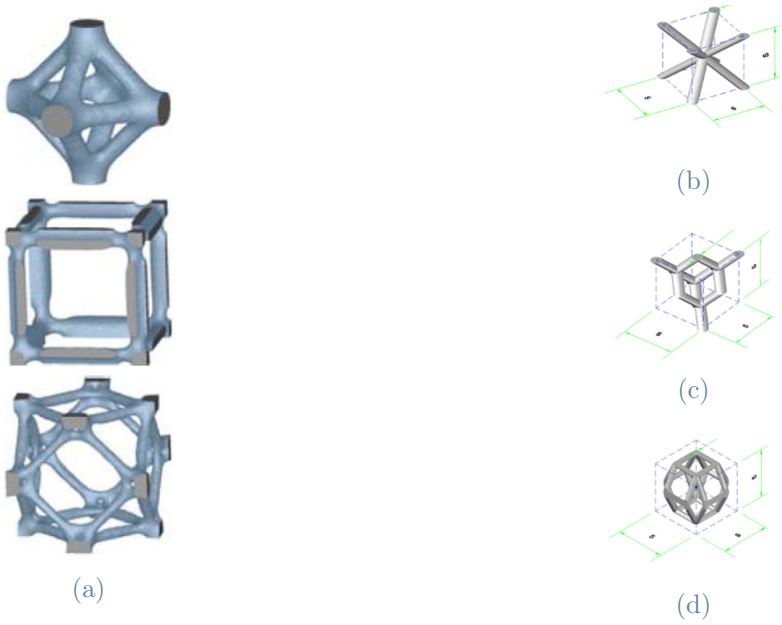

Figure 1.26: Lattice unit cell design patterns FCC, VC, ECC (Left, from top to bottom) [59], (b) BCC, (c) Diamond, (d) Tetrakaidecahedron [62].

Starting with the study of L-PBF-produced lightweight SS 316L lattice structure produced from FCC, VC, and ECC unit cells (Fig. 1.26a), the author reported that the FCC and VC lattice structures have better mechanical properties than the ECC lattice structure. However, the ECC structure has the highest energy absorption efficiency, and a slightly higher young modulus has been reported for ECC in high relative densities [59].

Considering the second case study on L-PBF-produced SS 316L lattice structures produced from BCC (Fig. 1.26b), diamond (Fig. 1.26c), and Tetrakaidecahedron (Figure 1.26d) unit cells, the tetrakaidecahedron structure revealed higher mechanical properties and better energy absorption performance than the diamond and BCC structure [62].

The last introduced case study followed a different approach to lattice design; however, the design and results are briefly mentioned in the following paragraph since it is a unique design and could be considered as a direction to be followed in future studies. As can be seen in Figure 1.27, this article studied the five different lattice structures that have been designed by different combinations of BCC (blue) and HCP (grey) unit cells and compared them to the lattices made by only BCC or HCP unit cells.

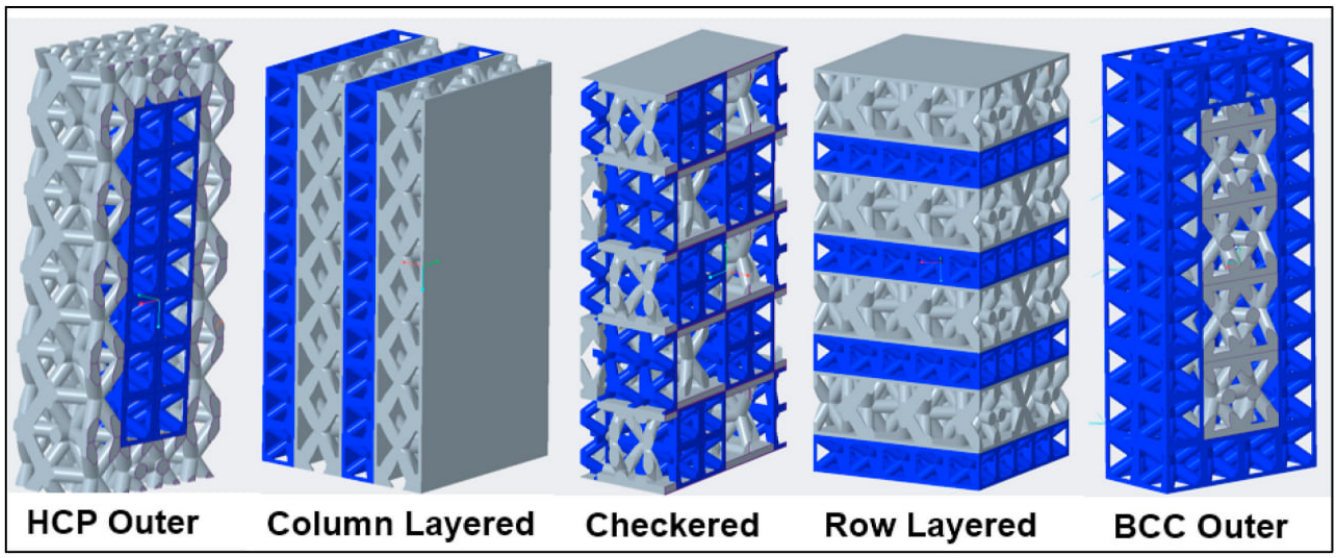

Figure 1.27: CAD representations showing the five designs used in this study [51].

As reported by the author, the values of the compressive test have indicated that the column-layered design has the best performance among all the groups, and the row-layered and checkered lattice have the second and third best yielding and ultimate stress values with respect to other designs [51].

1.3.3. Properties and Parameters

Functional and Mechanical Propeties

Lattice structures have fundamental characteristics that make them an optimal choice and, in certain applications, the only viable option. For optimization of the functionality of these structures for a broader range of applications, it is essential to monitor the critical mechanical properties that can be improved or negatively affected by the process parameters or lattice design. These properties can be briefly described as [30, 34, 41, 62]:

- Compressive Strength: Lattice structures have lower compressive strength than solid structures, but they are an excellent choice since they match the application requirements while using less material.
- High Stiffness: An optimal lattice design should provide the necessary stiffness to support intended loads while maintaining flexibility.
- Fatigue Resistance: It is crucial for lattice structures subjected to cyclic loading. and optimized lattice designs should minimize stress concentrations.
- High Energy Absorption: The total cumulative energy absorption per unit volume was higher in a functionally graded lattice than in a uniform lattice.
- High Damping Effect: An optimized lattice should deploy the high-damping effect required by the goal application.
- Heat Dissipation: Thermal stability and heat dissipation are more important in high-temperature or fluctuation temperature applications.

Parameters

As mentioned, unit-cell design and arrangement inside the lattice are highly effective parameters in achieving the optimal goal properties. One of these important parameters in the design of a lattice is the level of porosity that each unit cell has. The porosity level can be controlled by the thickness and diameter of the struts [50].

The lattice production through L-PBF can affect the final quality through laser technology, process parameters, laser scan strategy, and interface with design software [34]. The details of L-PBF process parameters are discussed in detail in 1.2.5, and only a few important parameters that affect the lattice structure are quoted in the following paragraph.

The author of the referenced chapter reported that the excessive-high linear energy density (LED) [J/mm], which represents the amount of energy delivered by the laser per unit length of the single scan tack, affects the mechanical properties of the structure through

the generation of pores in struts that are fabricated by L-PBF. The LED is calculated by dividing the laser power (p) by the scanning speed (v) as indicated in Equation 1.2 and needs to be optimized based on desired energy delivery [49].

$$LED = \frac{p}{v} \tag{1.2}$$

Another study found that as distinct energy inputs result in variable-sized melt pools, increased energy input results in a wider melt pool and a larger strut diameter. However, physical phenomena in the melting process occur in the surrounding areas, resulting in keyholes and lack-of-fusion pores, balling, particle adhesions, or wavy struts [16]

1.3.4. Benefits and Drawbacks

Lattice structures, mainly metallic lattice structures, have proven advantages that can be mentioned, such as their lightweight nature, high strength-to-weight ratio, and superior thermal management properties that promote efficient heat dissipation and minimize thermal stresses. On the other hand, their customizable designs allow for optimizing mechanical properties to meet specific needs and minimize material waste. The production of lattice structures by AM technologies maximizes these advantages and allows local, precise, and automatic control of the material distribution within the design space [30, 50].

To be mentioned, there are also disadvantages regarding lattice structures, such as the complexity of designing effective lattice structures that require specialized knowledge and computational tools and can cause high costs and processing time. In addition, this complexity should be compromised to be in balance with structural integrity. The other drawback, in close relation to the L-PBF parameters and scanning strategy, is that lattice structures may exhibit anisotropic mechanical behavior that is not desired [50]. Another shortcoming in L-PBF-produced lattices is the possible need for support materials, which causes certain material waste and increases post-processing time [33].

1.3.5. Applications

It is required to note that all the following applications are the applications of L-PBF-produced lattice structures that provide superior functionalities. The main applications that are highly studied in literature can be mentioned as:

- **Biomedical:** Medical devices, surgical aids, and implants are being approved for use and can be matched to a person's anatomy. Unique surfaces, biocompatibil-

ity, high strength, and light weight offer benefits for bone ingrowth and biological integration [50].

- **Aerospace and Automotive:** Lattice structures are widely accepted in these fields due to their lightweight and high strength. The weight decrease means better performance with less fuel consumption, especially in aircraft and race cars. The lattice structure is also widely used as the core of multiple structures in aerospace, like wings. Functionalities in aerospace concerning heat exchange and acoustic insulation capabilities are desired sectors to use the lattice structures [33, 34, 41].
- **Construction:** The lattice structure is used as the core of the beam and sandwich panels in many sectors as a desired application due to its lightweight and high stiffness [34].
- **Heat transfer:** Concerning the heat transfer capabilities of these structures, the high area-to-volume ratio, on the one hand, and the high number of internal voids, on the other, significantly increased the use of lattice structures for heat exchangers, cooling channels, and energy-absorbing applications [33, 34].
- **Industrial** lattice structures are used for filtration in a very broad range of industries because of their possibility to have a high number of voids with the possibility to orient them to reduce pressure drops [34].

1.3.6. Porous Metallic Lattice Structures:

Porous metallic lattice structures are characterized by a three-dimensional network of interconnected struts and void spaces, forming a lightweight and high-surface-area framework [33]. The regularity in the arrangement of pore units provides the properties for porous lattice structures that are difficult or impossible to include in porous structures with stochastic pores [30].

As previously mentioned for lattice structures, similarly, the lattice and pore arrangement design plays a crucial role in determining the mechanical properties and performance of porous metallic lattice structures [30]. The design principles are slightly different for porous lattice structures, and in this regard, Figure 1.28 indicates the main specific structures for porous metallic lattice materials, including some of the most common pore unit configurations [30]. It is important to mention that different lattice configurations offer distinct mechanical characteristics and can be tailored to specific application requirements.

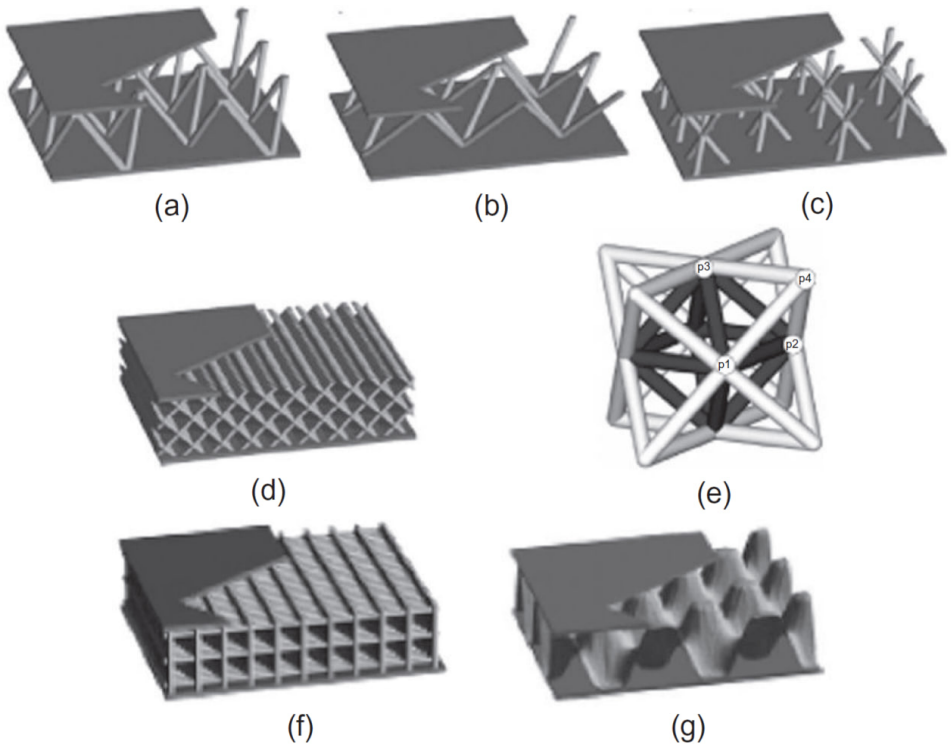

Figure 1.28: Schematic illustrations of porous metallic lattice structures (a) tetrahedral (b) pyramidal (c) 3-D-kagome (d) diamond (e) octahedral (f) hollow (g) egg-box [30].

Manufacturing: The main porous structure manufacturing technologies primarily included investment casting, metallic wire weaving, metallic wire assembling, polymer forerunner electrodeposition, thermal spray, and chemical vapor depositions (CVD) [10, 30]. However, additive manufacturing, mainly L-PBF and EBM, has become the optimal manufacturing method in this field in recent years. The use of L-PBF for the production of these structures is a valuable asset that highly improved the free design and controlled producibility of complex pore arrangements in this field, which was not accessible to this level by the conventional manufacturing method.

Advantages and Drawbacks: One of the key advantages of porous metallic lattice structures is their exceptional mechanical strength and stiffness, coupled with their low density. Moreover, porous lattice materials can achieve maximum performance because of their regular pore shape and periodic pore arrangement, which can be theoretically calculated. However, achieving a balance between structural integrity and porosity is essential, and factors such as lattice unit cell design, strut size, and interconnectivity influence mechanical behavior, which is highly improved by the use of L-PBF but still needs to be studied and optimized. Post-processing treatments may be required to enhance the material properties and mitigate potential issues like surface roughness [33, 34].

Applications Porous structures are primarily intended to be used in medical applications due to their similarities to natural organs. With recent developments in the production methods of porous metallic lattice structures, various applications have been introduced besides medical implants. Porous metallic lattices have a uniform permeation capability and can be used to make different kinds of industrial filters, gas purification separators, and fluid distributors. Also, because of their large specific surface area, they can be used in electrodes, catalysts and their carriers, capacitors, and especially in heat exchangers [7, 30]. Moreover, these materials, due to their lightweight and shock- or sound-absorbing properties, are highly used in the aerospace and automotive industries, especially the race car industry[34].

Important Setting One of the important settings in the lattice design and L-PBF process parameters that significantly impact the mechanical properties of the final product is the previously introduced concept, Hatch Angle (1.2.4), which refers to the rotation degree of the work surface by the end of the printing process of each layer.

As can be seen in Figure 1.29, which indicates the two common 45 and 90-degree hatch angles, this parameter plays a crucial role, and as is discussed in this thesis, it has a great impact on the result properties and also implies changes on the surface and also porous direction, which can impact the filtration of absorbing properties through changing the specific surface area, which is not the focus of this study.

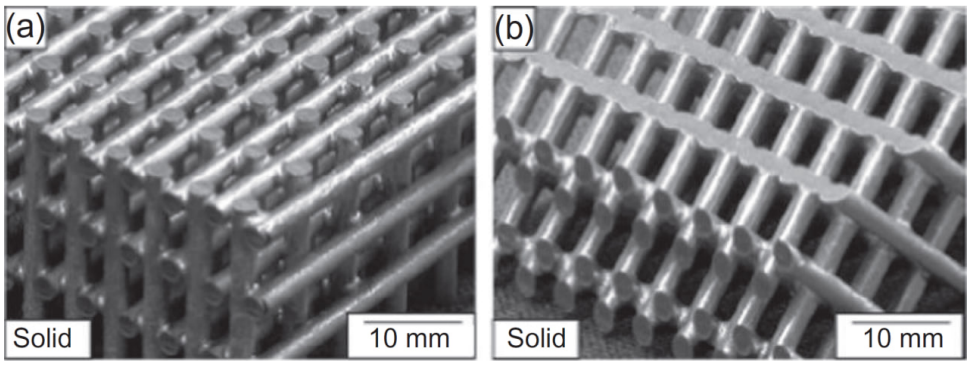

Figure 1.29: Porous lattice structures (a) Square orientation (90°), (b) Diamond orientation (±45°) [30].

1.3.7. Compression Behaviour

The general deformation behavior of lattice structures during compression testing can be classified into three stages: (I) linear elastic deformation, (II) plastic deformation, and (III) compacting. It can be said from the acquired result of this thesis and based on

the scientific definition of compression testing that the first and third stages are shared between all the structures, regardless of their topology and printing parameters. Within the plastic deformation stage, the deformation behavior can be broadly categorized into two regimes: bending-dominated and stretch-dominated behaviors. These deformation modes are schematically shown in the stress-strain diagram in Figure 1.30 [11, 25].

- **Bending-dominated Behavior:** Deformation predominantly occurs through the bending and buckling of lattice struts. Struts bear the load, and the deformation is characterized by flexural responses similar to slender columns undergoing buckling. Compression forces induce bending and buckling, leading to a relatively continuous deformation until a critical load is reached, possibly resulting in catastrophic buckling. This behavior is often associated with effective energy absorption, making it suitable for applications requiring controlled deformation, such as impact absorption or crash resistance.
- **Stretch-dominated Behavior:** Deformation is primarily governed by the stretching or axial elongation of lattice struts. The lattice structure experiences elongation in the direction of the applied compression force. Stretch-dominated behavior is characterized by a relatively linear and elastic deformation response during the initial compression stages. It is desirable in applications where controlled and reversible deformation is crucial, such as in structural components that need to recover their original shape after deformation.

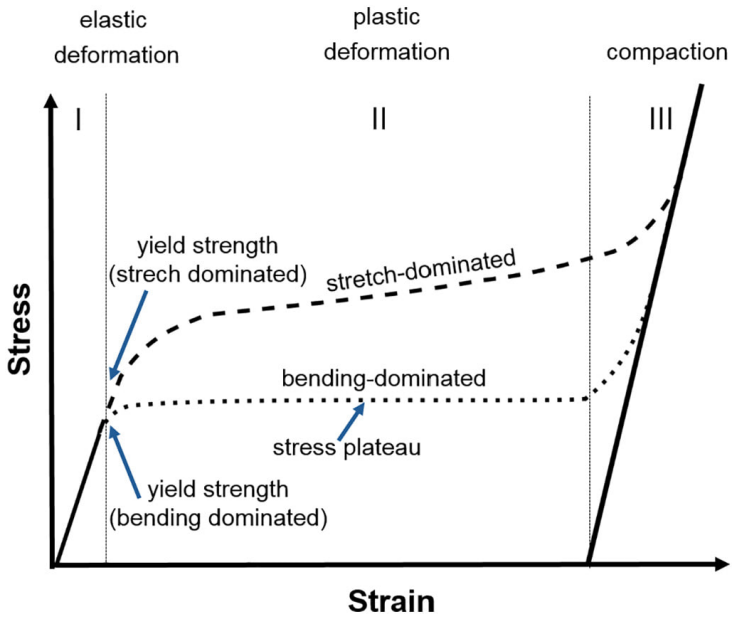

Figure 1.30: Schematic compression stress-strain curves of a bending-dominated and a stretch-dominated lattice structure [25].

Microlattice structures may exhibit transitional behaviors between bending-dominated and stretch-dominated responses based on factors like lattice geometry, material properties, and loading conditions [25]. The choice between bending-dominated and stretch-dominated behavior depends on the specific application requirements. Design considerations, including lattice topology, strut dimensions, and material properties, play a crucial role in optimizing the microlattice structure to exhibit the desired mechanical behavior.

Both of these deformations have been identified in the understudied samples during the experimental steps of this thesis, and the results are discussed in Chapter 3.

1.3.8. Conclusion

Finally, the investigation of lattice and porous metallic lattice structures is considered an important step forward in the field of advanced materials and additive manufacturing. This chapter, through discussing the background, design considerations, mechanical characteristics, benefits, drawbacks, and numerous applications of lattice structures, highlighted their huge effect on the aerospace, medical, energy storage, and automotive industries. The adaptability of these structures, with their adjustable features and large surface area, provides new opportunities for innovative technical solutions. Furthermore, the developing landscape of lattice and porous metallic lattice structures promises continuing progress, influencing the future of materials engineering and additive manufacturing approaches. As investigations continue, the potential for discovering new applications and improving existing ones grows, creating an evolving sector with long-term relevance. Besides all these optimal features, further developments in metal additive manufacturing promote the evolution of the lattice structure application to new industries that were not applicable to their conventional manufacturing methods.

1.4. Stainless Steel

1.4.1. Introduction

Stainless steels are alloys of iron, chromium, and other elements that resist corrosion in many environments. As defined in the handbooks "stainless steels are steels with at least 10.5% chromium that exhibit passivity in oxidizing environments" [5]. The chromium concentration is a critical parameter since, as it increases, the corrosion rate decreases.

The major microstructural components possible in steels are the following:

1. **Ferrite:** BCC iron.
2. **Cementite:** an iron-carbon compound, Fe/C.
3. **Pearlite:** a lamellar composite of ferrite and cementite.
4. **Austenite:** FCC iron.

The major limitations of stainless steel can be mentioned as that they are prone to pitting, susceptible to crevice corrosion, prone to stress corrosion cracking in halogen, susceptible to intergranular attack when sensitized, and are susceptible to galvanic corrosion [5, 36].

Various welding problems exist in stainless steel, especially with ferritic and martensitic steel. The ferritic is prone to grain growth at welding temperatures, and the martensitic forms hardened martensite during the quenching action that can follow welding, both of which result in crack initiation and a decrease in strength. On the other hand, austenitic has excellent weldability in almost all welding processes and its only remaining problem is sensitization [5].

Austenitic stainless steels, or series 300, are significantly more complex than ferritic and martensitic and have at least four major alloying elements: iron, chromium, carbon, and nickel. The carbon content is as low as it is commercially feasible to obtain; chromium can range from 16% to 26% and nickel content is usually at least 8%, but can be as high as 22%. The effect of the nickel is to promote a completely austenitic structure. Although certain grades of stainless steel in the temperature range of 400°C to 850°C show local chromium depletion and a corresponding loss of corrosion, some austenitic steel grades such as 304L and 316L are perfect options for welding applications due to their lower carbon content [5, 36] and the 316L is discussed further in the following section.

1.4.2. Stainless Steel 316L

316L stainless steel, is austenitic steel that is classified in the chromium-nickel group based on the classification given by Budinski G. M. [5]. The SS 316L is characterized by solid-point corrosion resistance and is widely used in pipelines, the food industry, marine and biomedical equipment, fuel cells, and other fields. The chemical composition of stainless steel is given in Table 1.1, and as can be seen, it has about 2% molybdenum in it to improve corrosion characteristics in reducing media and to improve pitting resistance [5, 36].

Element	C	Mn	P	S	Si	Cr	Ni	Mo	N
Composition [%]	0.030	2	0.045	0.030	1	16-18	10-14	2-3	0.10-0.16

Table 1.1: Stainless Steel 316L Chemical Composition [5].

Type 316L is the optimal stainless steel to use for chemical services where sensitization may be a problem. If a structure will need a stress relief heat treatment, this grade is the best to use. The same thing is true if a given structure involves high welding heat inputs. Shielded metal arcs provide the lowest heat input in moderate-section-thickness weldments [36]. All these chemical properties, besides its excellent high-temperature strength, non-magnetism, and perfect weldability, made the stainless steel 316L an optimal material to be used in metal additive manufacturing methods, especially in Laser powder bed fusion (L-PBF) [25, 29].

1.4.3. Stainless Steel 316L in L-PBF

In Laser powder bed fusion (L-PBF), the choice of materials plays a crucial role in determining the quality of the printed parts. Although the development of L-PBF has gradually accelerated and is becoming more commercialized, there are still few available metal materials. However, in recent years, 316L stainless steel has gradually become the raw material of L-PBF 3D printing technology due to its excellent mechanical and thermal properties and relatively low costs, which make it suitable for a wide range of applications [13].

The other reasons for choosing SS 316L over other common materials in L-PBF could be mentioned as [10, 13, 39]:

- Outstanding mechanical properties such as high tensile strength, excellent ductility, and impressive fatigue resistance.

- High corrosion resistance, particularly in aggressive environments.
- Great biocompatibility makes 316L invaluable for biomedical applications.
- The low carbon content provides enhanced weldability and minimizes the risk of carbide precipitation.
- SS 316L's thermal properties align well with the L-PBF process requirements, facilitating efficient energy absorption during laser melting.
- Good compatibility with post-processing treatments, providing optimization possibilities for its microstructure and properties.

It is important to quote from the referred case study, that the typical microstructure deriving from an additive process for 316L is composed of elongated dendritic grains along the building plane. This particular microstructure gives superior mechanical properties to the as-built material [7].

These properties, besides the fact that 316L is easy to manufacture with L-PBF in comparison to other common L-PBF materials like Ti6V4 and AlSi10Mg/AlSi12Mg [34], make 316L an ideal choice for a vast range of applications in medical, aerospace, automotive, and many other industries.

However, there are possible problems that can be identified in the stainless steel 316L L-PBF-produced samples. A few case studies in this regard are reported in the following.

- A reduction in tensile strength is detected by the author and is defined to be induced because of partially melted powder particles in the microstructure. It is suggested in the literature that, to solve this problem, laser remelting could be applied. The study proved that the density of stainless steel parts could be improved and the surface roughness could be reduced by the secondary scanning method, thus improving the fatigue characteristics [29]. This result is valuable proof of the effect of the scanning strategy on the mechanical properties.
- The other case study reported that 316L stainless steel printed with L-PBF technology showed anisotropy in notched high-cycle fatigue behavior and fatigue crack [25].
- Finally, universal research on 316L stainless steel using L-PBF technology shows that the density state of stainless steel cannot be guaranteed due to certain porosity between stainless steel powders, which can cause internal defects in the parts printed with 316L stainless steel, affecting the overall service life of the parts and even leading to parts being scrapped. [13].

1.5. Conclusion

In conclusion, the state-of-the-art exploration reveals a comprehensive understanding of the fundamental and existing knowledge in the field of Laser powder bed fusion (L-PBF) optimization for stainless steel 316L porous microlattices production.Laser powder bed fusion (L-PBF) as a dominant additive manufacturing method that revolutionized the AM market, brought exceptional properties and producibilities that, prior to its introduction, were a part of AM technology limitations.

The historical development of L-PBF and its capabilities in lattice structure manufacturing laid the foundation for the current research focus. The provided literature review discussed the mechanical properties of micro lattices, emphasizing the importance of unit cell geometry and design principles and their advantages, such as their lightweight nature and high-strength properties, which make them promising for applications in aerospace, biomedical, and structural components.

However, challenges mentioned in this chapter, including fabrication complexity, performance limitations, and material constraints, indicate the need for further investigations and provide insight into the ongoing research efforts, experimental methodologies, and the effects of various parameters on the mechanical behavior of micro lattices. This knowledge serves as a valuable reference for the current thesis, offering a platform for further investigation.

As the research progresses, the focus on control parameters in L-PBF for microlattices becomes crucial. Understanding the effects of machine, material, and lattice-specific parameters, as well as their interplay, is essential for achieving optimal printing outcomes. Recent case studies and experiments, accompanied by detailed analyses and comparisons, contributed to the growing knowledge of SS-316L porous micro lattices.

In summary, this chapter provides the foundation for the upcoming research chapters, guiding the optimization of SS-316L porous microlattices through L-PBF. This study is unique and pioneering due to the fact that most of the articles and literature that have previously been published in this field were mainly focused on the effect of different unit cell designs, arrangements of unit cells, and scanning strategies, and not many studies have paid attention to only investigating the effect of printing parameters on the mechanical properties of L-PBF-produced 316L porous lattice structures. However, these limited references make the progress of this work more difficult; on the other hand, the acquired results became more valuable, and that is exactly the forerunner force of this research.

2 | Methodology

As previously said, the primary objective of this research is to take a step toward the AM development path by optimizing printing parameters for L-PBF-produced stainless steel 316 porous lattices. This chapter specifies the utilized materials, sample preparation processes, and material characterization tests that were performed in the following sections.

2.1. Materials

2.1.1. Powder SS 316L

Stainless steel 316L powder with a particle size distribution (PSD) of 20 to 60 μm, was used for the production of the porous metallic lattice structures with different printing parameters to be studied in this thesis. The nominal composition of stainless steel 316L in wt.% was previously reported in Table 1.1 and the typical morphology of the 316L powder to be used in the L-PBF machine is indicated in Figure 2.1.

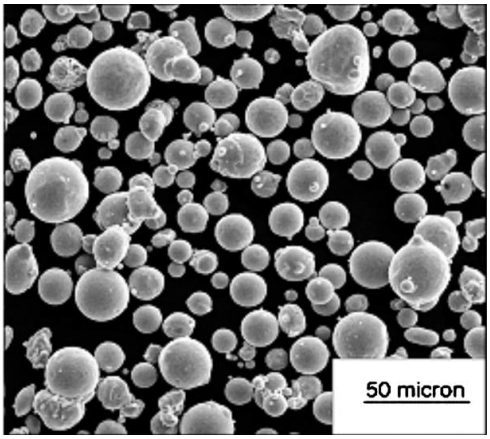

Figure 2.1: Typical Stainless Steel 316L powder used in L-PBF [52].

2.1.2. Microlattice Samples

As previously mentioned, this thesis has focused on the process parameter optimization for the L-PBF-produced stainless steel 316L porous metallic microlattice structures. For this purpose, as reported in Table 2.1, seven sets of SS 316L square cylinder microlattices with a 100 mm^2 cross section that is indicated in Figure 2.2 have been printed with three different scanning strategies and also in three different scanning speeds while the rest of process parameters were kept constant. The importance of these provided micro-size lattices is that they we manufactured without a CAD model and directly through the control of parameters like hatch angle, hatch spacing, and layer repetition which are not applicable on an industrial scale, and they became possible because Sharebot, as an AM machine manufacturer and supplier of studied samples, has the ability to produce samples with such alternating parameters

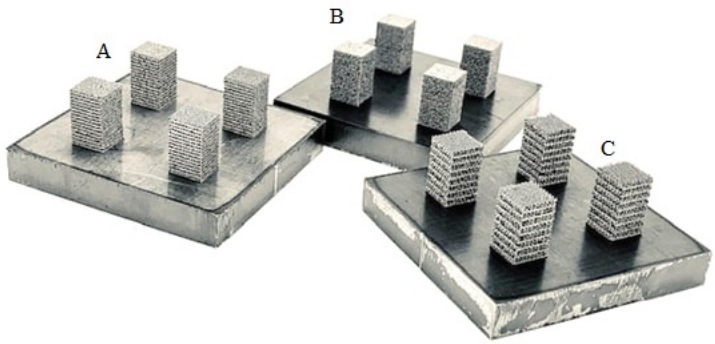

Figure 2.2: Printed Samples: (A) 10 Layers with 90° hatch angle, (B) 5 Layers with 90° hatch angle, (C) 10 Layers with 45° hatch angle,

Sample Set	**Layers (#)**	**Hatch Angle (Degree)**	**Scan Speed (µm/s)**
A1	10	90	600
A2	10	90	550
A3	10	90	500
B1	5	90	600
B2	5	90	550
B3	5	90	500
C1	10	45	600

Table 2.1: Sample Set Parameters

As mentioned microlattices have been produced and delivered by MetalOne L-PBF machine supplied by additive manufacturing machine producer company, Sharebot. Samples are delivered in seven batches and however, they are different in number of the layers, scanning speed, and hatch angle, the rest of the parameters are kept constant and can be mentioned as follows:

- Laser Power (p): 185W (60% of 285 which is the maximum power of the machine)
- Laser Scan (v): Continuous
- Focal Length: +2
- Spot Size: About 100 microns
- Layer Thickness (t): 0.05 mm
- Hatch Spacing(h): 400 μm
- Number of layers: 10, 5

As described previously, all the parameters were constant during the printing of all the sets in order to limit the variables and provide a perfect evaluation of the speed and scan strategy effects on the lattice mechanical properties.

Speaking of scanning strategy, the typical hatch spacing in the scanning strategy that was previously introduced (1.2.4) has been modified for this study to allow for the production of porous parts. These parts were created by selecting a hatch spacing equal to 400 μm so there was no overlap between the individual scan lines. In order to produce the desired lattice structure, the scan of each layer was repeated 5 or 10 times without any rotation. Figure 2.3a is a simple representation of the just-described scanning strategy, showing the distance between the adjacent lines and the number of layers that have been applied on top of each other. As can be seen in this representation, after printing a certain defined number of layers, a hatch angle of 90 degrees has been applied to generate the optimal property of controlled anisotropy. As can be seen in figure 2.3b and represented data from the provided lattices, the hatch angle has been set at 90 degrees for the first set of samples with 10 layer repetition, which is named series A, and for the other three sets of samples with 5 layer repetition, which are named series B. For further investigation, a 45-degree rotation has been implemented for sample set C, whose scanning strategy is similar to the previously mentioned porous metallic lattice structure with a 45-degree orientation (Fig. 1.29.b).

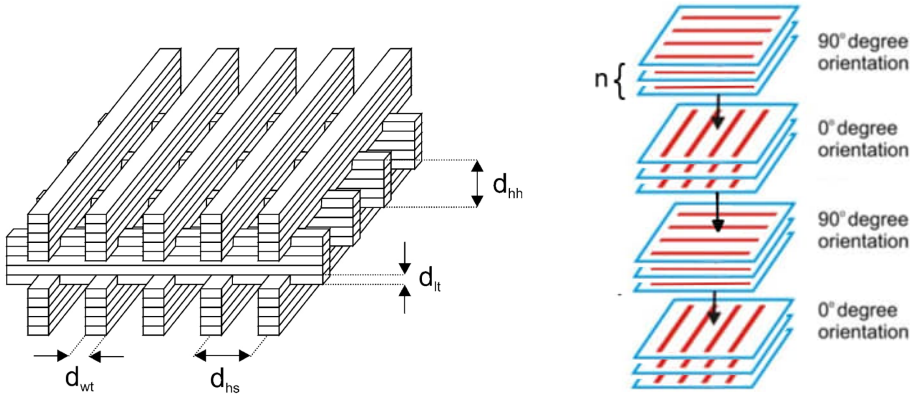

(a) (b)

Figure 2.3: The beam overlap design of porous structure (a), The 90 Degree layer orientations L-PBF laser scanning strategy (b) [10].

Speaking of scanning speed, samples have been printed with three scanning speeds with decreasing order of 600, 550, 500 μm/s for series A and B and Serie C only one set (C_1) with 600 μm/s scanning speed was printed. As mentioned in the given data and Table 2.1, the laser power for all the samples was kept constant during the process and the delivered energy was just adjusted through the change in scanning speed. Considering the fact that there is no overlap between scanning lines, between VED (1.1) and LED (1.2) the linear energy density formula is the optimal choice. Based on this equation, the delivered energy for sample sets A_1, B_1, and C_1 with 600 μm/s scanning speed, is approximately 308 [J/mm], for sample sets A_2 and B_2 with 550 μm/s scanning speed is 336 [J/mm], and for sample sets A_3 and B_3 with 500 μm/s scanning speed is 370 [J/mm].

2.2. Sample Preparation

2.2.1. Metallography

To gain a clear understanding of the effect of printing parameters on the microstructure of the printed samples and to identify the microstructure in the early-stage broken zones, three tested samples and one as-built from each set have gone through the metallography process and were prepared for further inspections.

Cutting

The samples were cut in two steps as the first stage in the metallography process. They were initially detached from the building substrate using a Hitech Europe Mod C250S

manual cutting machine, which is indicated in Figure 2.4a. Second, Metkon's Micracut 202 automated micro cutter was used to cut all samples, as shown in Figure 2.4b. The samples were sliced in half parallel to their building direction (Figure 2.4c), with the same cut setting used for all sets of samples. The cut began with a moderate rotating speed and gradually increased to 700 RPM. In the meantime, the machine's feed rate has been set at 20 μm/s and kept constant throughout the procedure.

(a) (b) (c)

Figure 2.4: The Cutting Device (a), The Microcutter (b).

Mounting

To proceed with the metallography process, due to the small size of the samples, the embedding was required to make possible the operation of later grinding and polishing steps. The cold mounting method was elected for this step in order to avoid lattice destruction through the applied pressure in the hot mounting machine. The other reason was the fact that due to the high pressure during the hot mounting, the mounting resins would penetrate the lattice and disrupt the grinding and inspection procedures in the late stage.

The samples were initially rounded with a thin layer of copper tape to meet the conductivity requirement during the surface inspection with scanning electron microscopy (SEM) and skip the extra gold coating procedure. Later, the cold mounting solution was made from a 2:1 combination of resin powder and hardener solution supplied by Hitech Europe and applied to the molds containing samples. The critical challenge for this step was keeping the back side of the sample uncovered because the water, polishing suspensions, and detached particles need to come out with the liquid flow during the grinding and polishing; otherwise, the particles would remain in the lattice and cause scratches in subsequent steps.

Grinding

By the end of the cold mounting process, a grinding process has been operated on the samples, beginning with 500-grit grinding paper and progressing through 600, 800, 1200, and 2500 papers in the following steps. The grinding process was done manually using the Mod MP311T manual grinding machine made by Hitech Europe, as indicated in Figure 2.5b. To minimize any heating influence on the microstructure, the grinding was done on wet grinding paper with flowing water. The operation began with a low rotation speed and gradually increased to avoid any deformation in the lattice structure.

It is important to note that an ultrasonic cleaning device was utilized to clean the sample and remove the grinded pieces in between the previously indicated stages. This step is critical for achieving a scratch-free surface by the end of the polishing process. Because of the small size of the pores, an ethanol solution has been chosen to provide better cleaning.

The main challenge in grinding the samples was the difference in the layers' thickness. As can be seen in Figure 2.3a, the utilized scanning strategy leads to the situation where only a very thin layer of the whole sample's surface is accessible in one plane. Because of this constraint, it was very simple to loosen the surface, which necessitated repeating the grinding until the next layer of horizontal rows was reached. This problem has been solved by regularly inspecting the surface after every five seconds of grinding to ensure the presence of a full surface in one plane.

(a) (b)

Figure 2.5: (a) Struers Automatic polishing machine (b) Paper Grinding Machine

Polishing

Following the grinding process, a polishing process has been applied to the as-built samples and the compressed samples with the same steps. The polishing has been done with the automatic polishing machine Struers Tegramin 25, which is shown in Figure 2.5a. The polishing process has been operated in three steps using MD Mol (3μm), MD-Plus (1μm), and MD Chem (Silica) polishing pads, respectively. For each step, its exclusive polishing solution has been applied by the polishing machine regularly, which was a 3 and 1μm diamond suspension supplied by Hitech Europe for the first two steps, and for the last step, a diluted OP-S NonDry solution, which was a colloidal silica solution supplied by Struer. The mentioned silica suspension has been diluted by distilled water in a 1:2 ratio. For a more controlled polishing process, the first two steps were initially applied by an automatic machine, and as a finishing step, they were polished manually for one minute before passing to the next step.

The lattice structure of the sample was the main challenge of the polishing step. Since the polishing pads were in cotton form, in some cases, part of the polishing pads became trapped in the lattice pores, fracturing the sample surface and scratching the polishing pad. A trial-and-error approach has been followed to face this challenge by adjusting the pressure applied to the sample by the machine's holder, the rotation speed of the polishing pad, and the increase in polishing suspension input. Based on the testing results, lowering the pressure to 25 N was adequate to avoid this difficulty. It should be noted that the fully flat and smooth surface of the sample after the grinding process, as well as the correct cleaning of the sample using the ultrasonic cleaner, was critical to preventing scratches on the sample surface and polishing pad.

Etching

As the final step in the metallography procedure, an etching solution prepared from a 1:1:1 combination of hydrochloric acid (HCL) 37%, nitric acid 65%, and water and has been used to erode the surface in order to see the microstructure of the objective zones and for further inspection.

The Main challenge in this stage was very different etching times for different structures and orientations. This problem has been addressed with a trial-and-error approach and multiple different etching times have been tested for each set of samples in order to provide a clear vision of the optimal etching time range for each structure. It is necessary to note that the over-etched samples have been grinded and polished again starting from the 2500 grinding paper.

The experimental times obtained from the tests revealed that larger lattices (Sets A and C with 10 layers) etch faster than smaller lattices (Set B with 5 layers) due to the lower density of material on certain surfaces, as the lattices with fewer layers have a higher density in certain areas and behave more like bulk samples. Meanwhile, the compressed samples from all sets exhibited nearly bulky behavior.

According to the experimental results, all compressed samples and samples from set B with 5 layers and a 90-degree hatch angle were etched in roughly 40 seconds, whereas sample series A with 10 layers and a 90-degree hatch angle took 13–15 seconds to etch. Samples from series C with 10 layers and a 45-degree hatch angle, on the other hand, were etched in almost 8 seconds.

2.3. Characterization Tests

As shown in Figure 2.2, each set of samples was printed on a single substrate with four separate lattice samples. A series of characterization tests on the samples, such as the compressive test, energy dispersive X-ray spectroscopy (EDS), scanning electron microscopy (SEM), digital image correlation (DIC), and optical microscope (OM), were performed to obtain complete data in order to provide a comprehensive vision of the effect of each parameter on the mechanical properties.

Each one of the four samples in all sets has been subjected to a similar process:

- One sample from each set has been analyzed as-built to characterize the original microstructure and any possible defect or geometrical heterogeneity coming from the manufacturing stage.
- One sample from each set has been compressed 70% of its initial height from the top surface along the building direction (Z axis) and analyzed.
- One sample from each set has been compressed 70% of its initial height from the lateral surface (X/Y axis) and analyzed.
- One sample from each set has been compressed 30% of its initial height from the top surface along the building direction (Z axis) and analyzed.

2.3.1. Energy Dispersive X-ray Spectroscopy (EDS) test

An energy dispersive X-ray spectroscopy (EDS) test was performed on the surface of an as-built sample to analyze the composition of the printed lattices, and the findings are provided in the next chapter (Table 3.1). The EDS test was carried out at Politecnico

di Milano University's materials analysis laboratory using the Zeiss EVO 50 scanning electron microscope (SEM), which is shown in Figure 2.6b.

2.3.2. Optical Microscope (OM)

An optical microscope inspection of the cut cross-section of the sample was undertaken in order to define exactly the influence of the printing speed and the number of layers in the microstructure of the provided samples.

The optical microscope examination was employed on every single sample of all seven sets of lattices in two steps. Each sample was examined with OM once at the end of the polishing process to characterize any surface flaws on the interior surface as well as offer a general picture of the lattice structure. After the etching procedure, the microstructure of each sample was investigated by OM once again, revealing the precise etched surface and identifying the microstructure of fracture zones, the quality of melting after rotation of the layer (effect of overlap strategy), and the quality of the attachment of the applied layer with the subsequent layer in order to decide on the optimal scanning speed.

The OM examination was carried out in the mechanical department of Politecnico di Milano University with the light microscope from the Zeiss company, as shown in Figure 2.6a, and the images from microstructure were taken with 25, 50, 100, 200, and 500 magnifications. All the acquired data are discussed further in the third chapter.

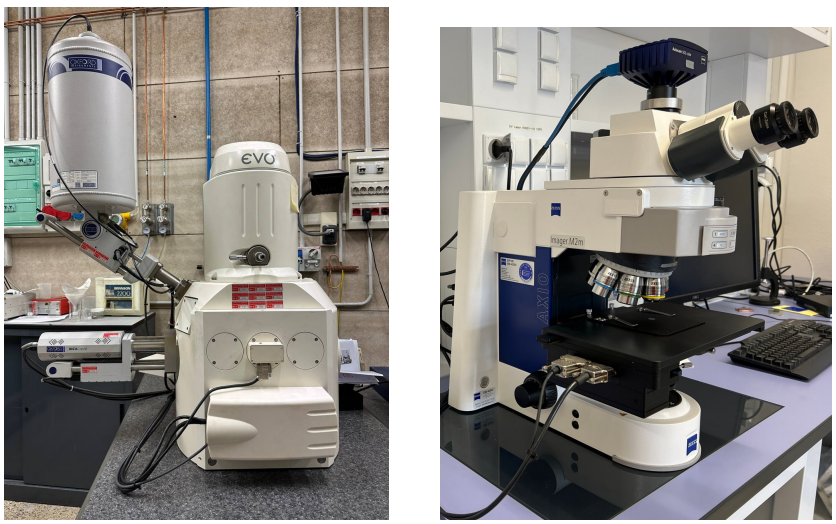

(a) (b)

Figure 2.6: (a) Scanning Electron Microscope (b) Optical Microscope.

2.3.3. Scanning Electron Microscope (SEM)

Fractography analyses and the analysis of printing quality for different scanning strategies were carried out by the Zeiss EVO 50 scanning electron microscope (SEM), which is shown in Figure 2.6b.

SEM examination was performed on one as-built sample from each series A, B, and C at all provided speeds from the top surface and lateral surface at 50, 150, 250, and 500 magnifications. In continuation, the remaining three samples from each batch were compressed before being subjected to the SEM analysis and then analyzed from the lateral surface. However, due to similarities seen in the as-built samples of each batch with different scanning speeds, only the three compressed samples from sets A1, B1, and C1 were chosen for further SEM analysis. All the acquired data are discussed further in the third chapter of the current thesis.

2.3.4. Compression Tests

Compression testing on microlattices is a fundamental method employed to assess their mechanical behavior and structural integrity under compressive loads. Microlattices, characterized by their intricate geometric designs, are subjected to axial compression to evaluate their response to compressive forces. The compression test provides insights into key mechanical properties, such as compressive strength, modulus of elasticity, and energy absorption capacity, essential for understanding the material's performance in various applications [56].

Compression tests in this study were performed with an MTS Alliance RF150 electromechanical testing machine that is shown in Figure 2.7a. For each set of samples, two samples have been compressed to 70% of their initial height, one in the Z direction and against the building direction, and the other into the lateral surface. The third compression test has been performed on the only remaining sample from each batch, which has been compressed to 30% of the initial height of the samples.

Concerning the compression test parameters that have been set on the test device, they are briefly mentioned as follows:

- Compression rate: 0.0833 mm/s (=5 mm/min).
- Data acquisition rate: 50 Hz.
- The process is done Without an extensometer due to the small size of the lattices.

The compressed samples have gone through the metallography process and fractography

analysis, as mentioned. The acquired data from compression tests has been processed, and the stress-strain graphs are presented in the third chapter.

(a) (b)

Figure 2.7: (a) Aramis Digital Image Correlation Camera. (b) Compressive Test Machine.

2.3.5. Digital Image Correlation (DIC)

Digital Image Correlation (DIC) is an optical non-contact measurement technique used to analyze and quantify the deformation, strain, and displacement of materials and structures. In DIC, a series of images captured during a deformation process are analyzed to track the movement of distinct surface patterns, called speckle patterns. By comparing the initial and deformed patterns, the software calculates displacement and strain fields, providing detailed insights into the material's mechanical behavior [58].

For a better understanding of the failure mode and fracture initiation points in the printed lattice structures, the final compression test, during which all the samples were compressed to 30% of their initial height, was recorded by Aramis 3D cameras from the GOM company, which can be seen in Figure 2.7b. The Aramis files were recorded by this equipment for the DIC analysis and processed by GOM Correlate 2020 software.

Based on the supplier's definition, "ARAMIS is a non-contact and material-independent measuring system based on digital image correlation (DIC). It offers a stable solution for full-field and point-based analyses of test objects of just a few millimeters up to structural components of several meters in size. In full resolution of 12 megapixels (5500 x 4400 pixels), up to 25 images per second can be recorded". The frames that are critical for having a clear vision of the failure mode of the lattice structures, that have been extracted from Aramis files, are presented and discussed further in the third chapter.

3 | Results and Discussions

Introduction

This chapter is dedicated to the presentation and analysis of the obtained data from the experiments described in the previous chapter. As previously stated, each of the four samples in each batch has undergone separate analyses to offer a full collection of data, resulting in a large number of images and graphs that need to be discussed. This chapter is divided into three main sections to provide a more organized sequence of data presentation and guarantee a better understanding.

1. As-built samples: This section contains results from EDS, OM, and SEM analyses done on the as-built samples' outer surface or inner cross-section.
2. Compressed samples: This section contains SEM and OM images of compressed samples and the corresponding stress-strain graphs for 70% compression tests along the Z axis or building direction and along the X/Y axis or lateral surface.
3. DIC Results: As the last section, this section is dedicated to the results of DIC tests as well as stress-strain graphs from the compression test with 30% compression from which DIC files were recorded.

3.1. As-Built Samples

In the following parts, the results of the as-built samples' analysis are presented. To have a better understanding, each series of samples is presented separately, which, in the meantime, is the study of the speed effect. Later, at the end of this section, the layer and hatch angle effects are discussed too.

3.1.1. EDS Results

The result of the energy dispersive X-ray spectroscopy (EDS) test is presented in the below-given Table 3.1. The table indicates the chemical composition of the printed sample, which, as can be seen in Figure 3.1, was done on the polished outer surface of the lattice.

Spectrum	Si	Cr	Mn	Fe	Ni	Mo	Total
Lattice Analysis 1	0.95	18.01	1.37	65.26	11.97	2.44	100.00
Lattice Analysis 2	0.65	17.86	1.48	64.91	12.40	2.70	100.00
Lattice Analysis 3	0.68	18.22	1.51	64.76	12.28	2.55	100.00
Average	0.76	18.03	1.45	64.97	12.22	2.56	100.00

Table 3.1: Weight % of the lattice EDS results.

It is important to mention that the carbon is not detected with sufficient accuracy in this test, and based on the previously given nominal composition of stainless steel 316L (Table 1.1), it is usually around 0.03 wt.% in 316L stainless steel. It is also important to consider the absence of the other light elements that were not detected in the EDS analysis.

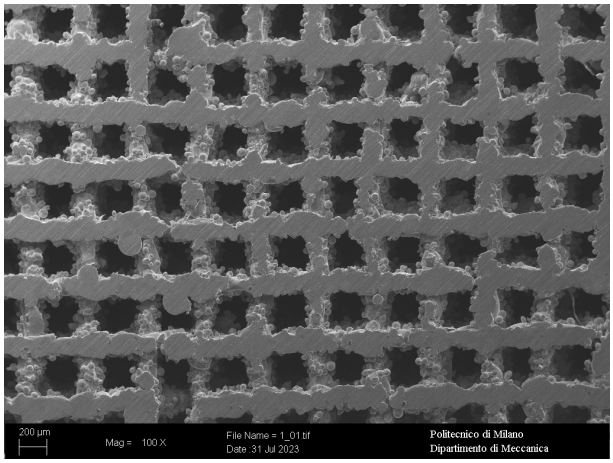

Figure 3.1: EDS Analyzed Surface

3.1.2. Scanning Speed Effect

As shown in Figure 3.2, a set of SEM images with x50 magnification from lateral and top views, as well as an OM image with x25 magnification from the cross-section of each series, is presented to provide a general introduction to each structure and the difference in their arrangements before beginning the detailed presentation of each series.

As is revealed, the major difference in the structure appears due to the different hatch angles. The sample with 45° rotation (C) looks different from samples with 90° rotation (A, B), which are more visible in the SEM pictures from the top view and OM pictures. As can be seen in the lateral view and cross-section, in series C, the line parallel to the picturing surface is repeated after four rotations; however, this happens after two

rotations in series A and B. On the other hand, the only difference between series A and B at this level of magnification can be mentioned as the smaller lattice pores and thus higher density in series B compared to series A due to their lower layer in each rotation.

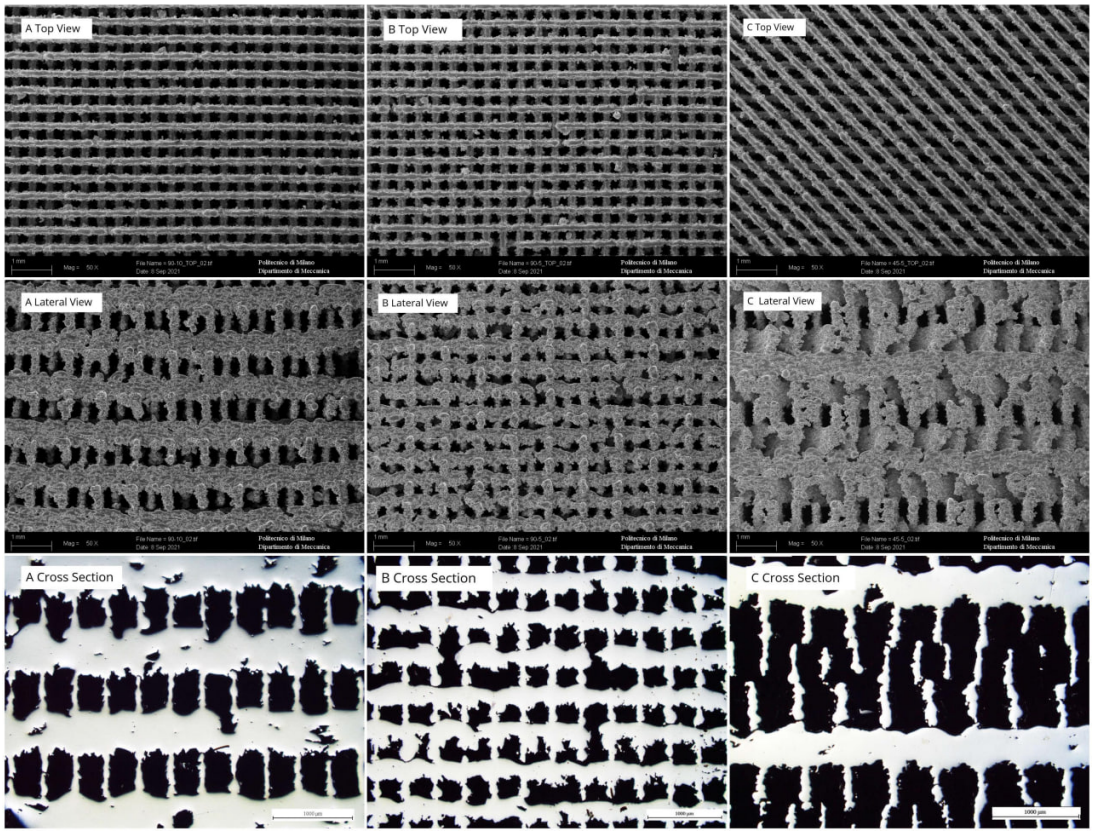

Figure 3.2: Asbuilt Samples: Cross-section: OM(x25), Top and Lateral Views: SEM(x50).

As can be seen in the lower magnification SEM pictures taken from the top view in Figure 3.2, the number of disorders and interrupted lines in the lattice structure is higher for the Serie B sample in comparison to series A and C. This finding is confirmed by the OM pictures taken from the etched cross-section of the samples, which are presented in the next sections.

The other important point to be highlighted is that, as can be seen in the provided OM pictures in Figure 3.2, the top border of each lattice pore reveals a rough surface compared to the bottom side of the pore. This rough surface appeared because the first layer of each set of hatches was printed on the powder substrate. However, the smooth layer at the bottom of each cell of the lattice was the last printed layer before rotation, which was applied to the previously printed solid substrate, resulting in better surface quality.

Because of this phenomenon and in order to have a uniform set of data, in this research, all

the samples have been prepared and analyzed, where the building direction of the sample is from bottom to top in all the acquired pictures, except for the samples compressed in the X/Y direction, where the building direction is from right to left.

Additionally, due to the importance of providing precise data and keeping the discussion focused simultaneously, more detailed pictures with high magnifications and graphs on a larger scale are presented in Appendix A and referred to regularly within the text.

Serie A, 10 Layers, 90° Rotation

Starting with the performed analysis on the Serie A samples, firstly, the SEM investigations were performed on the top and lateral surfaces of the lattice structure, which is shown in Figure 3.3. As visible in the lateral view (3.3a), there are a few porosities in between the layers of each set of hatches, as well as a lack of full attachment at several spots between the lines with different orientations, independent of scanning speed. It is also possible to identify interrupted scanning tracks that show the balling defect in top-view images (3.3b), which is probably related to the lack of fusion and inconsistency in the lower layers, or due to non-continuous laser scanning or excessive scanning speed. After considering the lateral view and seeing several inconsistencies in the lower layers, the first hypothesis is confirmed to have a higher probability.

Moreover, it is important to point out that SEM pictures indicate that decreasing the scanning speed from 600 μm/s in sample A_1 to 550 μm/s in sample A_2 and finally 500 μm/s in sample A_3, slightly reduces the number of balling defects in the structure of the lattice, as the theory behind this phenomenon is previously explained in Figure 1.23. This reduction in the scanning speed and, therefore, the increase in the delivered energy to the powder bed resulted in a reduction in the number of inconsistencies in the lower tracks.

Additionally, investigating the changes in the SEM pictures from sample A_1 to A_3 shows a small boost in the number of observable small metal balls connected to the main structure. As mentioned in the literature, this increase might be generated by the incomplete melting of the powders around the scanning track as a result of the increased supplied energy, which causes an increase in sputtering. As will be explained in the next paragraphs, OM results from these balls' microstructures (Fig. 3.4) confirm that these small balls are the unmelted powder particles that are fused and attached to the main structure, but the received heat was not enough to completely melt these particles.

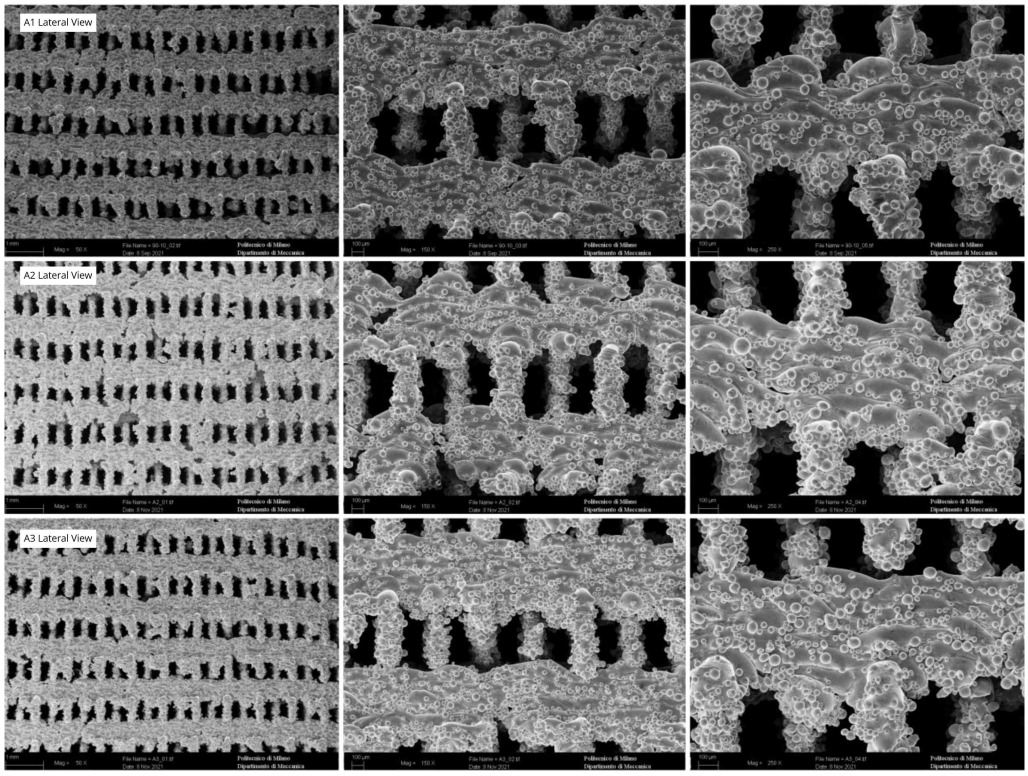

(a)

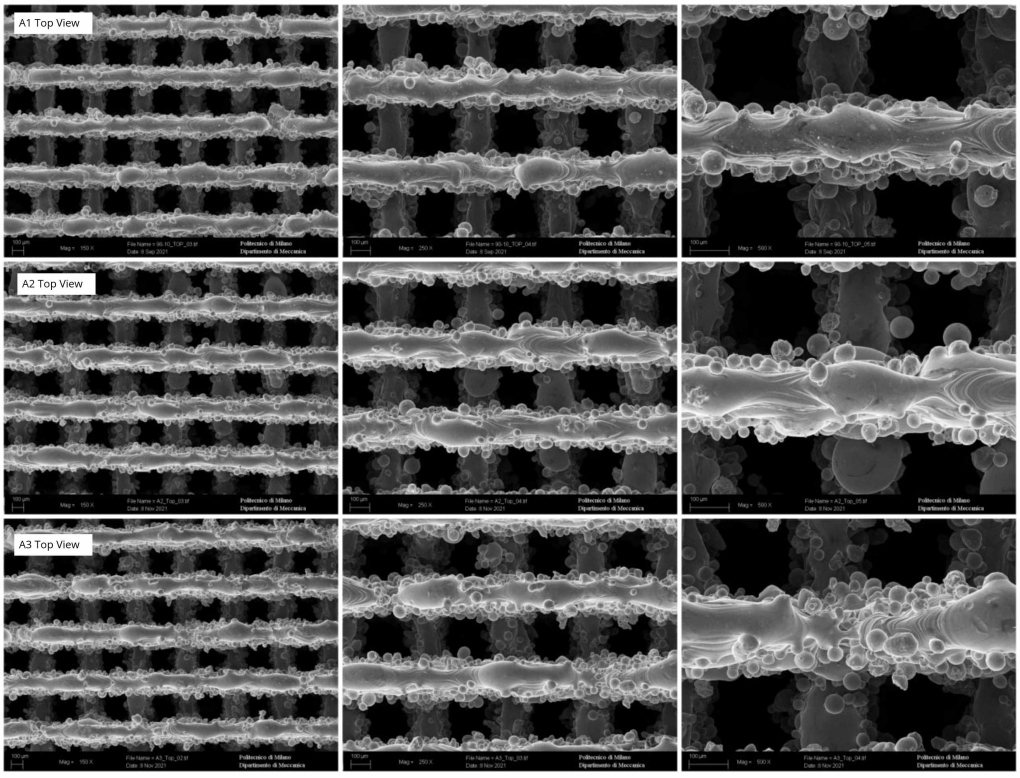

(b)

Figure 3.3: Serie A - Asbuilt SEM: A_1 (600 μm/s), A_2 (550 μm/s), A_3 (500 μm/s) (a) Lateral view, (b) Top view (Higher magnification A.2).

Following SEM, an OM examination was performed on the sample's inner surface, the results of which are shown in Figure 3.4. As can be seen, the first column is dedicated to the polished surface, which just exposes the sample's lattice structure and proves the presence of porosities. It is crucial to note that a few visible pores may be observed due to reaching the other end of the layer's width during the polishing step due to their thin width, which is noted in the methodology chapter as a major challenge in the polishing process. However, it is clear that the porosities similar to those captured in the images from sample A_3 in Figure 3.4 have been generated during the printing process.

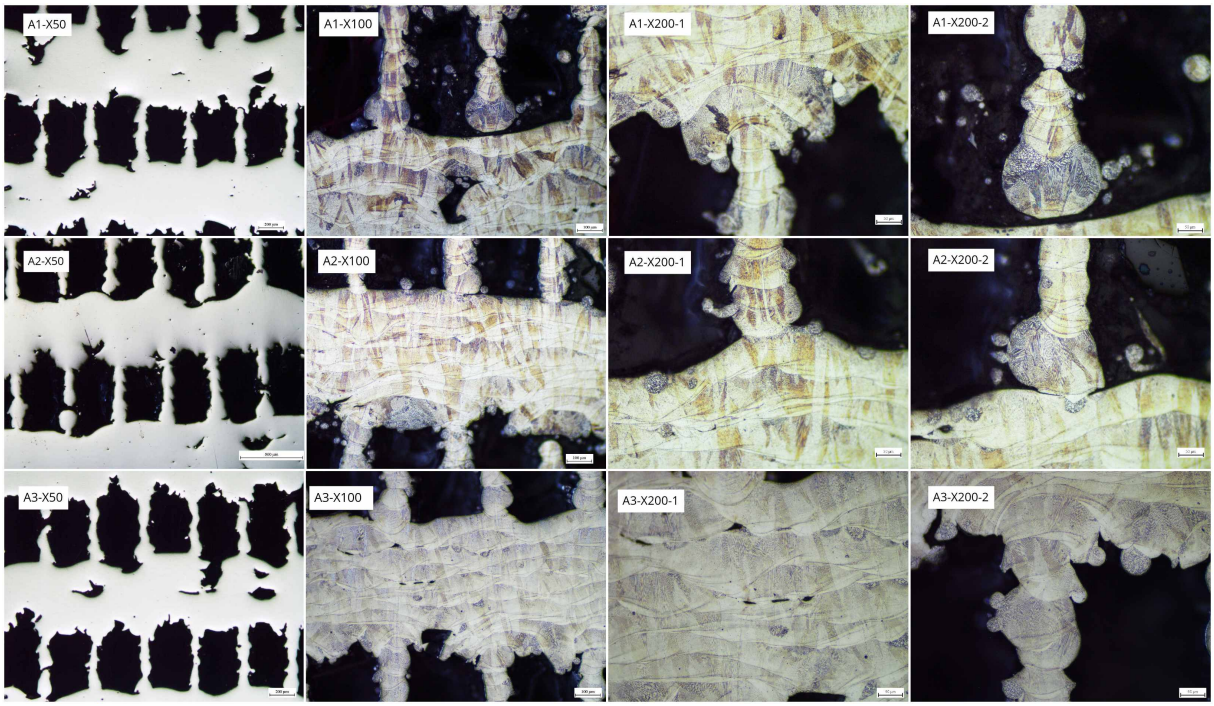

Figure 3.4: Serie A - Asbuilt microstructure: A_1 (600 μm/s), A_2 (550μm/s), A_3 (500μm/s)

Taking a close look at the above-presented pictures from the etched surface indicates that regardless of the scanning speed the presence of two types of microstructures can be identified in the micro lattice structure.

On the one hand, there is a perfectly melted structure that forms the desired layer-by-layer structure and shows a microstructure with grains that are elongated toward the building direction (Fig. 3.4.A_1,A_2 x200-1). On the other hand, a granular microstructure, which is identical to the microstructure of the unmelted powder particles that were previously introduced, mostly appeared at the top or bottom end of vertical lines where they were supposed to join the horizontal lines and remained incomplete (Fig. 3.4.A_1,A_2 x200-2).

It is important to mention that these two types of microstructure, are the two general

present microstructures in all the samples and series regardless of the scanning speed and the lattice structure. Accordingly, it is important to introduce each of these microstructures before proceeding to the SEM and OM results of series B and C.

Oriented Granular Microstructure: This microstructure reveals important information about the present sample. According to the literature, the grain orientation is influenced by the conditions during the solidification phase. In general, these grains grow from the cooler side to the warmer side, where in the applied L-PBF printing process, the upper surface is exposed to the laser beam while the bottom surface rests on a formed metal substrate that is relatively colder [17, 47]. As can be seen in high magnification photos of the etched cross-section of Serie A samples in Figure 3.5, it is possible to distinguish elongated grains from the bottom to the top of each layer.

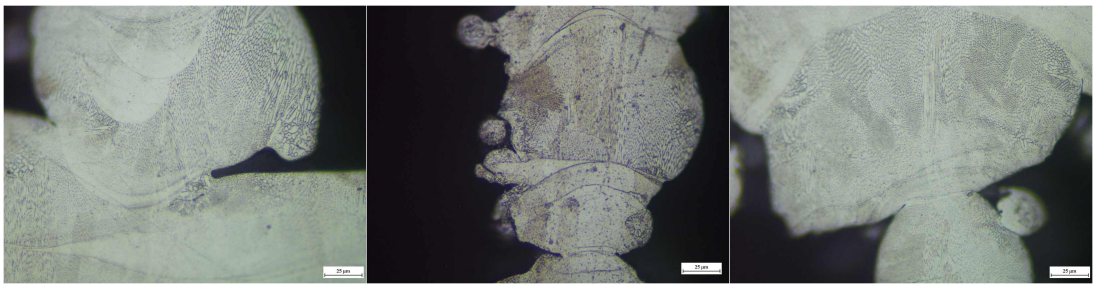

Figure 3.5: Serie A samples microstructure, x500 magnification OM pictures

As demonstrated in Figure 3.6, the elongated grains are aligned in the direction of the temperature gradient. This directional solidification produces coherently oriented grains along the building direction and influences mechanical characteristics dependent on the test direction and grain orientation [17]. Another point that can be seen in the high-magnification images is that the melting lines at the bottom of the melting pool are parallel to the L-PBF construction platform, whereas the top surface of the melting pool has been affected by the application of subsequent layers that have a melting pool with a depth greater than the layer thickness, as shown in Figure 3.5. This setting caused a remelt in the lower layers and formed better bonding between the layers.

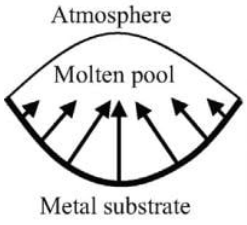

Figure 3.6: Diagram of the solidification of the melted pool during L-PBF process [17].

Powder Shape Granular Microstructure: As previously mentioned, this microstructure, in most cases, is the shared microstructure between the disjoint points of layers from two different hatches at the top or bottom end of the vertical lines, the small balls attached to the main structure, and a few interruptions in the tracks identified as a balling defect.

It is important to quote from the literature that during processing, a significant percentage of the first scanned layer of each hatch set is melted over free powder rather than previously melted solid. Scanning on free powder as opposed to previously melted solid has been shown to create an increased proportion of sintered rather than melted material [10]. Based on this explanation, this microstructure is identified as the original powder particles that have been generated due to an amount of heat that was enough to fuse and bond the powder particles together but not enough to melt the powder and the lower layer to form the melt pool and the perfectly melted microstructure that was discussed before. The theory confirms that the heat applied to the powder dissipated due to the distance between the heated powder and the lower melted layer and thus the lack of interference between the two phases, which led to the heat sink and dissipation. A more detailed picture is also presented in the later section (Fig. 3.9).

These microstructures are repeated in all the samples and play a crucial role in the compressive behavior of the lattices, which is discussed later. In the next sections, these microstructures are only referred to as "melted microstructure" and "unmelted microstructure" in order to be focused and avoid excessive explanations.

To summarize, the decrease in scanning speed in Serie A samples did not affect the microstructure of the lattice; however, aside from increasing the small unmelted balls, it resulted in a very slight reduction in porosities between subsequent layers of one hatch and reduced the balling defect by increasing coherency in lower layers.

Serie B, 5 Layers, 90° Rotation

Continuing with the performed analysis on the Serie B samples, the result of SEM inspection on the top and lateral planes of the lattice structure is presented in Figure 3.7. As can be seen, regardless of the scanning speed, the introduced balling defect can be identified in tracks in both top and lateral view pictures (similar to Serie A samples).

Moreover, focusing on SEM lateral pictures (Fig. 3.7a), there is no notable difference between the samples with different scanning speeds, and all Serie B analyzed samples showed quite similar balling defects, discontinuities in tracks, and incomplete attachment of the vertical and horizontal tracks in the SEM pictures.

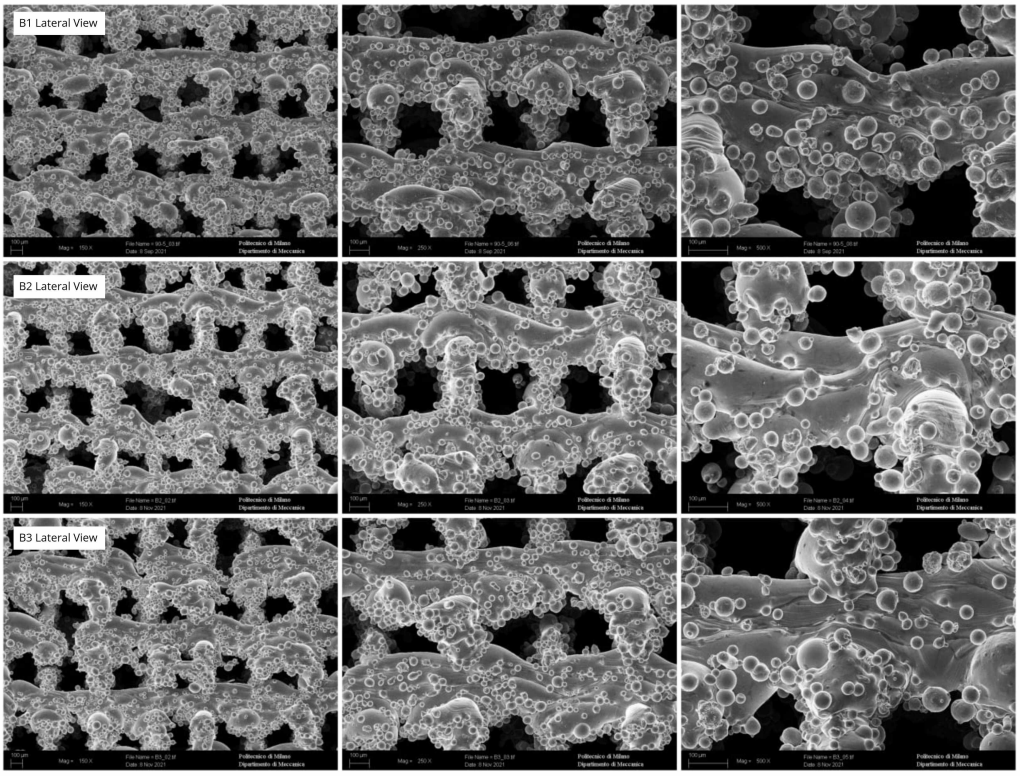

(a)

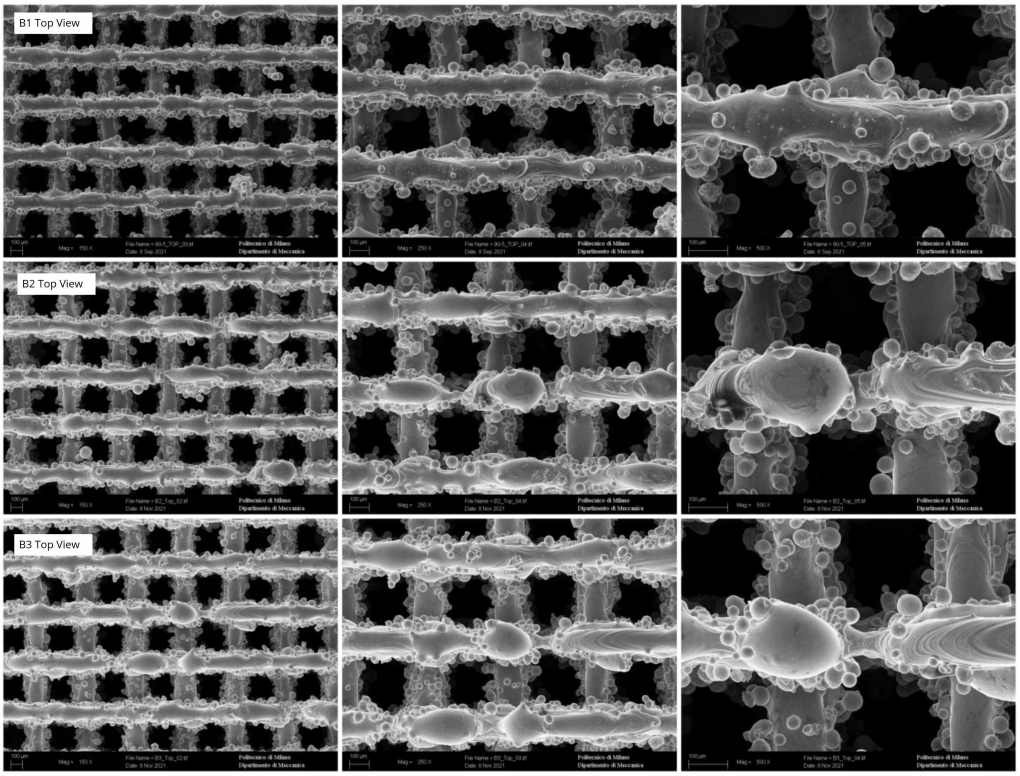

(b)

Figure 3.7: Serie B - Asbuilt SEM: top to bottom B_1 (600 μm/s), B_2 (550μm/s), B_3 (500μm/s) (a) Lateral view, (b) Top view (Higher magnification A.3).

On the other hand, investigation of the optical microscope results from the different scanning speeds which are shown in Figure 3.8, reveals a few distinct differences between samples B_1 with 600 μm/s, B_2 with 550μm/s, and B_3 with 500μm/s scanning speed. As observed in the image, despite the existence of ball-shaped endpoints at the top and bottom ends of vertical lines with their unmelted microstructure, the number of these types of endings showed a slight reduction by lowering the scanning speed. Furthermore, through considering the low magnification OM pictures, the overall regularity of the lattice structure in sample B_3 is greater than in samples B_2 and B_1 respectively.

The previously discussed heat dissipation due to the lack of attachment between heated powder and the lower surface can be clearly observed in the high magnification OM pictures in the below given Figure 3.8.B_1,B_3-x200.

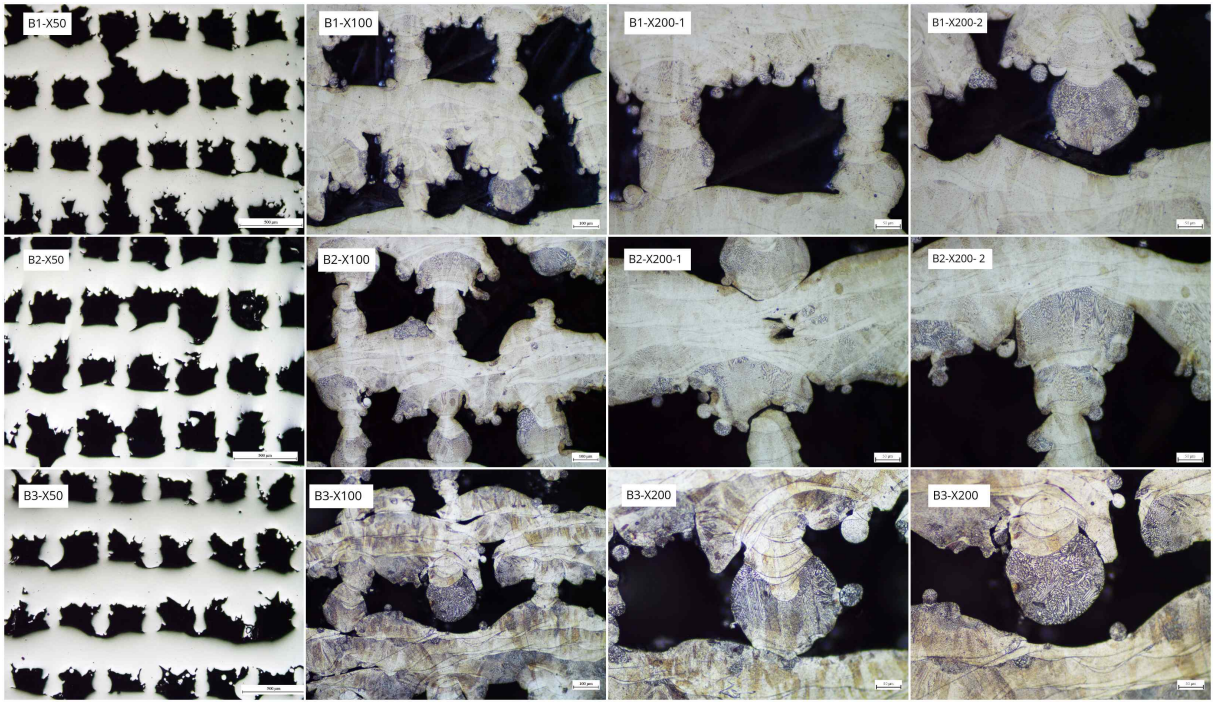

Figure 3.8: Serie B - Asbuilt Microstructure: B_1 (600 μm/s), B_2 (550μm/s), B_3 (500μm/s)

To have a more detailed look, Figure 3.9 indicates the high magnification of the Serie B samples containing both previously defined microstructures. As can be seen, Figure 3.9.1 shows the elongated grains along the building direction and also the perfect layer-by-layer structure of the vertical line. While, other pictures show the unmelted powder microstructure, that despite the incomplete melt, their grains at some spots are aligned in the building direction too. Moreover, Figure 3.9.3 clearly shows the penetration of the melting pool to the lower layer and the fact that the proper level of melting can turn the unmelted granular microstructure into a perfectly melted one.

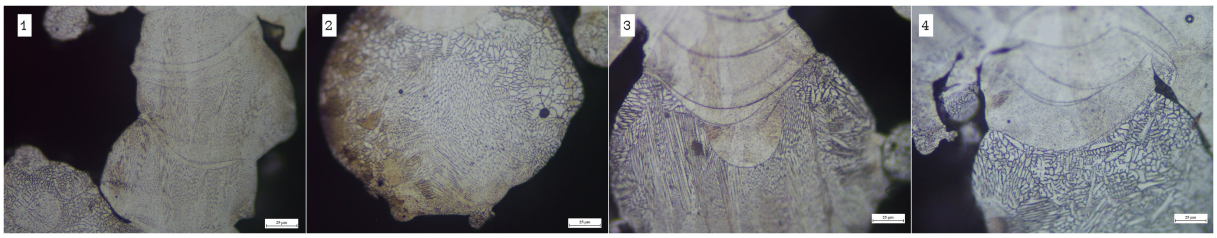

Figure 3.9: Serie B samples microstructure, x500 magnification OM pictures

To sum up, the decrease in scanning speed in Serie B samples did not significantly affect the number of columns with unmelted microstructure or the level of porosity; however, lower speeds generated a slightly more disciplined arrangement of microlattice structure.

Serie C, 10 Layers, 45° Rotation

Finishing the study of as-built samples with the results of SEM and OM analysis on sample C_1 with 600 μm/s scanning speed from the Serie C batch. Given the SEM results from the lateral and top views of the sample's outer surface in Figure 3.10, it only provides a general vision of the structure in low magnification pictures and proves the presence of pores between the layers one hatch in high magnification pictures. Additionally, the disjoints in the connecting points of different hatches can be observed.

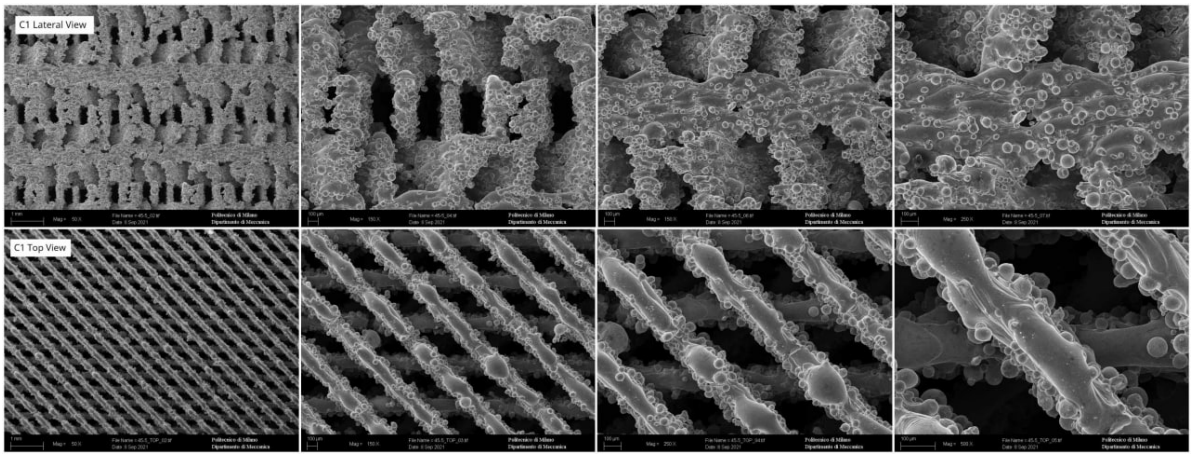

Figure 3.10: Serie C as-build sample C_1 (600 μm/s).

A detailed examination of the optical microscope images of sample C_1 verifies the presence of both sorts of specified microstructures in this sample as well. Furthermore, high-magnification OM images presented in Figure 3.11 indicate that the attachments of vertical lines that represent layers with 45°, 90°, and 135° rotations are weak, and most of the joints between these layers are either not connected or subjected to the granular un-

melted structure and have less mechanical strength than the joint point between 0° and 180° rotation layers (parallel to the picturing surface) and their subsequent layers.

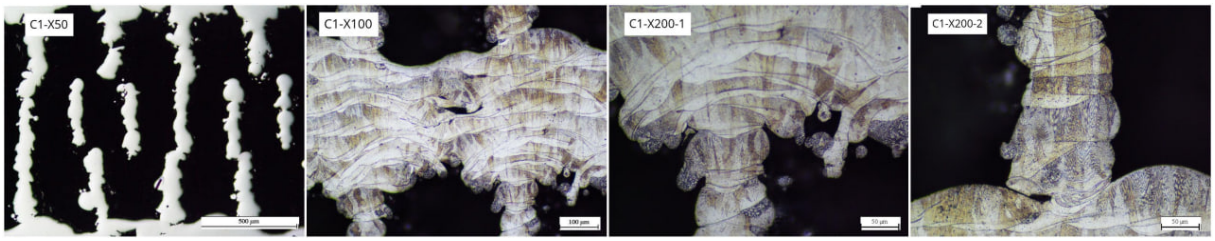

Figure 3.11: Serie C - Asbuilt Microstructure: C_1 (600 μm/s).

3.1.3. Layer Effect

In this section, the effect of the number of layers in each rotation is discussed through the comparison of the SEM and OM results of the samples from series A and B with 10 and 5 layers repeated in each hatch, respectively. It is worth mentioning that only SEM and OM analysis on the as-built samples is not enough to identify the effect of one parameter, and the discussed points will be supported by considering later compression test results.

In order to stay focused, only A_1 and B_1 samples with 600 μm/s scanning speed are compared in this section, while the comparison of all the scanning speeds from both series A and B in higher magnifications is reflected in appendix A.4.

A brief look at the SEM and OM images of both samples at low magnification reveals that the five-layer structures (B) provided smaller lattice cells than the ten-layer structures (A). Focusing on the SEM images shown in Figure 3.12 proves that Serie B samples have a higher number of lattice disorders such as balling defects visible in the top view pictures. Meanwhile, SEM pictures from the lateral view show that the vertical lines (the layers with 90° hatch) are formed out of the lattice structure in sample B_1 compared to A_1. Considering the OM result presented in Figure 3.13, these popped-out lines are spherical in shape and have the mentioned unmelted powder granular structure.

A more focused investigation of OM images of both samples confirms that the number of these spherical endpoints located on the top or bottom of the vertical lines and the joint spots of the lines after rotation are higher in sample B_1 in comparison to A_1. Furthermore, the OM results in Figure 3.13 reveal that sample A has longer columns (10 layers) and its cells are more organized than the cells in sample B, which could be due to the detrimental effects of the laser beam on neighboring lines because of the small cell size in sample B.

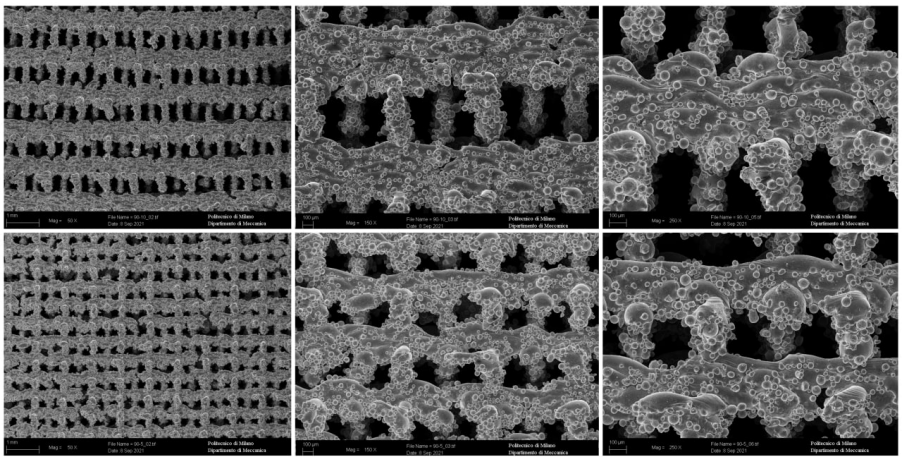

(a)

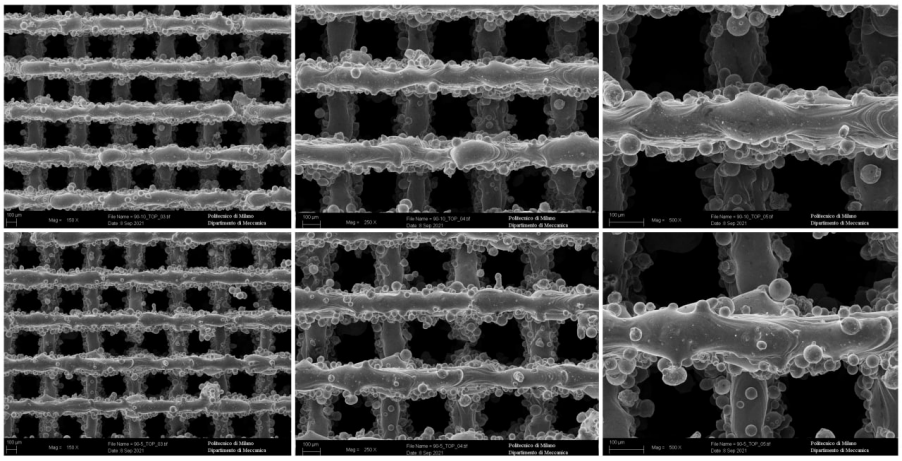

(b)

Figure 3.12: Layer Effect SEM $A_1 - B_1$ (600 μm/s):(a) Lateral view (b) Top view, (Different presentation A.4)

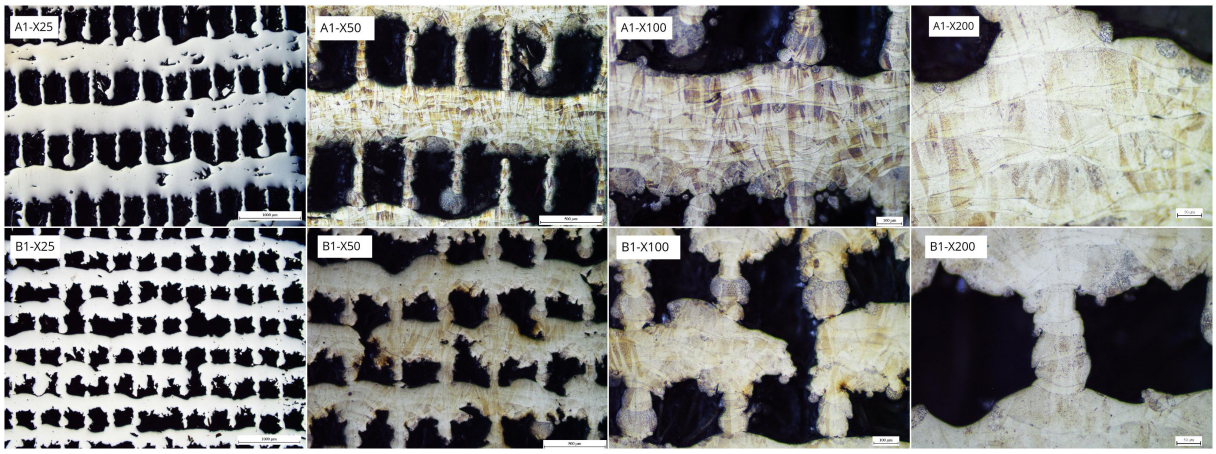

Figure 3.13: Layer Effect OM $A_1 - B_1$ (600 μm/s)

3.1.4. Hatch Angle Effect

The study of the hatch angle effect on the structure and microstructure of the presented microlattices is performed through the comparison of A_1 and C_1 samples' SEM and OM results.

As can be seen in Figure 3.14, SEM pictures at this stage only show the difference in the structure of the samples, and further data needs more investigation.

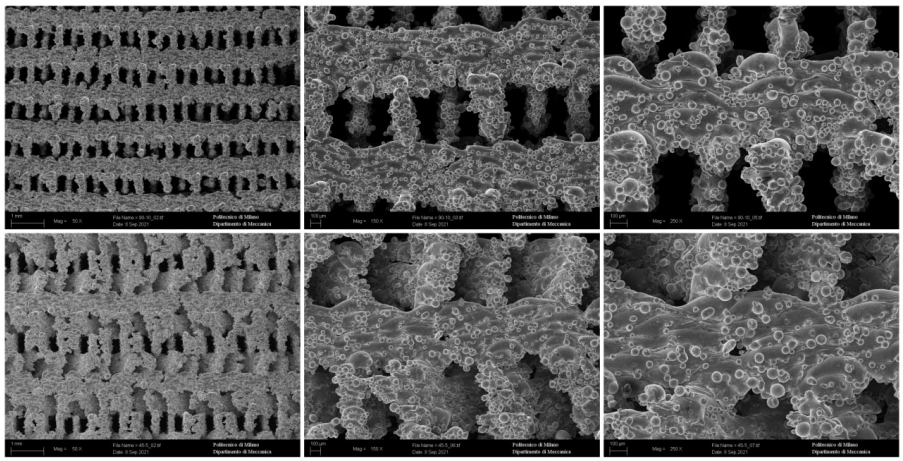

(a)

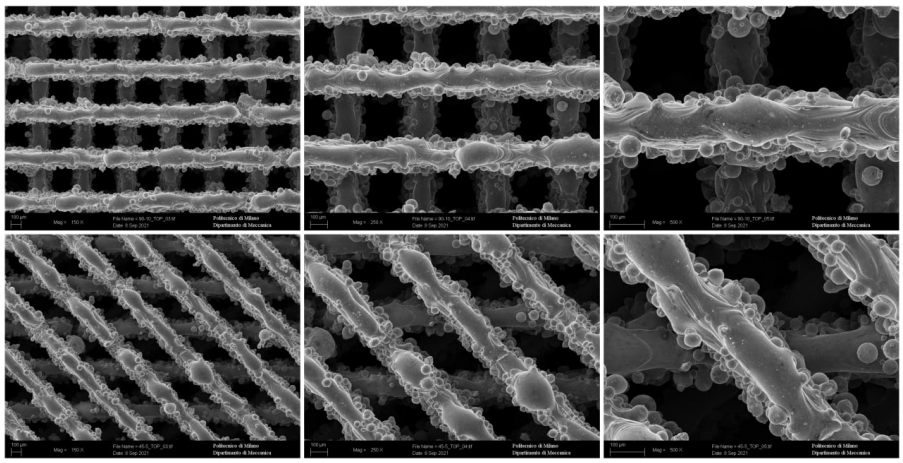

(b)

Figure 3.14: Hatch Angle effect- Sets A_1 (90°) on top and C_1 (45°)- 600 μm/s scanning speed (a) Lateral view, (b) Top view (High Magnification A.1).

However, by comparing the acquired OM results in Figure 3.15, it is possible to mention that sample A_1 is more organized in terms of cell arrangement, and this sample has a higher number of joint points between layers of different hatches (vertical and horizontal lines) with melted microstructure and a higher attached crosssection compared to sample

C_1, where most of the layers from different hatches are either not connected or contain the unmelted powder granular structure.

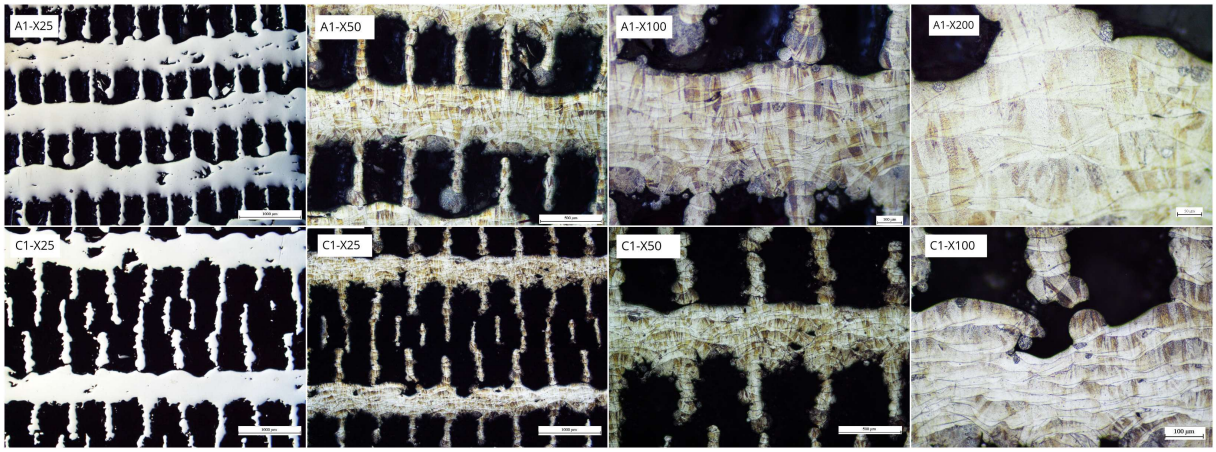

Figure 3.15: Hatch Angle Effect OM $A_1 - C_1$ (600 μm/s)

3.2. Compressed Samples

As previously mentioned, three levels of compression tests were applied to three samples from each set, and the acquired results are presented in the following sections. As can be seen in Figure 3.16 indicating the SEM pictures from the compressed samples, each of the designed structures, A, B, and C, had distinct deformation behavior in response to the operated compression tests.

Based on the presented OM results in the previous section, it was visible that there are no significant microstructural differences between samples from the same set but with different scanning speeds (Figures 3.4, 3.8). Based on this experimental data, only samples with a scanning speed of 600 μm/s from each batch have been selected to be studied through the SEM and OM analyses. However, due to the exclusive compressive behavior and stress-strain values that appeared in the compression test results, the stress-strain graphs have been extracted and presented for all the samples, and together with the DIC data, they are addressed in the next sections.

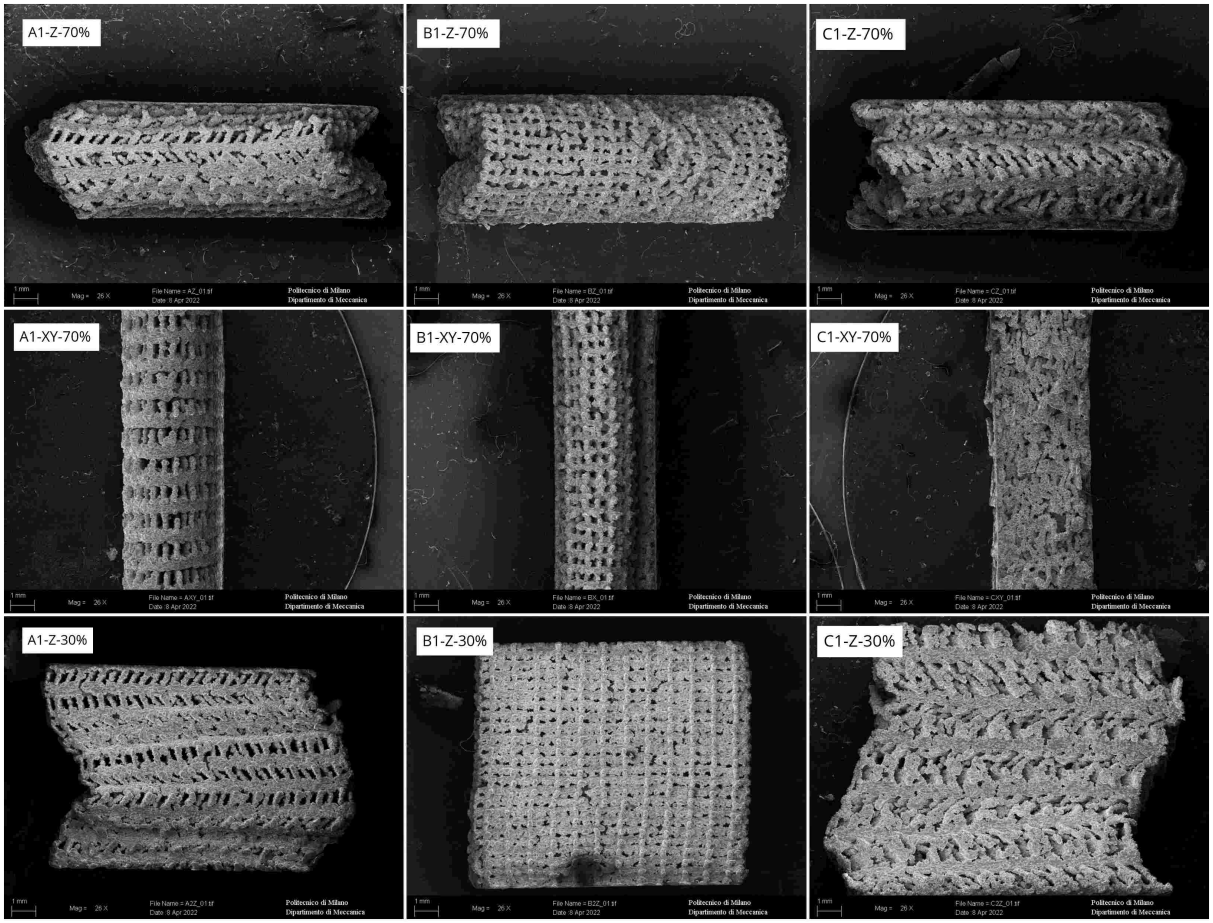

Figure 3.16: Compressed samples' SEM pictures

To provide a disciplined presentation of data, similar to the previous part, the collected findings are divided into three groups based on only one variable parameter, and the SEM, OM, and stress-strain graphs have been analyzed with regard to that parameter in each category. The three groups are as follows:

1. Scanning Speed Effect
2. Layer Number Effect
3. Hatch Angle Effect

3.2.1. Scanning Speed Effect

Due to the choice of one scanning speed from each set to be analyzed through SEM and OM inspections, the only feasible data to study the compressed samples from the scanning speed aspect is the stress-strain curves.

Figure 3.17 represents the results of the two modes of compression tests done on the Serie A samples, one along the Z axis or building direction of the microlattice and the other along the X/Y direction or lateral surface of the microlattice. As can be seen, Figure 3.17a indicates the stress-strain graphs of each scanning speed in Serie A samples in both directions. Apart from the importance of the total stress along the 70% strain, a better understanding of the yielding procedure in each sample is critical for having a reliable conclusion from the results. For this purpose, a section of each graph that contains the yielding area and belongs to the first 30% of the strain is zoomed in and presented in Figure 3.17b. Similarly, Figure 3.18a represents the stress-strain graphs that show the details of the compression test operated on the Serie B samples in both Z and X/Y directions, and Figure 3.18b indicates the yield behavior of each scanning speed on B samples separately but on the same scale.

Taking a close look at the presented data both indicated graphs for Series A and B reveal a considerable increase in both initial yielding values and the maximum achieved stress values by reducing the scanning speed. On the other hand, considering the compressive behavior of Serie A samples, Figure 3.17 represents a bending-dominated lattice structure in compression behavior with several drops followed by spikes in the stress level in compression along the Z axis, which is related to the failure of the layers of the lattice. After a few fluctuations in the stress level related to the failure of subsequent layers, the compaction of the lattice starts, which is shown by the continuous increase in the stress level for strains higher than 50%. It is worth highlighting that the given stress-strain graphs exactly follow the previously introduced stress-strain graph (Fig.1.30) showing

the schematic compression stress-strain curves of a bending-dominated and a stretch-dominated lattice structure. In the following section, the stretch-dominated behavior of Serie B samples is discussed.

Based on the experimental data, strain values higher than 70% show a huge spike in stress values, which is related to reaching the relatively bulky structure.

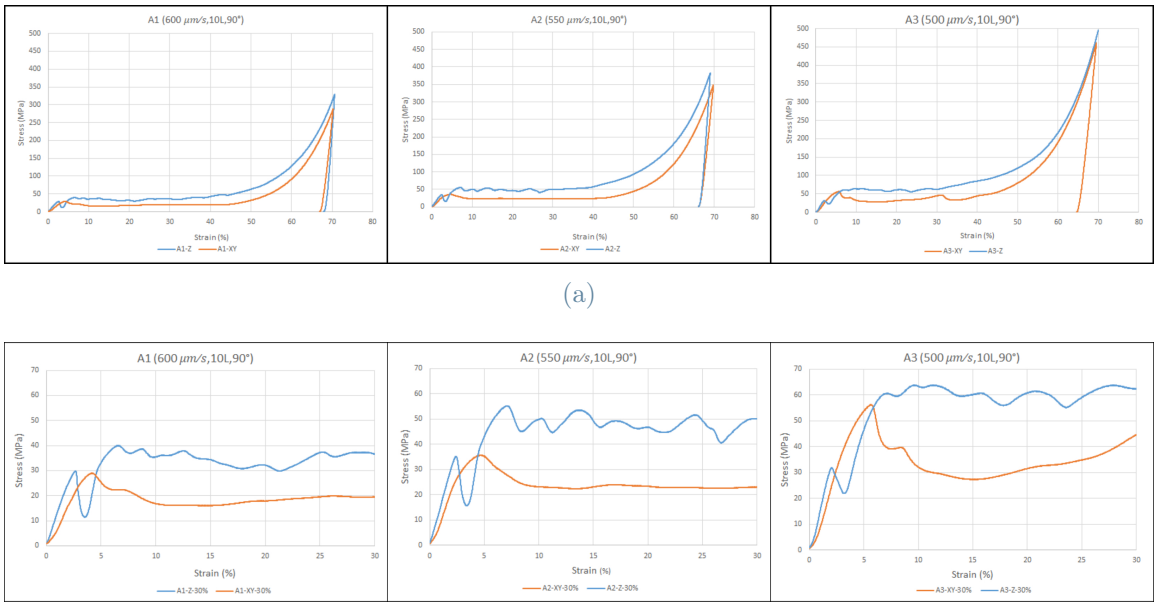

(a)

(b)

Figure 3.17: Compressed samples, Speed effect, A1, A2, A3 Compression 70% along Z axis and X/Y axis. The large-scale graphs are presented in Appendix A.5.

Considering the compression behavior of the series B samples represented in Figure 3.18, due to the absence of any failure between the layers, a stretch-dominated compression behavior is identified in the compression test of Serie B samples along the Z axis direction, and no fluctuation in the stress values is visible. This resistance to early failure in samples with five-layer repetition can be confirmed through the DIC results and the pictures taken from the compressed samples. On the other hand, as can be seen in Figure 3.18b, Serie B samples represent a bending-dominated behavior in the compression test along the X/Y direction, and the difference between two graphs is identical to the previously introduced schematic difference of two present compression behaviors in Figure 1.30.

It is important to mention that, unlike the Z axis where the Serie B sample showed a stretch-dominated compression, in the compression test along the X/Y axis, both the A and B series show similar bending-dominated compressive behavior and represent a single slight drop followed by a continuous growth in the stress values. However, it is necessary

to highlight that this decrease in Series A samples is higher than in Series B.

To be highlighted from the graphs, the yielding stresses and maximum achieved stresses in the X/Y axis compressions are mostly equal or lower than related values in the compressions along the Z axis. Based on this experimental data, to avoid any confusion due to the high number of overlapping graphs, the presentation of the values for the X/Y compression tests is avoided in the next sections. However, the comparison of X/Y compression tests based on the varying parameters is presented in the appendix A.

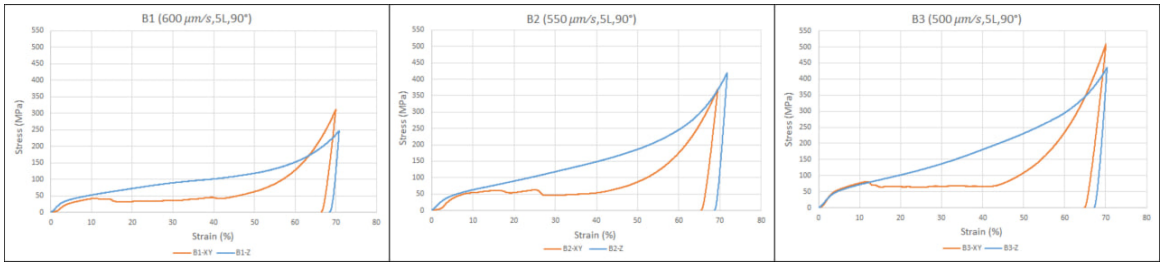

(a)

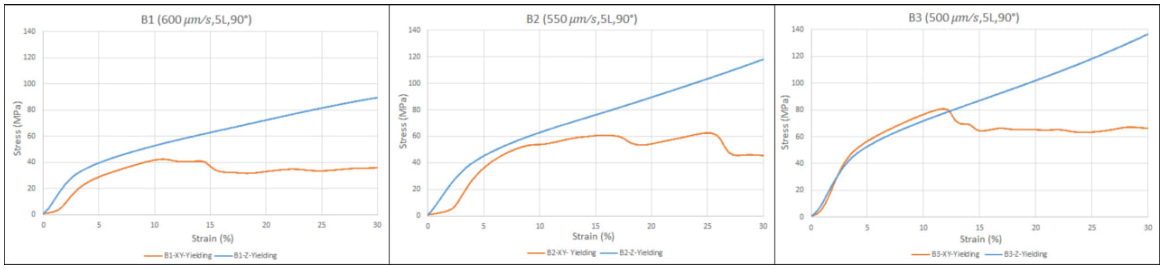

(b)

Figure 3.18: Speed effect on B1, B2, B3 Compressed samples, Compression 70% along Z and X/Y axis. The large-scale graphs are presented in Appendix A.6.

3.2.2. Layer Number Effect

For studying the effect of the number of layers, the SEM and OM investigations have been selectively applied to the compressed sample A_1 and sample B_1 both with 600 μm/s scanning speeds and 10 and 5 layers repetition respectively.

As can be seen in Figure 3.19, the SEM pictures from the three compressed samples from each mentioned batch are indicated which show the compressed samples with 70% compression along the Z axis (Fig.3.19a), 70% compression along the X/Y axis (Fig.3.19b), and 30% compression again along the Z axis (Fig.3.19c).

Before the start of the discussion, it is important to mention that during the investigation of the samples, first the 70% compression test was applied to the samples, and the results

were studied through the SEM and OM, which indicated the total failure of the structure in all the samples. This finding led the study to the third compression test to be done in 30% of the samples' initial height to understand the failure behavior of samples.

Firstly, the important point to highlight about the SEM results of the compressed A_1 and B_1 samples along the X/Y direction is the fact that layers printed on top of each other from the same hatch have high compressive strength as one unique section. As can be seen in Figure 3.19b, the parts with 10 repeated layers are bent 180° without any observable break in their structure; however, the joint points of the layers with distinct hatches are detached from each other. However, the sample B_1 showed a fracture in the mentioned area which is related to the small lattice dimension and thus less ability to bend otherwise the microstructure of both samples is the same.

Considering the SEM pictures at low magnifications, the deformation in the lattice structure of sample B_1 is less in comparison to sample A_1 in the 30% compression in the Z direction. As we can see in the SEM pictures clearly, sample A_1 shows sliding of the layers in Figure 3.19c; however, sample B_1 has just a slight bending and experiences buckling instead of sliding which can be clearly seen in Figure 3.20c.B_1 x50 and x200-1 where the horizontal layers reached to each other but the columns in between did not fail or bend. This is highly related to the short columns in sample B_1 which only get more compact under compression force and do not bend or fail as easily as the columns in sample A_1.

The mentioned short columns and more compact structure with smaller lattice cells in sample B_1 caused the distribution of the applied compressive load all over the structure and led to the generation of a large number of cracks in the joint points instead of the bending and failure of the columns, which can be confirmed through considering the OM pictures of compressed samples presented in Figure 3.20. These cracks are more visible in the OM pictures of sample B_1 compared to A_1 (Fig.3.20c) due to the fact that sample A_1 experienced a stress relief step through the failure of its layers which can be identified in the stress-strain graphs shown in Figure 3.21b.

As is clear from the OM and SEM pictures of both series regardless of the number of the layers, there are hardly broken sections within the layers from the same hatch and most of the broken parts in both series are detected at the joint point between the layers from different hatches. This finding is confirmed through the OM results presented in Figure 3.20, where the endpoints of the columns show the most disconnections and broken parts when they contain the previously introduced unmelted microstructure.

Through the high magnification OM pictures presented in Figure 3.20, it is possible to confirm that in the presence of a **perfectly melted microstructure** at the joint points

of layers with different hatches, the structure remains without any cracks or fractures even in compressions up to 70% of the initial height of the sample. This fact can be clearly seen in Figures 3.20a A_1 x200-2, B_1 x200-1, and Figure 3.20c A_1 x200-1.

In the meantime, through the high magnification OM pictures presented in Figure 3.20, it is possible to confirm that the **granular unmelted microstructures** are the most talented areas to break and fail even in small strains. Most of these areas are either not attached to the earlier or subsequent layers or failed and broke in low stresses (Fig.3.20c). This fact can be clearly seen in Figures 3.20a A_1 x200-1, B_1 x200-2, Figures 3.20b A_1 x200-1, B_1 x200, and in a more obvious view in Figures 3.20c A_1 x200-2, and B_1 x200.

To sum up, from the microstructural investigations for the layer effect and the OM results of the broken parts, it can be concluded that in Serie B samples with five layers of repetition, there is no failure of the layers; however, in Serie A samples with ten layers of repetition, failure occurs in low stress. To be more precise, comparison of the schematic compression stress-strain curves from Figure 1.30 with the experimental results presented in Figure 3.17,3.18 revealed that the Serie A samples with ten layers of repetition lattice structure showed bending-dominated behavior with lower yield strength, a stress plateau, and therefore, a lower compressive strength compared to the Serie B sample with five layers of repetition lattice structure, which showed a stretch-dominated behavior.

It is important to highlight that the crack initiation in all samples is identified to start from joint points between layers with different hatches that have the mentioned incomplete fused powder, previously called unmelted granular microstructure. In some pictures, it is visible that these areas are the crack initiation points, which then extended to the main structure and caused the total failure of that layer and thus the final collapse in the lattice, which only occurred in Series A and C samples. These slidings and the sequence of failure of the individual layers can be correlated to the stress-strain graphs.

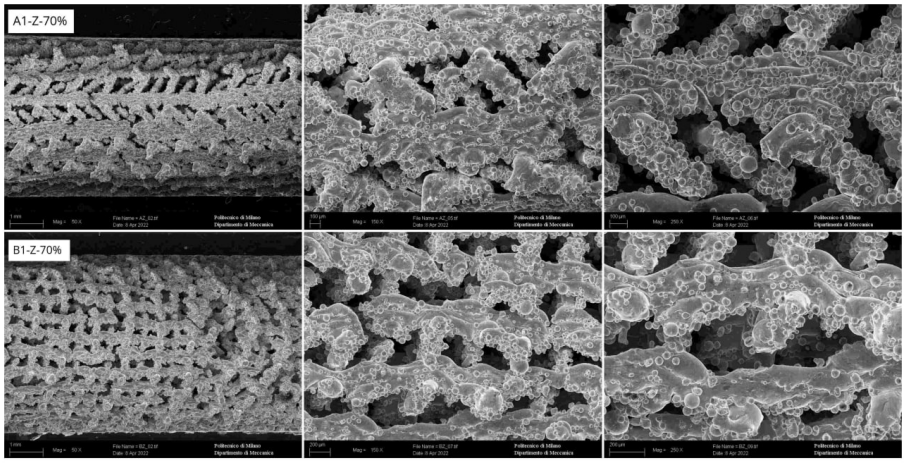

(a)

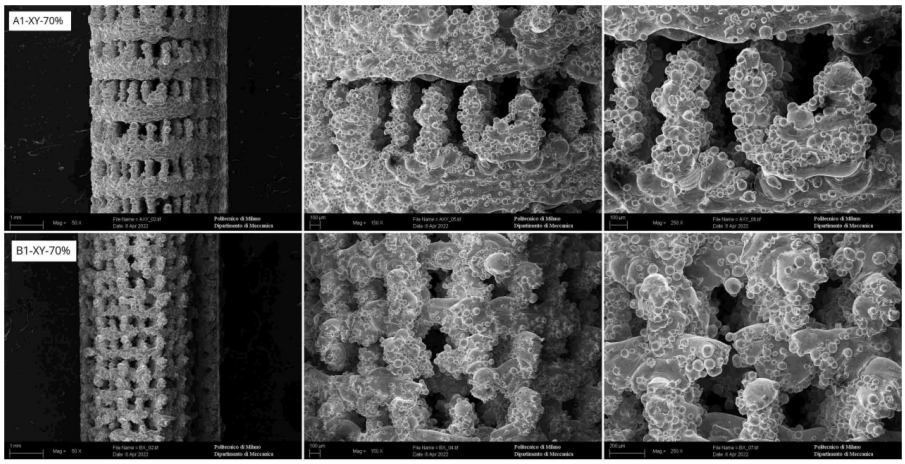

(b)

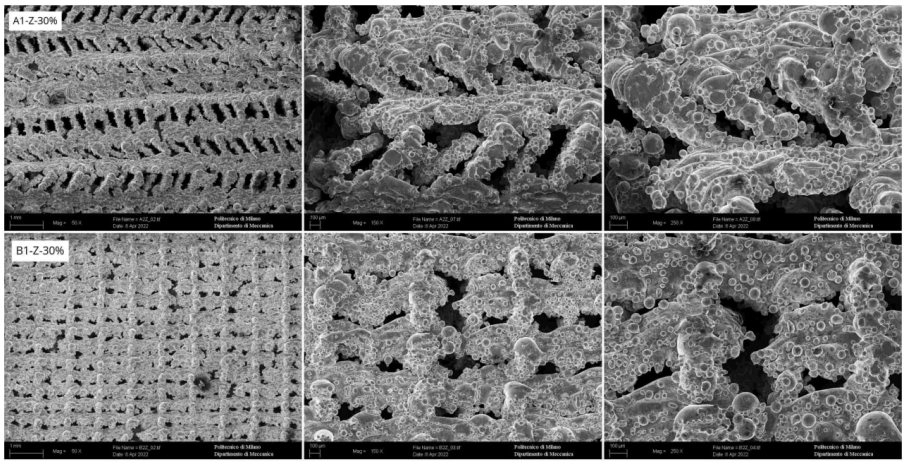

(c)

Figure 3.19: Compressed samples, Layer Number effect, A1 and B1 (a) Compression 70% along Z axis (b) Compression 70% along X/Y axis (c) Compression 30% along Z axis.

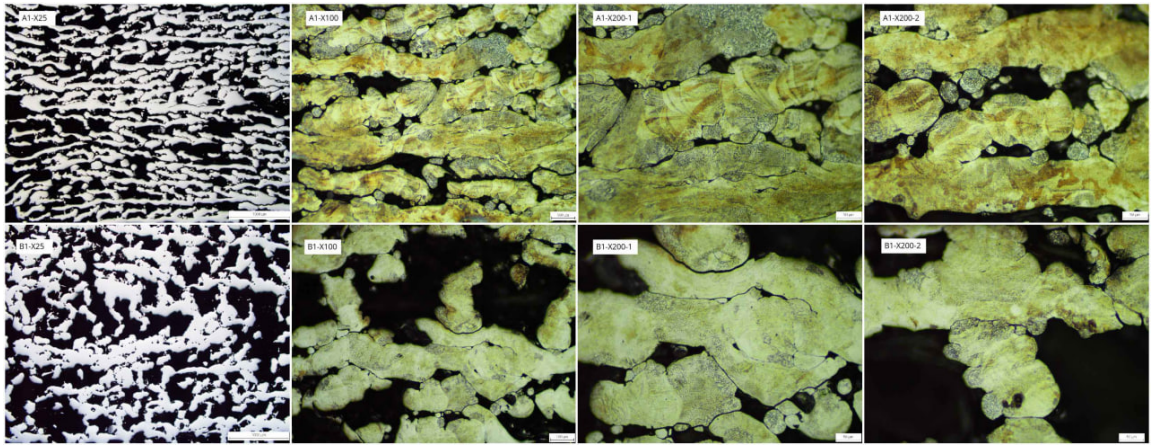

(a)

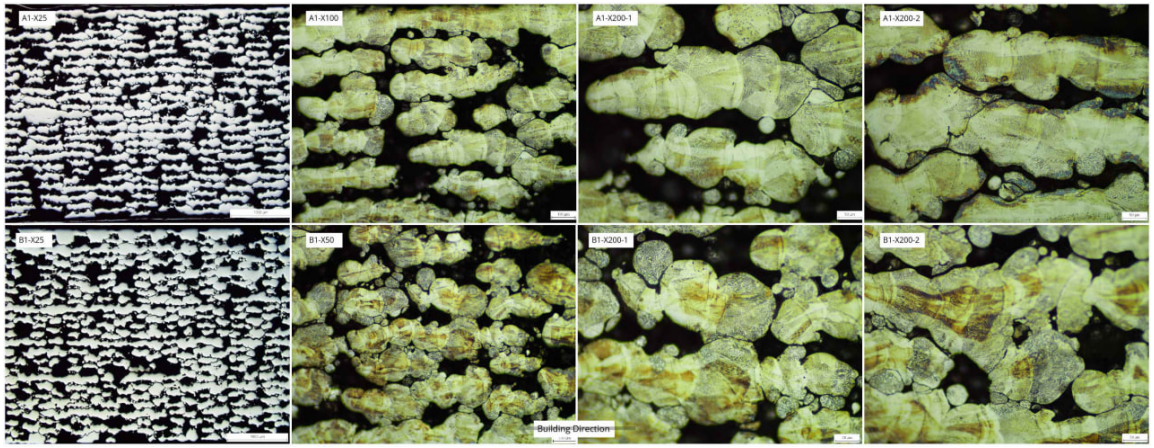

(b)

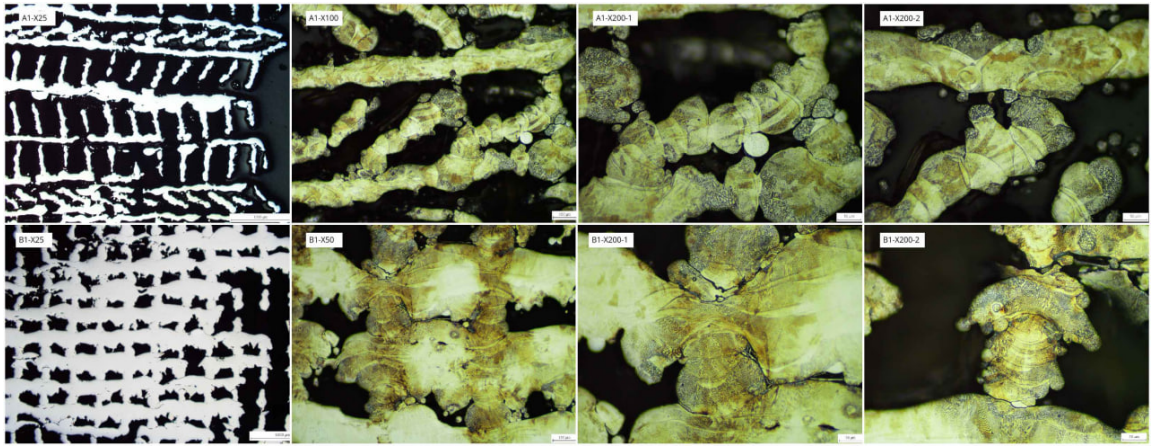

(c)

Figure 3.20: Compressed samples, Layer Number effect, A1 and B1 (a) Compression 70% along Z axis (b) Compression 70% along X/Y axis (c) Compression 30% along Z axis.

The graphs provided in Figure 3.21 are a presentation of the effect of the layer number on the compressive strength of the lattice and clearly show the difference in the compression behavior of two A and B samples with bending-dominated and stretch-dominated behaviors, respectively. In these graphs, each scanning speed of series A and B has been compared to each other individually. As can be seen, the difference in the shape of the stress-strain graphs confirms the absence of the failure in Serie B samples, while the sequential stress relief through the failure of the layers in Serie A samples with ten-layer repetition is revealed in the fluctuations in stress values. However, a quantitative look at the yielding graphs (Fig. 3.21b) shows quite similar behavior up to the initial 2.5% strain, which can be the elastic area of both structures. It is also possible to point out the similar responses of both structures to the decrease in scanning speed, which confirms the discussed results in the previous section.

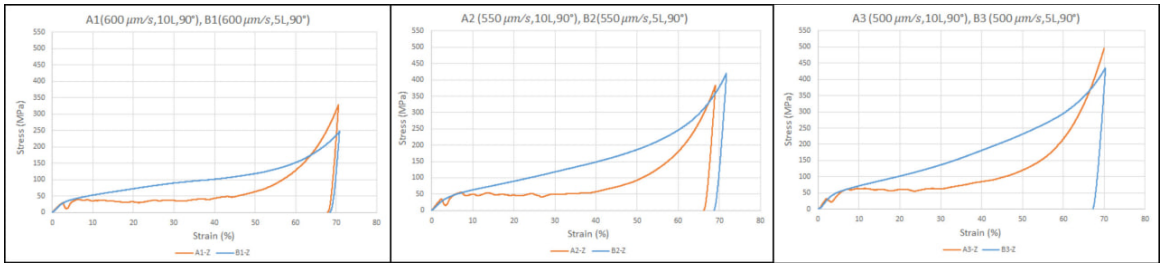

(a)

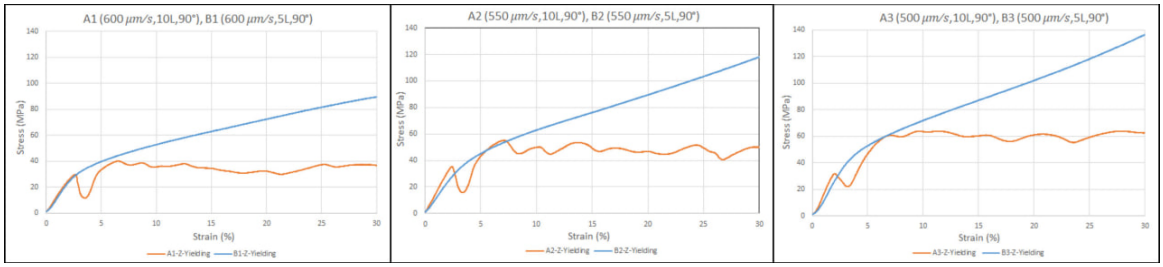

(b)

Figure 3.21: Compressed samples, Layer Number effect, A_1 and B_1 Compression 70% along Z axis

As previously mentioned, the larger view of these graphs is presented in Appendix A.7, and the study of the layer effect on the stress-strain graphs extracted from the compression tests in the X/Y direction also is presented in Appendix A.8.

3.2.3. Hatch Angle Effect

As a final parameter, the effect of the hatch angle on the microstructure and compressive test of the provided microlattices, similarly, has been investigated through the SEM, OM, and the stress strain graphs. These investigations have been selectively applied to the samples A_1 from Serie A with 90° hatch angle and sample C_1 from Serie C with 45° hatch angle, both with 600 μm/s scanning speeds.

As can be seen in Figure 3.22, the SEM pictures from the three compressed samples from each mentioned batch are indicated which show the compressed samples with 70% compression along the Z axis (Fig.3.22a), 70% compression along the X/Y axis (Fig.3.22b), and 30% compression again along the Z axis (Fig.3.22c) and with the same order, the OM pictures from the polished and etched cross-section of A_1 and C_1 samples are presented in Figure 3.23.

Considering the SEM pictures, it is visible that the compressed structure of both samples in 70% compression along the Z axis is quite similar; however, there are a few minor ruptures in the layers from the same hatch in C_1 while this is not observed in sample A_1. On the other hand, the 70% compression along the X/Y axis induced very different compressed structures in two samples, and the one with a 90-degree hatch angle still holds the lattice structure despite the extensive bending, but the one with a 45-degree hatch angle is completely destroyed. Finally, SEM pictures of the 30% compressed samples along the Z axis showed quite similar sliding behavior in lower stresses, which is possible to be correlated to the stress-strain graphs. However, the number of detachments between the layers from different hatches is higher in sample C_1 in comparison to sample A_1.

Correlating the mentioned observations in the SEM pictures to the acquired OM results presented in Figure 3.23, confirms all the mentioned facts about higher destruction of the lattice structure in compression along the X/Y axis in sample C_1 (Fig. 3.23b)and also a lower number of well-connected layers from different hatches. As can be seen in Figure 3.23a and Figure 3.23b, both samples represented a similar compressive behavior; however, considering the microstructural analysis, sample C_1 has a higher number of unmelted granular microstructures and disconnections in the lattice structure.

Considering Figure 3.23c, it is visible that the total interference between the ±45, ±90, and ±135 layers is less in samples with a 45-degree hatch angle and even in columns with perfectly melted microstructure the two consequent layers with different hatches are not connected, and cracks are visible in Figure 3.23c C_1 x200.

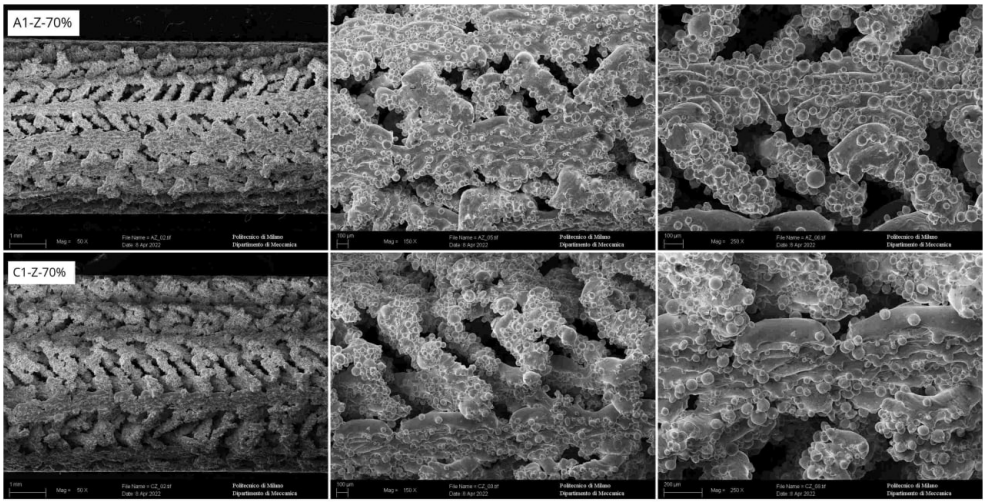

(a)

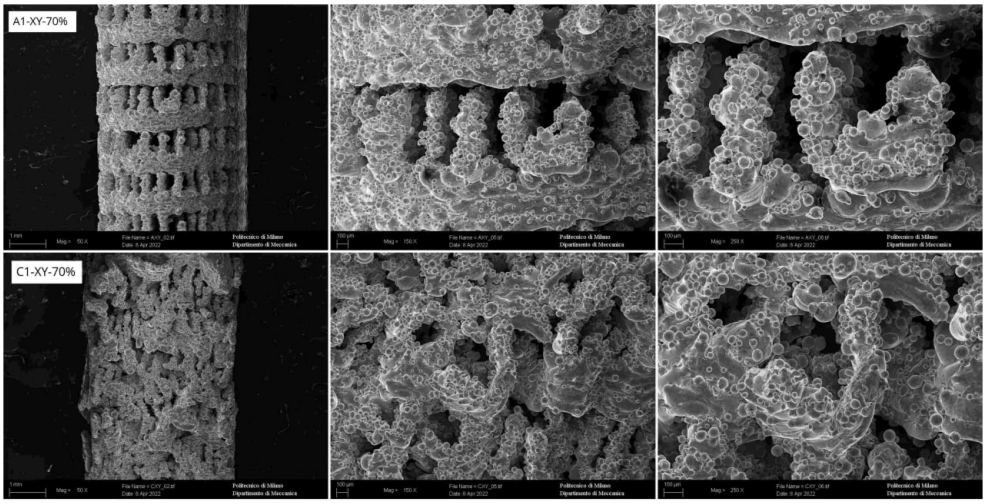

(b)

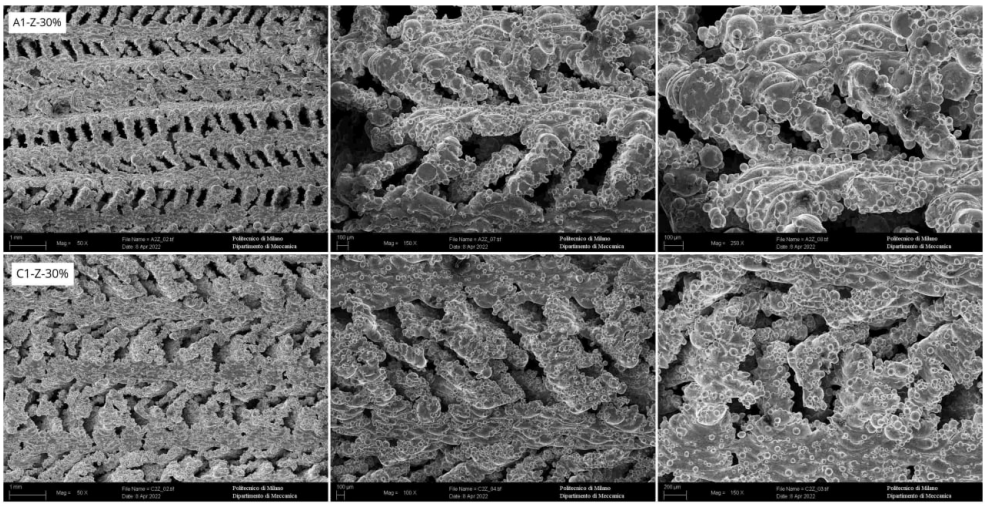

(c)

Figure 3.22: Compressed samples, Hatch Angle effect, A1 and C1 (a) Compression 70% along Z axis (b) Compression 70% along X/Y axis (c) Compression 30% along Z axis.

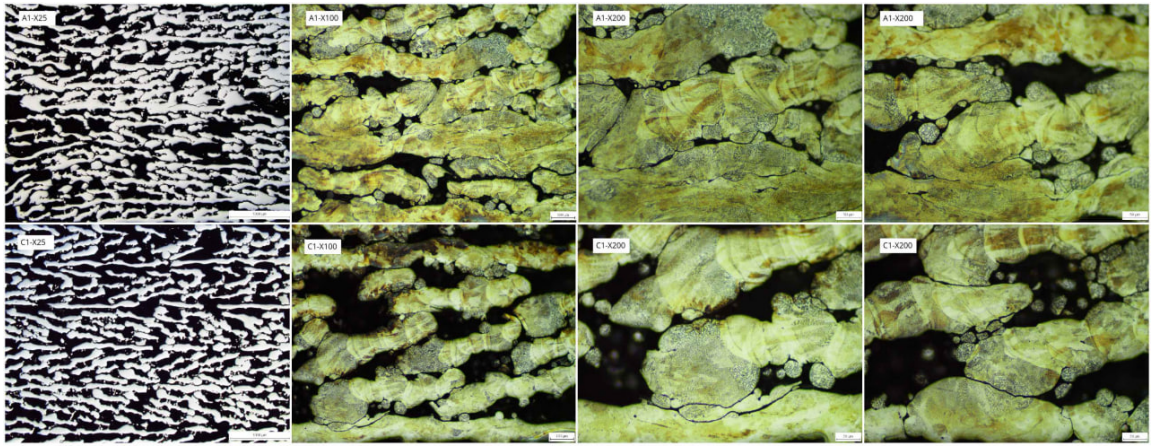

(a)

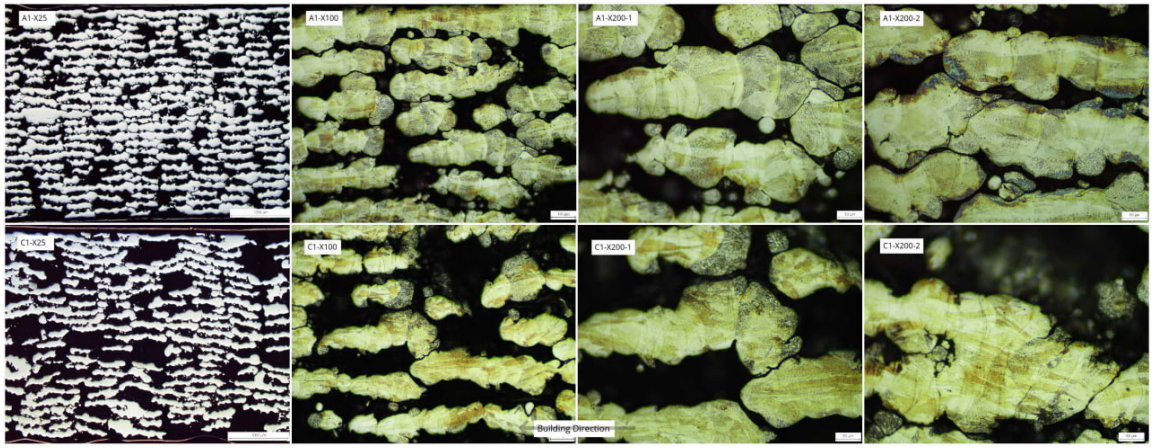

(b)

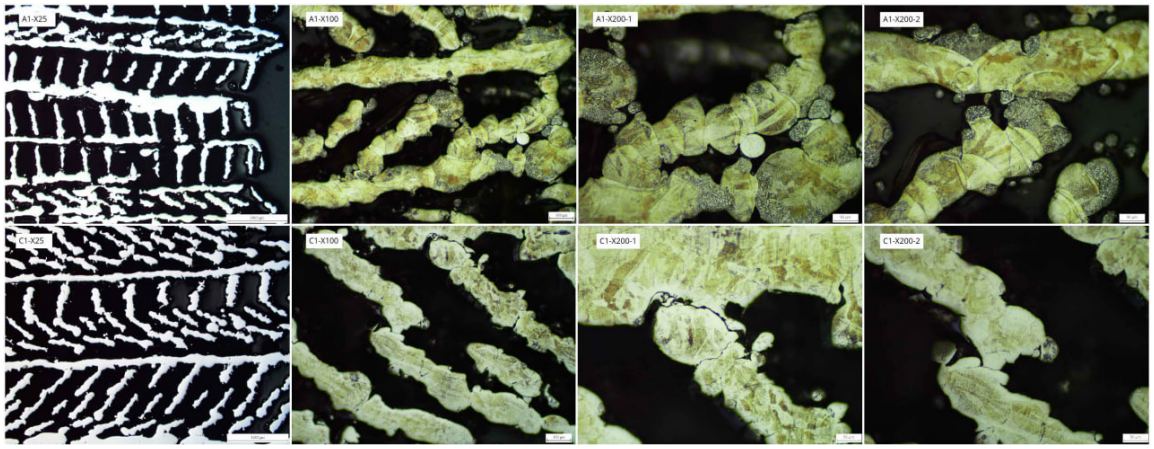

(c)

Figure 3.23: Compressed samples, Layer Number effect, A1 and B1 (a) Compression 70% along Z axis (b) Compression 70% along X/Y axis (c) Compression 30% along Z axis.

The provided stress-strain graphs for both samples in the compression test along the Z axis up to 70% of their initial eight are represented in the below-given Figure 3.24. Similarly, both the total strain range and the zoomed yield range are presented. Taking a close look at both graphs indicates that both series A and C with 10 layers of repetition regardless of the applied hatch angle have a bending-dominated compression behavior (Fig. 1.30) and also confirms the understood phenomenon from the microstructural data. Both samples show similar yielding behavior, which is a result of the sequential failure of the layers, and also show an almost continuous increase in stress after 30% strain, which is an indication of compaction in the microlattice.

It is important to point out the higher yielding stress that sample A_1 showed in comparison to sample C_1, which based on the correlation between the graphs and acquired OM results is due to the weak connections of the layers with different hatches in sample C_1 and also the higher number of columns with unmelted granular microstructure endings in comparison to sample A_1.

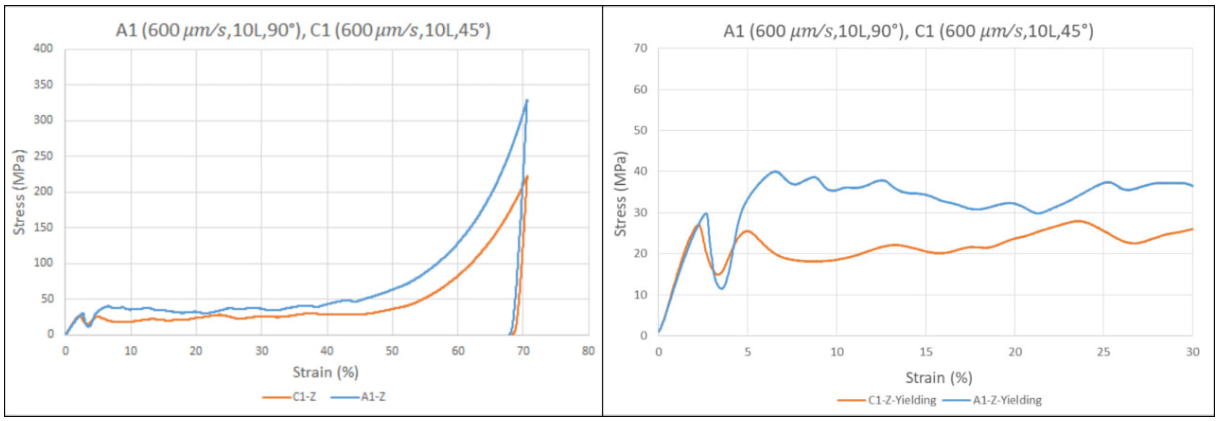

Figure 3.24: Compressed samples, Hatch Angle effect, A_1 and C_1 Compression 70% along Z axis

To summarize, unlike the similarities between samples with distinct layer numbers, the alternation of the hatch angle has obvious effects on the microstructure quality and compressive strength of the sample. Sample A_1 with a 90-degree hatch angle apparently provided better bonding between layers with different hatches and also higher yield stress in comparison to sample C_1.

3.3. DIC Results

As the last step of analyzing the printing parameters' effect on the provided microlattices, the digital image correlation test has been employed during the 30% compression test along the Z direction. As previously mentioned, the two primary 70% compression tests have been applied along the two different axes, and their results did not provide a complete understanding of the yielding behavior of the microlattices due to the complete destruction of the lattice structure caused by the application of excessive compressive loads. For this reason, an additional compression test has been employed with 30% compression along the Z direction in order to study mainly the yielding behavior of the samples.

During this compression test, the Aramis files have been recorded from the sample surface as mentioned in the previous chapter, to be analyzed through the GOM Correlate software, and the stress and strain at the failure points be assessed to provide a comprehensive understanding of the compression behavior of the present microlattices.

However, due to the micro-scale dimensions of the provided lattices, the desired data from the DIC test could not be extracted, and the main objective of this testing method was not fulfilled. As far as this test works on the surface area of the recorded sample, due to the very small lattice structure of the samples, the software was not able to identify the individual cells in the sample surface in order to identify the lattice distortions during straining and measure the stress and strain at the failed points, and the software identified the surface of the sample as a whole surface.

Meanwhile, despite the inability of the DIC software to identify the lattice surface, the recorded videos provided a complete and useful vision of the macroscopic strain and failure behavior of each sample. On the other hand, through the correlation of the corresponding stress-strain graph of the compression test that the DIC files have been recorded from, the precise definition of the failure behavior of the sample has been defined based on the stress value fluctuations to provide a better understanding of the compression and failure properties of each microlattice design.

3.3.1. Serie A

Starting with Serie A samples, three deformation reports from each scanning speed in Serie A have been provided in Figures 3.25, 3.26, and 3.27. Having a close look at all these results, the failure behavior of the samples has not been affected by reducing the scanning speed, and all the samples failed with a similar behavior regardless of the scanning speed. However, it is possible to mention that a decrease in scanning speed increased the yielding stresses in the stress-strain graphs (a comparison of the stress-strain graph of this compression test for three scanning speeds is presented in Appendix A.9).

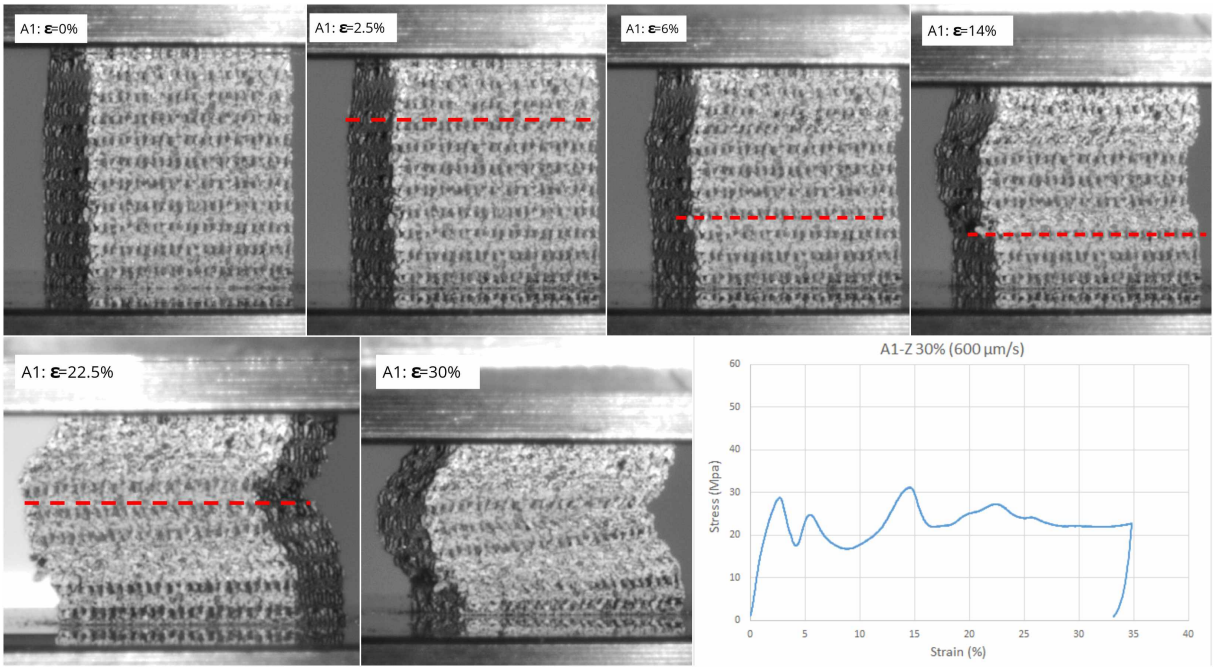

Figure 3.25: Serie A DIC- A_1 (600 μm/s).

Taking a close look at Figure 3.25, each layer that fails in the written strain and the corresponding drop in the stress value is identified based on correlating the given times in the compression test results and the time indicated in the Aramis files. It is clear through the acquired videos and presented deformation procedure that the drop in the stress level is due to the failure of one layer, and the subsequent increase in the stress level is related to both the compaction of the failed layer and reaching the yielding level of the next failing layer, and this sequence continues until reaching the final 30% strain.

The same discussions can be mentioned for the provided deformations on the samples A_2 and A_3 presented in Figure 3.26, and 3.27, respectively.

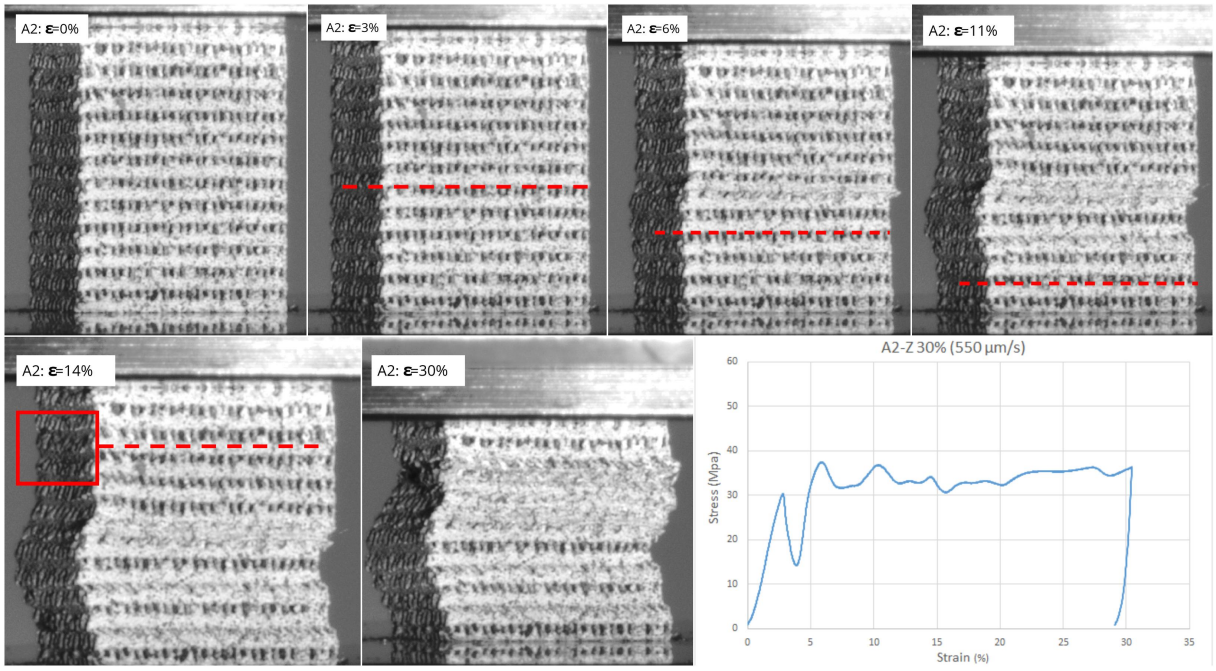

Figure 3.26: Serie A DIC- A_2 (550 μm/s).

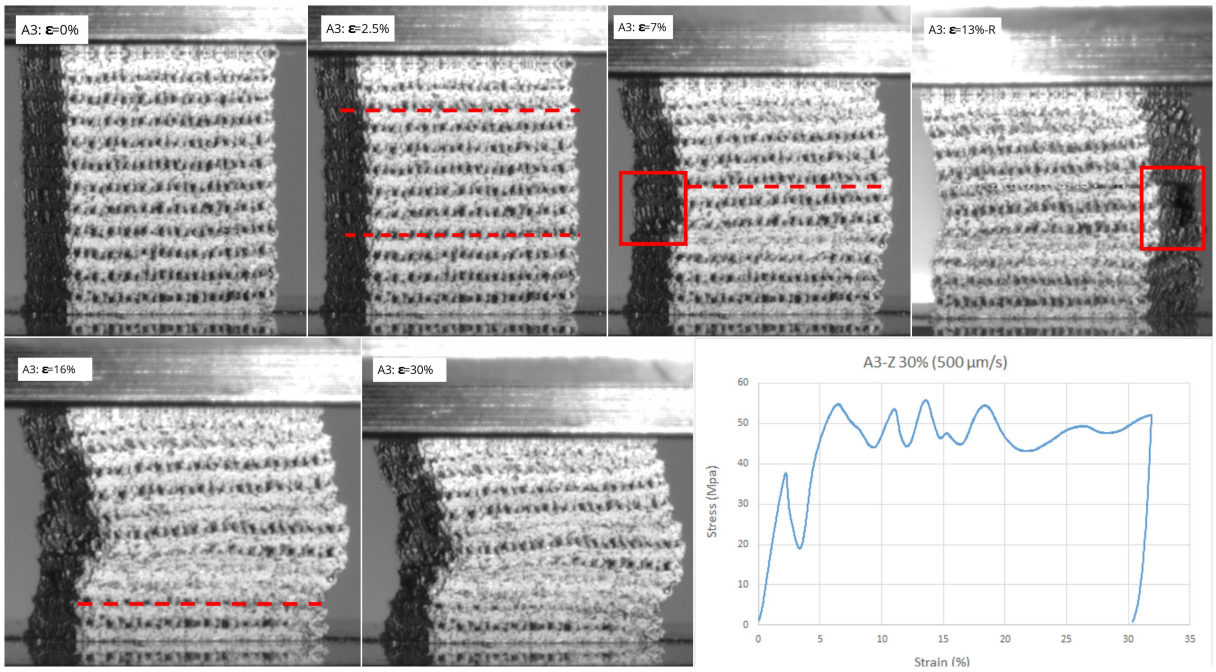

Figure 3.27: Serie A DIC- A_3 (500 μm/s).

3.3.2. Serie B

Considering the DIC analysis that has been performed on Serie B samples, the below-given Figure3.28 could be represented as a final result. As previously mentioned multiple times, the Serie B samples do not fail or experience the sliding phenomena, so there is not so much information to be mentioned from the DIC results, and only the bulking of the sample and the curvy shape of the sample that can be seen by the end of the compression test. However, the correlation between the stress-strain graph and the sequence of the strain stress-strain progress could be highlighted as the compression behavior of the sample with five layers of repetition and a 90-degree hatch angle.

On the other hand, it is also possible to mention the increase in the level of achieved stress for the same strain by decreasing the scanning speed, which has been discussed frequently in previous sections.

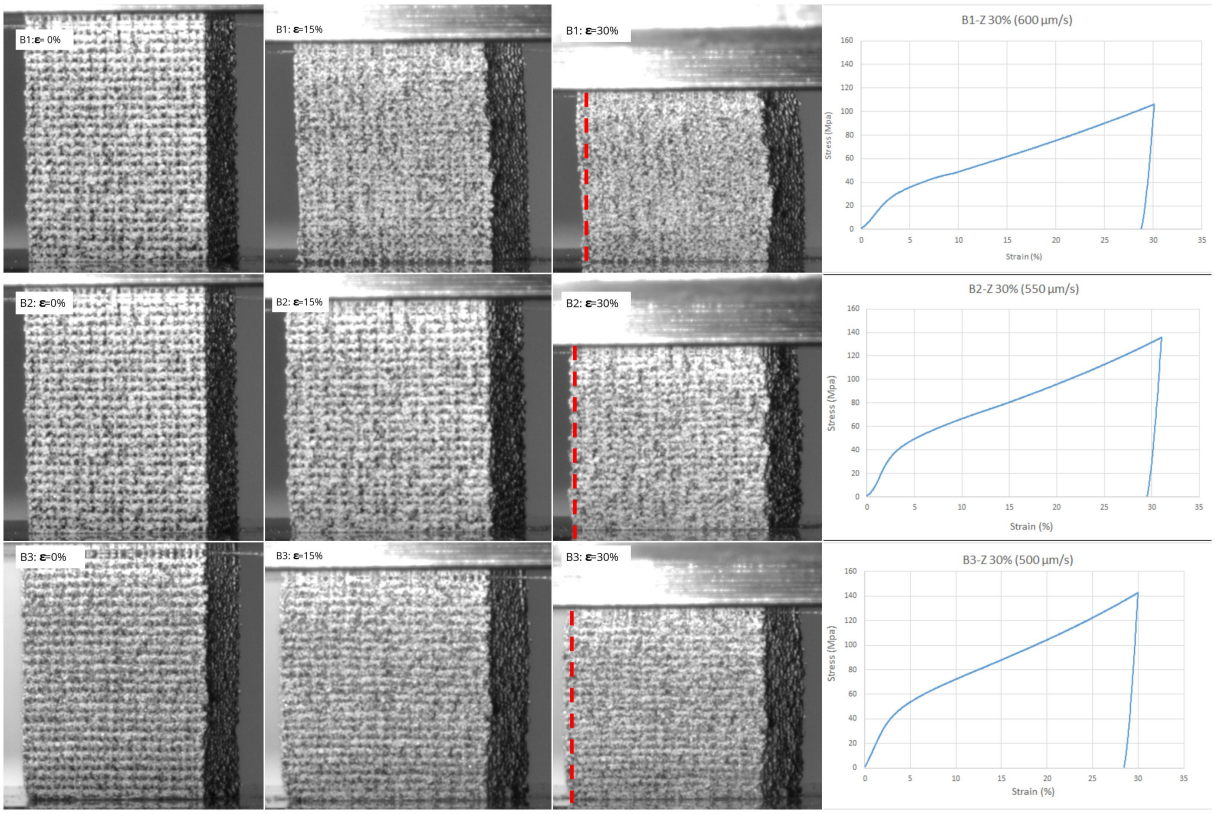

Figure 3.28: Serie B DIC- B_1 (600 μm/s),B_2 (550 μm/s), B_3 (500 μm/s).

Additionally, the comparison of the stress-strain graph of this compression test for three scanning speeds of Series B samples is presented in Appendix A.10.

3.3.3. Serie C

The last sample that has been analyzed through the DIC method is sample C_1 from Serie C with 600 μm/s scanning speed, 10-layer repetition, and a 45-degree hatch angle.

As can be seen in the below-given Figure 3.29 and previously mentioned, the failure and compression behavior of samples with ten-layer repetition (A and C) are quite similar, and both series fail through layer-by-layer failure and yielding and represent the fluctuation in their stress values in the plotted stress-strain graph.

In comparing the failure modes of the A and C series, it is possible to mention that the sliding and failure of individual layers is much more severe in the Serie C sample with a 45-degree hatch angle, and it occurs at lower stresses in comparison to the similar sample from Serie A.

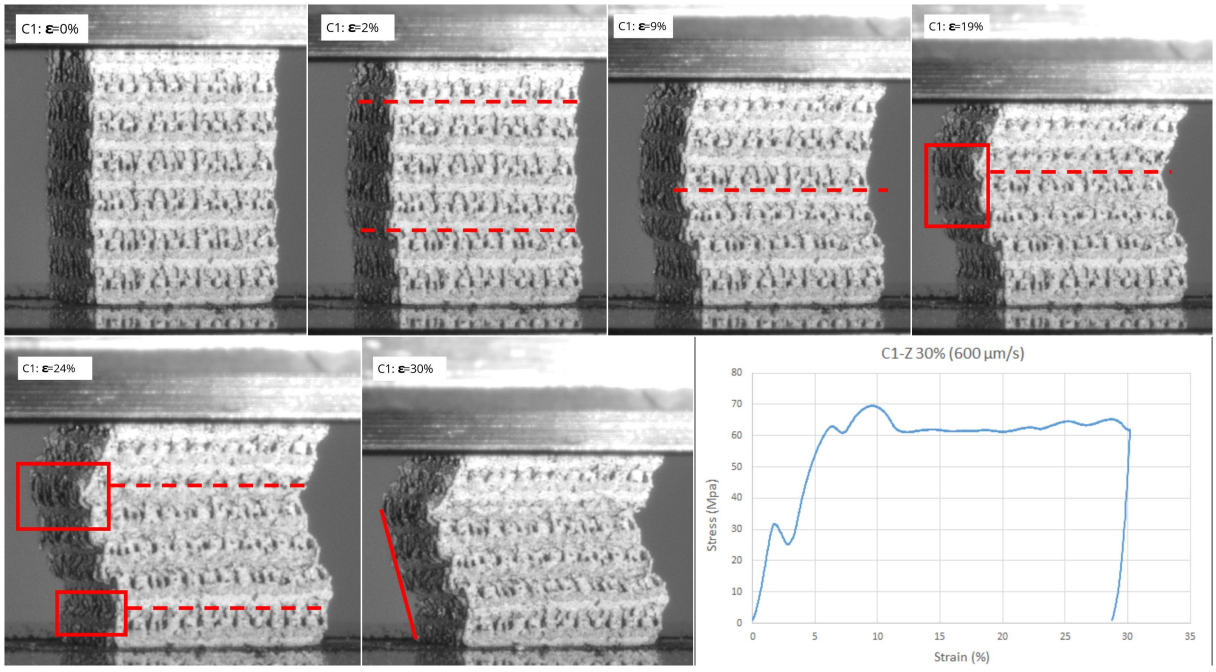

Figure 3.29: Serie C DIC-C_1 (600 μm/s)

4 | Conclusion

4.1. Conclusion

The dominance and great impact of metal additive manufacturing in all industries are unveiled to every scholar who is active in this field. The metal AM industry's evolution is as fast as before the publication of this work, new developments in methods, materials, and applications of AM other than those mentioned in this work will be introduced. In the meantime, the importance of microlattice structures in today's high-tech industries has attracted multiple researchers to investigate their potential properties and optimize the manufacturing methods of these structures.

All these indicated importance built the foundation of the current work, and this master's thesis embarked on a comprehensive exploration of laser powder bed fusion (L-PBF) parameter optimization specifically tailored for the fabrication of stainless steel 316L porous microlattices. The aim was to unravel the relationship between printing parameters, microstructure, and mechanical properties, contributing to the advancement of additive manufacturing techniques in the context of metallic porous microlattices. The fact that made this research a unique and pioneering work among other related ones is the use of printing parameters like hatch angle, hatch distance, and lattice design as the manufacturing means instead of utilizing the CAD and STL files for manufacturing the desired microlattice structure as is mostly done in other research.

The extensive investigation of seven distinct batches of samples, each varying in scanning speeds, layer repetitions, and hatch angles, has yielded profound insights specific to the realm of metallic porous microlattices. By leveraging sophisticated analytical tools such as scanning electron microscopy (SEM), optical microscopy (OM), and compression tests coupled with Digital Image Correlation (DIC) analysis, we figured out the impacts of varying printing parameters on the microstructure and mechanical properties of these intricate structures.

Considering the acquired results, the fracture and failure behavior between sets was different, but the microstructure of samples and the fracture behavior in terms of fracture

initiation points, which were the joints between layers from different hatches with the unmelted microstructure, were quite similar for all the batches with different parameters. However, the fracture and failure behavior of the batches in terms of yielding and maximum achieved stresses were quite distinct, and different structures and speeds revealed different compressive strengths.

The comparison of the effects of each parameter has shown that scanning speed has the most significant impact on the level of compressive strength and increases the yielding and maximum achieved stresses, which corresponds to the increase in the delivered energy to the powder bed by reducing the scanning speed. The increase in the delivered energy causes a higher temperature and thus a deeper melt pool that reduces porosities, reduces the number of unmelted granular regions, and increases the remelting of previous layers. All these effects result in a better attachment of layers and delay the yielding of the microlattice structure.

Considering the hatch angle effect, samples from Serie A with a 90° hatch angle showed higher compressive strength compared to the sample from Serie C with a 45° hatch angle. The microstructural data from OM results do not show that much difference between the two series, while stress-strain graphs confirm that hatch angle affects the compressive strength, and Serie A samples showed higher yielding and maximum achieved stress compared to Serie C samples. On the other hand, the compression behavior of samples was not affected by hatch angle, and the stress-strain graph of samples from both series showed a bending-dominated compression behavior.

Studying the effect of the number of layers, consideration of the OM and SEM results revealed that Serie B samples with five layers of repetition in each hatch had a higher number of disorders in the lattice structure, while Serie A samples with ten layers of repetition in each hatch showed much more ordered lattice cells and high discipline in the lattice structure. On the other hand, samples with 10 layers (A) had less compressive strength in comparison to samples with 5 layers (B). The results from OM, SEM, and DIC confirmed that Serie A samples have columns with much longer lengths that bend easily with lower applied stresses, and the samples represent a bending-dominated compression behavior. However, Serie B samples with five layers have short columns, which, instead of bending and failure of the layers, just get compact, and there is no failure in between layers and a stretch-dominated behavior can be detected from their stree-strain graphs. These findings are then supported by the correlation of the DIC results with the stress-strain graphs in the yielding area since, in Serie A samples, the graphs showed a fluctuation in which each of the drops in stress level was related to the failure of a layer, while the graphs for Serie B samples showed no fluctuation and just a uniform increase in stress

was measured which could be highlighted as the desired compression behavior.

It is important to mention that regardless of varying parameters, all the samples represented a bending-dominated compression behavior in compression tests along the X/Y direction, which through the SEM results can be interpreted as happening due to the bending of the resistant strut in all samples.

To sum up all varying parameters, the results underscored the significance of a lower number of layer repetitions, reduced scanning speed, and a 90° hatch angle in achieving optimal mechanical properties for Stainless Steel 316L porous microlattices. These parameter configurations not only enhanced microstructural characteristics but also manifested a substantial improvement in compressive strength, affirming the critical role of parameter optimization in the L-PBF process specifically for metallic porous microlattices.

4.2. Upcoming Perspectives

In considering the broader implications of this research, the significance of metallic porous microlattices in diverse applications cannot be overstated. Metallic porous microlattices, with their unique combination of mechanical properties and structural efficiency resulting from optimized L-PBF parameters, hold promise in various industries. In aerospace, the lightweight nature of these structures can contribute to fuel efficiency and overall performance. In biomedical engineering, the biocompatibility of materials like Stainless Steel 316L, coupled with the optimized fabrication process, makes metallic porous microlattices particularly attractive for implant applications. Additionally, the potential for heat dissipation and energy absorption positions metallic porous microlattices as valuable components in the automotive and energy sectors. The successful optimization of L-PBF parameters for metallic porous microlattices brings these applications closer to reality, unlocking new possibilities for the integration of metallic porous microlattices into mainstream manufacturing processes.

While this research has provided new insights specific to metallic porous microlattice manufacturing, it also highlights avenues for future exploration within this sector. Further studies in order to illustrate more lights to the L-PBF parameter optimization unaddressed challenges could be testing a higher number of samples with a broader range of scanning speeds, hatch angles, and layer numbers to confirm the certainty of the discussed theories and optimize the microlattices based on the industrial aim requirements. Investigating the scalability of optimized parameter configurations for stainless steel 316L porous microlattices in an industrial setting is crucial for bridging the gap between laboratory findings and practical applications in the context of metallic porous microlattices

and could be an exciting step to be taken in future studies.

In conclusion, this master's thesis has not only advanced our understanding of Laser Powder Bed Fusion parameter optimization for Stainless Steel 316L porous microlattices but has also set the stage for transformative advancements in the field of additive manufacturing specifically tailored for metallic porous microlattices. The profound impact of optimized parameters on the microstructure and mechanical properties of microlattices is a testament to the potential of this technology within this specialized domain. As we look toward the future, the insights gained from this research provide a solid foundation for continued exploration and innovation, propelling the field of metallic porous microlattice manufacturing into new frontiers of possibility.

Bibliography

[1] F. Abe, K. Osakada, Y. Kitamura, M. Matsumoto, and M. Shiomi. Manufacturing of titanium parts for medical purposes by selective laser melting. *Proc. 8th Int. Conf. Rapid Prototyping*, pages 288–293, 01 2000.

[2] C. Beyer. Strategic Implications of Current Trends in Additive Manufacturing. *Journal of Manufacturing Science and Engineering*, 136(6):064701, 10 2014. ISSN 1087-1357. doi: 10.1115/1.4028599. URL https://doi.org/10.1115/1.4028599.

[3] C. Beyer and D. Figueroa. Design and Analysis of Lattice Structures for Additive Manufacturing. *Journal of Manufacturing Science and Engineering*, 138(12):121014, 09 2016. ISSN 1087-1357. doi: 10.1115/1.4033957. URL https://doi.org/10.1115/1.4033957.

[4] K. S. Boparai, R. Singh, and H. Singh. Development of rapid tooling using fused deposition modeling: a review. *Rapid Prototyping Journal*, 22(2):281–299, 2016.

[5] K. Budinski and M. Budinski. *Engineering Materials: Properties and Selection*. Prentice Hall, 2002. ISBN 9780130305336. URL https://books.google.it/books?id=E6seAQAAIAAJ.

[6] F. Calignano, D. Manfredi, E. P. Ambrosio, S. Biamino, M. Lombardi, E. Atzeni, A. Salmi, P. Minetola, L. Iuliano, and P. Fino. Overview on additive manufacturing technologies. *Proceedings of the IEEE*, 105(4):593–612, 2017. doi: 10.1109/JPROC.2016.2625098.

[7] F. Careri, R. H. Khan, C. Todd, and M. M. Attallah. Additive manufacturing of heat exchangers in aerospace applications: a review. *Applied Thermal Engineering*, 235:121387, 2023. ISSN 1359-4311. doi: https://doi.org/10.1016/j.applthermaleng.2023.121387. URL https://www.sciencedirect.com/science/article/pii/S1359431123014163.

[8] S. Crump. Apparatus and method for creating three-dimensional objects. In *U.S. Patent No. 5,121,329*. U.S. Patent and Trademark Office, 1992.

[9] J. Dawes, R. Bowerman, and R. Trepleton. Introduction to the additive manufacturing powder metallurgy supply chain. *Johnson Matthey Technology Review*, 59: 243–256, 07 2015. doi: 10.1595/205651315X688686.

[10] S. R. F. P. O. W. et al. The development of a scanning strategy for the manufacture of porous biomaterials by selective laser melting. *T J Mater Sci: Mater Med*, 20: 1839–1848, 06 2009. doi: https://doi.org/10.1007/s10856-009-3763-8.

[11] V. A. D. S. K. A. et al. Additive manufacturing of 3d nano-architected metals. *Nature Communication 9,593*, 2018. doi: https://doi.org/10.1038/s41467-018-03071-9.

[12] G. Fuquan and S. A. A. Precise deposition of molten microdrops: the physics of digital microfabrication. *Proc. R. Soc. Lond. A*, 444:533–554, 1994. doi: http://doi.org/10.1098/rspa.1994.0037.

[13] B. Gao, H. Zhao, L. Peng, and Z. Sun. A review of research progress in selective laser melting (slm). *Micromachines*, 14(1), 2023. ISSN 2072-666X. doi: 10.3390/mi14010057. URL `https://www.mdpi.com/2072-666X/14/1/57`.

[14] I. Gibson and D. Shi. Material properties and fabrication parameters in selective laser sintering process. *Rapid prototyping journal*, 3(4):129–136, 1997.

[15] I. Gibson, D. Rosen, B. Stucker, and M. Khorasani. *Development of Additive Manufacturing Technology*, pages 23–51. Springer International Publishing, Cham, 2021. ISBN 978-3-030-56127-7. doi: 10.1007/978-3-030-56127-7_2. URL `https://doi.org/10.1007/978-3-030-56127-7_2`.

[16] A. Großmann, J. Gosmann, and C. Mittelstedt. Lightweight lattice structures in selective laser melting: Design, fabrication and mechanical properties. *Materials Science and Engineering: A*, 766:138356, 2019. ISSN 0921-5093. doi: https://doi.org/10.1016/j.msea.2019.138356. URL `https://www.sciencedirect.com/science/article/pii/S0921509319311426`.

[17] P. Hanzl, M. Zetek, T. Bakša, and T. Kroupa. The influence of processing parameters on the mechanical properties of slm parts. *Procedia Engineering*, 100:1405–1413, 2015. ISSN 1877-7058. doi: https://doi.org/10.1016/j.proeng.2015.01.510. URL `https://www.sciencedirect.com/science/article/pii/S1877705815005378`. 25th DAAAM International Symposium on Intelligent Manufacturing and Automation, 2014.

[18] W. Harun, N. Manam, M. Kamariah, S. Sharif, A. Zulkifly, I. Ahmad, and H. Miura. A review of powdered additive manufacturing techniques for ti-6al-4v biomedical

applications. *Powder Technology*, 331:74–97, 2018. ISSN 0032-5910. doi: https://doi.org/10.1016/j.powtec.2018.03.010. URL https://www.sciencedirect.com/science/article/pii/S0032591018301931.

[19] Y. Hosni and R. Sundaram. Rapid prototyping and tooling: A survey and applications. In *Current Advances in Mechanical Design and Production VI*, pages 511–520. Elsevier, 1995.

[20] C. W. Hull. Apparatus for production of three-dimensional objects by stereolithography. In *U.S. Patent No. 4575330.* U.S. Patent and Trademark Office, 1986.

[21] P. Jacobs, D. Reid, Computer, and A. S. A. of SME. *Rapid Prototyping & Manufacturing: Fundamentals of Stereolithography.* Society of Manufacturing Engineers, 1992. ISBN 9780872634251. URL https://books.google.it/books?id=HvcN0w1VyxwC.

[22] C. R. D. J. J. B. Jr. Selective laser sintering with assisted powder handling. In *U.S. Patent No. 4561434.* United States Patent and Trademark Office, 1991.

[23] J.-P. Kruth, P. Mercelis, J. Vaerenbergh, L. Froyen, and M. Rombouts. Binding mechanisms in selective laser sintering and selective laser melting. *Rapid Prototyping Journal*, 11:26–36, 02 2005. doi: 10.1108/13552540510573365.

[24] T. Kurzynowski, E. Chlebus, B. Kuźnicka, and J. Reiner. Parameters in selective laser melting for processing metallic powders. *Proceedings of SPIE*, 8239:823914, 02 2012. doi: 10.1117/12.907292.

[25] P. Köhnen, C. Haase, J. Bültmann, S. Ziegler, J. H. Schleifenbaum, and W. Bleck. Mechanical properties and deformation behavior of additively manufactured lattice structures of stainless steel. *Materials Design*, 145:205–217, 2018. ISSN 0264-1275. doi: https://doi.org/10.1016/j.matdes.2018.02.062. URL https://www.sciencedirect.com/science/article/pii/S0264127518301539.

[26] M. Lalegani Dezaki, A. Serjouei, A. Zolfagharian, M. Fotouhi, M. Moradi, M. Ariffin, and M. Bodaghi. A review on additive/subtractive hybrid manufacturing of directed energy deposition (ded) process. *Advanced Powder Materials*, 1(4):100054, 2022. ISSN 2772-834X. doi: https://doi.org/10.1016/j.apmate.2022.100054. URL https://www.sciencedirect.com/science/article/pii/S2772834X22000379.

[27] T. Larimian, M. Kannan, D. Grzesiak, B. AlMangour, and T. Borkar. Effect of energy density and scanning strategy on densification, microstructure and mechanical properties of 316l stainless steel processed via selective laser melting. *Materials Science and Engineering: A*, 770:138455, 2020. ISSN 0921-5093. doi:

https://doi.org/10.1016/j.msea.2019.138455. URL https://www.sciencedirect.com/science/article/pii/S0921509319312419.

[28] R. Larson. Method and device for producing three-dimensional bodies, July 28 1998. US Patent 5,786,562.

[29] H. Li, M. Ramezani, M. Li, C. Ma, and J. Wang. Effect of process parameters on tribological performance of 316l stainless steel parts fabricated by selective laser melting. *Manufacturing Letters*, 16:36–39, 2018. ISSN 2213-8463. doi: https://doi.org/10.1016/j.mfglet.2018.04.003. URL https://www.sciencedirect.com/science/article/pii/S2213846317300810.

[30] P. Liu and G.-F. Chen. *Porous materials: processing and applications*. Elsevier, 2014.

[31] G. I. R. D. S. B. K. Mahyar. *Hybrid Additive Manufacturing*, pages 347–366. Springer International Publishing, Cham, 2021. ISBN 978-3-030-56127-7. doi: 10.1007/978-3-030-56127-7_12. URL https://doi.org/10.1007/978-3-030-56127-7_12.

[32] D. Manfredi, F. Calignano, E. Ambrosio, M. Krishnan, R. Canali, S. Biamino, M. Pavese, E. Atzeni, L. Iuliano, P. Fino, and C. Badini. Direct metal laser sintering: An additive manufacturing technology ready to produce lightweight structural parts for robotic applications. *La Metallurgia Italiana*, 105, 10 2013.

[33] J. O. Milewski. *Additive Manufacturing of Metals: From Fundamental Technology to Rocket Nozzles, Medical Implants, and Custom Jewelry*, volume 258. Springer Series in Materials Science, 2017. URL https://api.semanticscholar.org/CorpusID:136050727.

[34] R. Mines. *Additive Manufacturing Processes and Materials for Metallic Microlattice Structures Using Selective Laser Melting, Electron Beam Melting and Binder Jetting*, pages 17–31. Springer International Publishing, Cham, 2019. ISBN 978-3-030-15232-1. doi: 10.1007/978-3-030-15232-1_3. URL https://doi.org/10.1007/978-3-030-15232-1_3.

[35] L. Murr, E. Esquivel, S. Quinones, S. Gaytan, M. Lopez, E. Martinez, F. Medina, D. Hernandez, E. Martinez, J. Martinez, S. Stafford, D. Brown, T. Hoppe, W. Meyers, U. Lindhe, and R. Wicker. Microstructures and mechanical properties of electron beam-rapid manufactured ti–6al–4v biomedical prototypes compared to wrought ti–6al–4v. *Materials Characterization*, 60(2):96–105, 2009. ISSN 1044-5803. doi: https://doi.org/10.1016/j.matchar.2008.07.006. URL https://www.sciencedirect.com/science/article/pii/S1044580308002076.

[36] G. T. Murray. *Handbook of Materials Selection for Engineering Applications Mechanical Engineering*. CRC Press, 1997.

[37] D. S. Nagaraju, R. Krupakaran, C. Sripadh, G. Nitin, and G. Joy Joseph Emmanuel. Mechanical properties of 3d printed specimen using fdm (fused deposition modelling) and sla (stereolithography) technologies. *Materials Today: Proceedings*, 2023. ISSN 2214-7853. doi: https://doi.org/10.1016/j.matpr.2023.09.223. URL https://www.sciencedirect.com/science/article/pii/S2214785323049040.

[38] T. Nakano and T. Ishimoto. Powder-based additive manufacturing for development of tailor-made implants for orthopedic applications. *KONA Powder and Particle Journal*, 32:75–84, 02 2015. doi: 10.14356/kona.2015015.

[39] T. D. Ngo, A. Kashani, G. Imbalzano, K. T. Nguyen, and D. Hui. Additive manufacturing (3d printing): A review of materials, methods, applications and challenges. *Composites Part B: Engineering*, 143:172–196, 2018. ISSN 1359-8368. doi: https://doi.org/10.1016/j.compositesb.2018.02.012. URL https://www.sciencedirect.com/science/article/pii/S1359836817342944.

[40] A. C. F. on Additive Manufacturing Technologies and A. C. F. on Additive Manufacturing Technologies. Subcommittee F42. 91 on Terminology. *Standard terminology for additive manufacturing technologies*. Astm International, 2012.

[41] C. Pan, Y. Han, and J. Lu. Design and optimization of lattice structures: A review. *Applied Sciences*, 10(18), 2020. ISSN 2076-3417. doi: 10.3390/app10186374. URL https://www.mdpi.com/2076-3417/10/18/6374.

[42] L. Parry, I. Ashcroft, and R. Wildman. Understanding the effect of laser scan strategy on residual stress in selective laser melting through thermo-mechanical simulation. *Additive Manufacturing*, 12:1–15, 2016. ISSN 2214-8604. doi: https://doi.org/10.1016/j.addma.2016.05.014. URL https://www.sciencedirect.com/science/article/pii/S2214860416300987.

[43] V. Petrovic, J. Vicente Haro Gonzalez, O. Jordá Ferrando, J. Delgado Gordillo, J. Ramón Blasco Puchades, and L. Portolés Griñan. Additive layered manufacturing: sectors of industrial application shown through case studies. *International Journal of Production Research*, 49(4):1061–1079, 2011.

[44] E. M. Sachs, M. J. Cima, and J. A. Cornie. Three dimensional printing: Rapid tooling and prototypes directly from cad representation. *1990 International Solid Freeform Fabrication Symposium*, 1990. URL https://api.semanticscholar.org/CorpusID:139820312.

[45] V. Sagias, K. Giannakopoulos, and C. Stergiou. Mechanical properties of 3d printed polymer specimens. *Procedia Structural Integrity*, 10:85–90, 2018. ISSN 2452-3216. doi: https://doi.org/10.1016/j.prostr.2018.09.013. URL https://www.sciencedirect.com/science/article/pii/S2452321618300611. 1st International Conference of the Greek Society of Experimental Mechanics of Materials,Athens, May 10-12, 2018.

[46] U. Scipioni Bertoli, A. J. Wolfer, M. J. Matthews, J.-P. R. Delplanque, and J. M. Schoenung. On the limitations of volumetric energy density as a design parameter for selective laser melting. *Materials Design*, 113:331–340, 2017. ISSN 0264-1275. doi: https://doi.org/10.1016/j.matdes.2016.10.037. URL https://www.sciencedirect.com/science/article/pii/S0264127516313363.

[47] U. Scipioni Bertoli, B. E. MacDonald, and J. M. Schoenung. Stability of cellular microstructure in laser powder bed fusion of 316l stainless steel. *Materials Science and Engineering: A*, 739:109–117, 2019. ISSN 0921-5093. doi: https://doi.org/10.1016/j.msea.2018.10.051. URL https://www.sciencedirect.com/science/article/pii/S0921509318314230.

[48] H. Shipley, D. McDonnell, M. Culleton, R. Coull, R. Lupoi, G. O'Donnell, and D. Trimble. Optimisation of process parameters to address fundamental challenges during selective laser melting of ti-6al-4v: A review. *International Journal of Machine Tools and Manufacture*, 128:1–20, 2018. ISSN 0890-6955. doi: https://doi.org/10.1016/j.ijmachtools.2018.01.003. URL https://www.sciencedirect.com/science/article/pii/S0890695518300233.

[49] B. Song, S. Wen, C. Yan, Q. Wei, and Y. Shi. Chapter 3 - preparation and processing of metal materials. In B. Song, S. Wen, C. Yan, Q. Wei, and Y. Shi, editors, *Selective Laser Melting for Metal and Metal Matrix Composites*, 3D Printing Technology Series, pages 35–88. Academic Press, 2021. ISBN 978-0-08-103005-9. doi: https://doi.org/10.1016/B978-0-08-103005-9.00003-1. URL https://www.sciencedirect.com/science/article/pii/B9780081030059000031.

[50] F. Tamburrino, S. Graziosi, and M. Bordegoni. The Design Process of Additively Manufactured Mesoscale Lattice Structures: A Review. *Journal of Computing and Information Science in Engineering*, 18(4):040801, 07 2018. ISSN 1530-9827. doi: 10.1115/1.4040131. URL https://doi.org/10.1115/1.4040131.

[51] K. D. Traxel, C. Groden, J. Valladares, and A. Bandyopadhyay. Mechanical properties of additively manufactured variable lattice structures of ti6al4v. *Ma-*

terials Science and Engineering: A, 809:140925, 2021. ISSN 0921-5093. doi: https://doi.org/10.1016/j.msea.2021.140925. URL https://www.sciencedirect.com/science/article/pii/S0921509321001945.

[52] S. Tsopanos, R. A. W. Mines, S. McKown, Y. Shen, W. J. Cantwell, W. Brooks, and C. J. Sutcliffe. The Influence of Processing Parameters on the Mechanical Properties of Selectively Laser Melted Stainless Steel Microlattice Structures. *Journal of Manufacturing Science and Engineering*, 132(4):041011, 07 2010. ISSN 1087-1357. doi: 10.1115/1.4001743. URL https://doi.org/10.1115/1.4001743.

[53] B. N. Turner, R. Strong, and S. A. Gold. A review of melt extrusion additive manufacturing processes: I. process design and modeling. *Rapid prototyping journal*, 20 (3):192–204, 2014.

[54] B. Vayre, F. Vignat, and F. Villeneuve. Metallic additive manufacturing: State-of-the-art review and prospects. *Mechanics Industry*, 13:89–96, 01 2012. doi: 10.1051/meca/2012003.

[55] X. Wang, M. Jiang, Z. Zhou, J. Gou, and D. Hui. 3d printing of polymer matrix composites: A review and prospective. *Composites Part B: Engineering*, 110:442–458, 2017. ISSN 1359-8368. doi: https://doi.org/10.1016/j.compositesb.2016.11.034. URL https://www.sciencedirect.com/science/article/pii/S1359836816321230.

[56] X. Wang, J. A. Muñiz-Lerma, O. Sánchez-Mata, M. Attarian Shandiz, and M. Brochu. Microstructure and mechanical properties of stainless steel 316l vertical struts manufactured by laser powder bed fusion process. *Materials Science and Engineering: A*, 736:27–40, 2018. ISSN 0921-5093. doi: https://doi.org/10.1016/j.msea.2018.08.069. URL https://www.sciencedirect.com/science/article/pii/S0921509318311377.

[57] S. Wickramasinghe, T. Do, and P. Tran. Fdm-based 3d printing of polymer and associated composite: A review on mechanical properties, defects and treatments. *Polymers*, 12(7), 2020. ISSN 2073-4360. doi: 10.3390/polym12071529. URL https://www.mdpi.com/2073-4360/12/7/1529.

[58] L. Xiao and W. Song. Additively-manufactured functionally graded ti-6al-4v lattice structures with high strength under static and dynamic loading: Experiments. *International Journal of Impact Engineering*, 111:255–272, 2018. ISSN 0734-743X. doi: https://doi.org/10.1016/j.ijimpeng.2017.09.018. URL https://www.sciencedirect.com/science/article/pii/S0734743X17304852.

[59] Z. Xiao, Y. Yang, R. Xiao, Y. Bai, C. Song, and D. Wang. Evaluation of

topology-optimized lattice structures manufactured via selective laser melting. *Materials Design*, 143:27–37, 2018. ISSN 0264-1275. doi: https://doi.org/10.1016/j.matdes.2018.01.023. URL https://www.sciencedirect.com/science/article/pii/S0264127518300303.

[60] C. Yan, L. Hao, A. Hussein, P. Young, and D. Raymont. Advanced lightweight 316l stainless steel cellular lattice structures fabricated via selective laser melting. *Materials Design*, 55:533–541, 2014. ISSN 0261-3069. doi: https://doi.org/10.1016/j.matdes.2013.10.027. URL https://www.sciencedirect.com/science/article/pii/S0261306913009540.

[61] W. Zhang, A. Chabok, B. J. Kooi, and Y. Pei. Additive manufactured high entropy alloys: A review of the microstructure and properties. *Materials Design*, 220:110875, 2022. ISSN 0264-1275. doi: https://doi.org/10.1016/j.matdes.2022.110875. URL https://www.sciencedirect.com/science/article/pii/S026412752200497X.

[62] T. Zhong, K. He, H. Li, and L. Yang. Mechanical properties of lightweight 316l stainless steel lattice structures fabricated by selective laser melting. *Materials Design*, 181:108076, 2019. ISSN 0264-1275. doi: https://doi.org/10.1016/j.matdes.2019.108076. URL https://www.sciencedirect.com/science/article/pii/S0264127519305143.

A | Appendix A

- **As-build**- Hatch Angle Effect- Comparison of Series A and C:

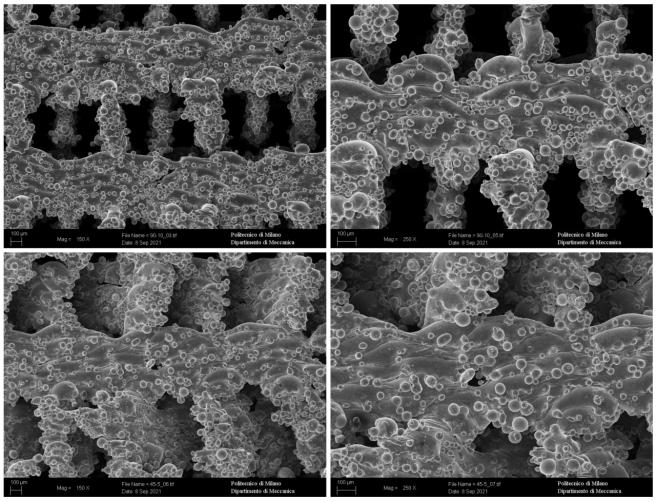

(a)

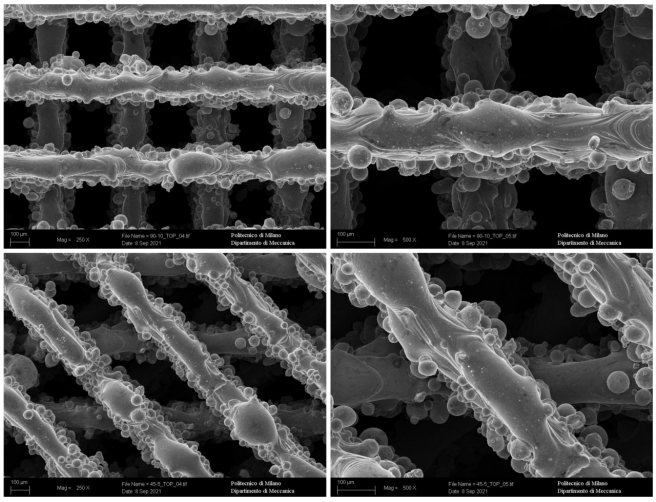

(b)

Figure A.1: Hatch Angle effect Sets A_1 with 90° on top and C_1 in the bottom with 45° both with 600 μm/s scanning speed (a) Lateral view, (b) Top view.

- **As-build**- Scanning speed effect:

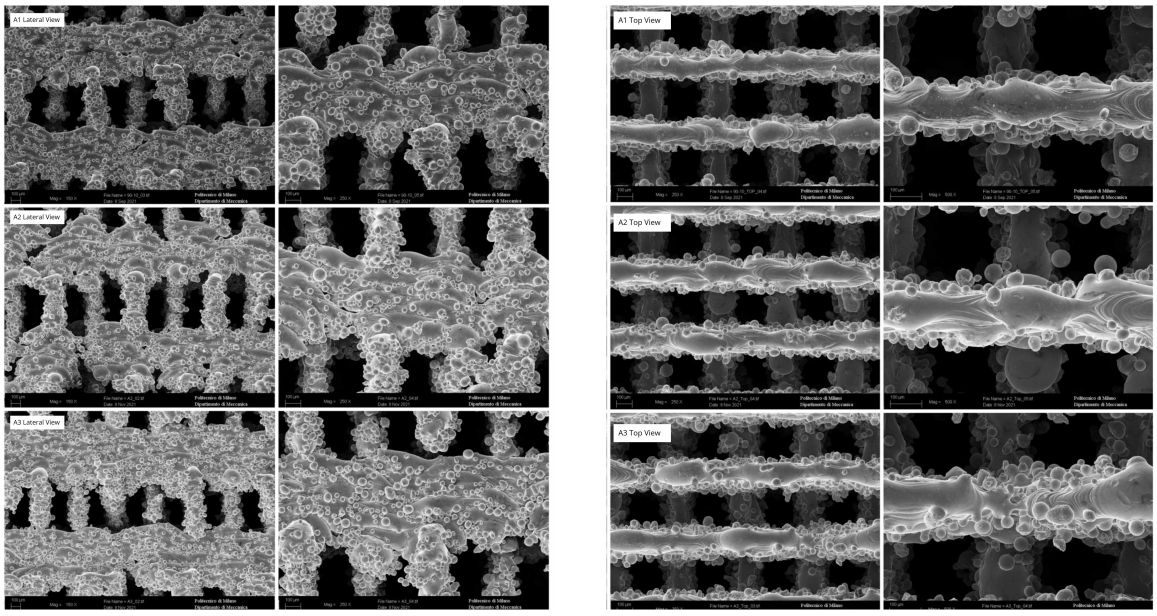

(a) (b)

Figure A.2: **Serie A** - Asbuilt SEM: A_1 (600 μm/s), A_2 (550μm/s), A_3 (500μm/s) (a) Lateral view, (b) Top view.

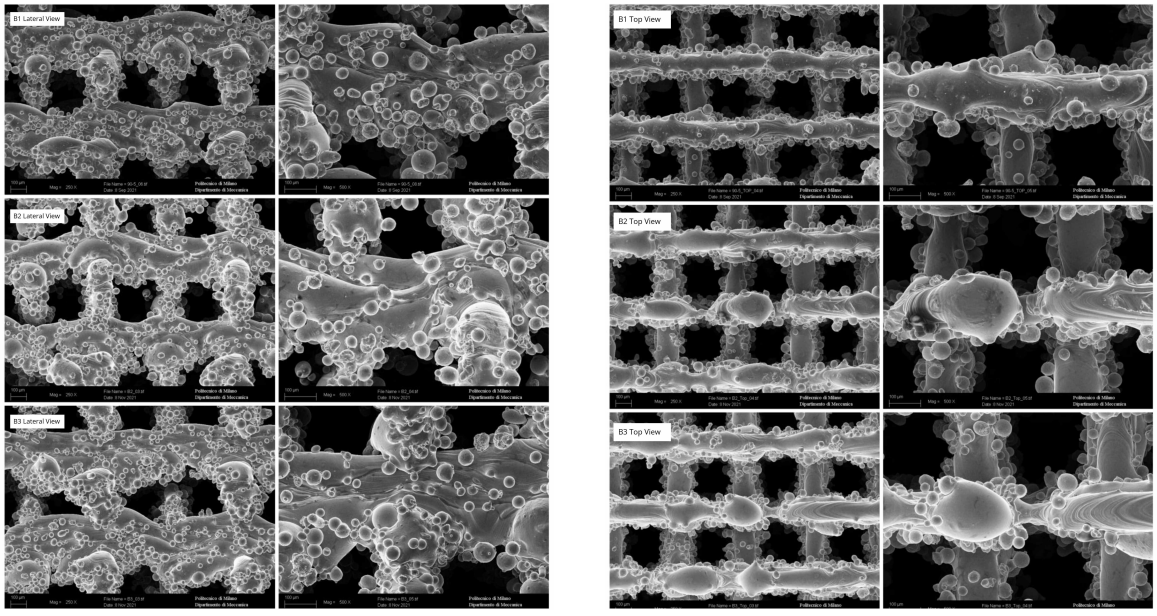

(a) (b)

Figure A.3: **Serie B** - Asbuilt SEM: B_1 (600 μm/s), B_2 (550μm/s), B_3 (500μm/s) (a) Lateral view, (b) Top view.

- **As-build**- Layer Effect- Comparison of Series A and B:

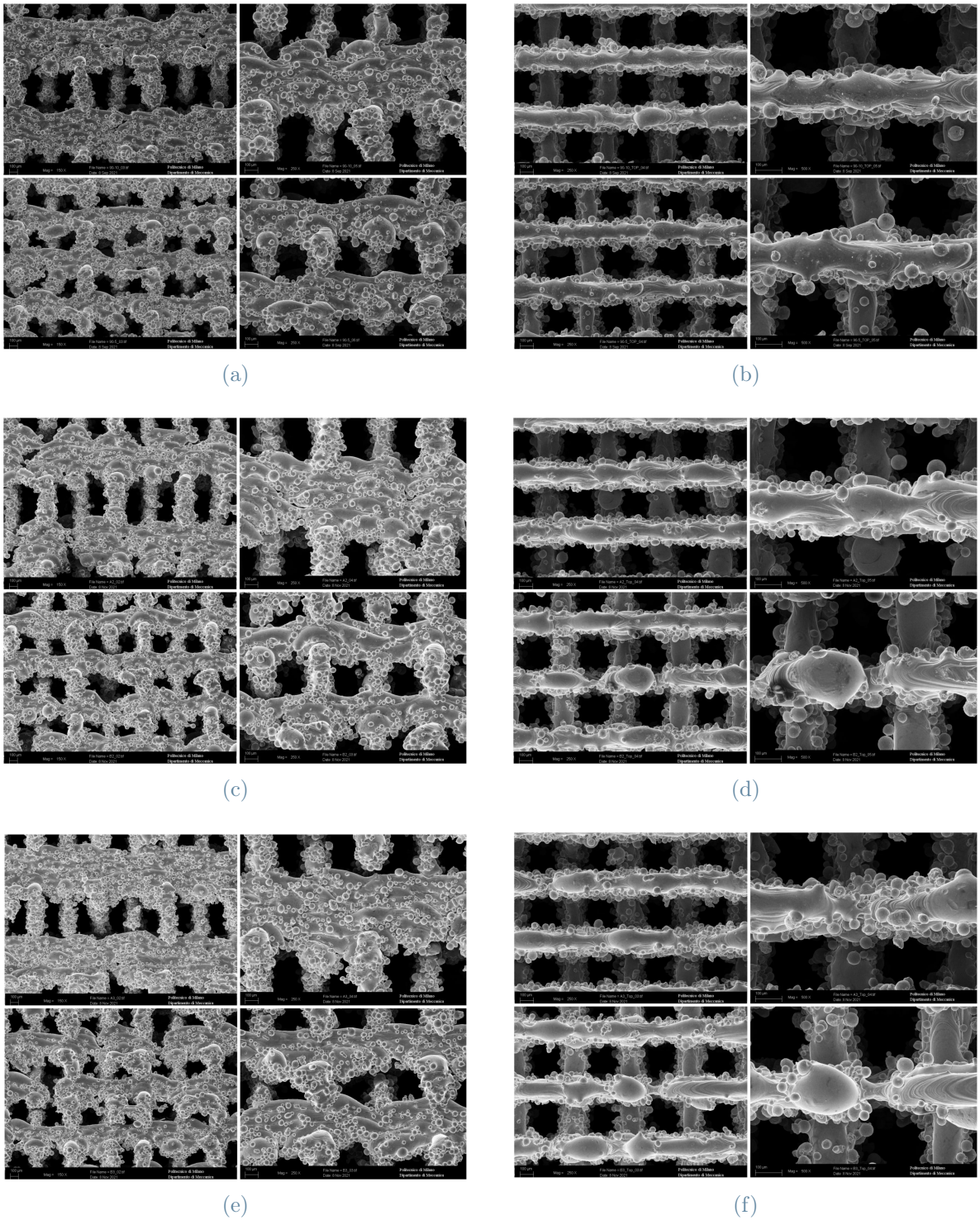

(a) (b) (c) (d) (e) (f)

Figure A.4: Layer Effect SEM $A_1 - B_1$ (600 μm/s):(a) Lateral view (b) Top view, $A_2 - B_2$ (550 μm/s): (c) Lateral view, (d) Top view, $A_3 - B_3$ (500 μm/s): (e) Lateral view, (f) Top view.

Compression Test, Speed Effect, Serie A:

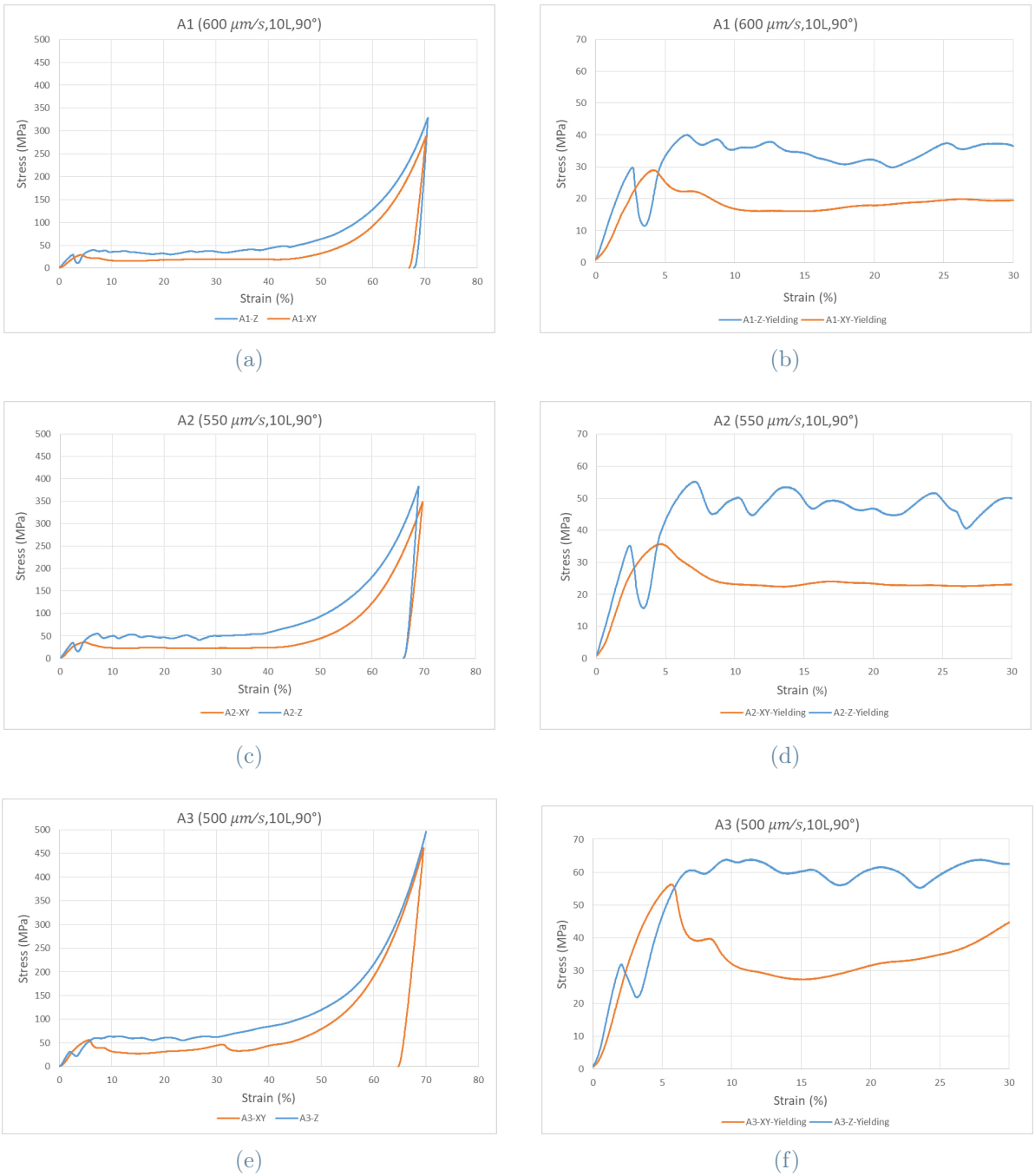

Figure A.5: Speed Effect Compression Test Serie A

Compression Test, Speed Effect, Serie B:

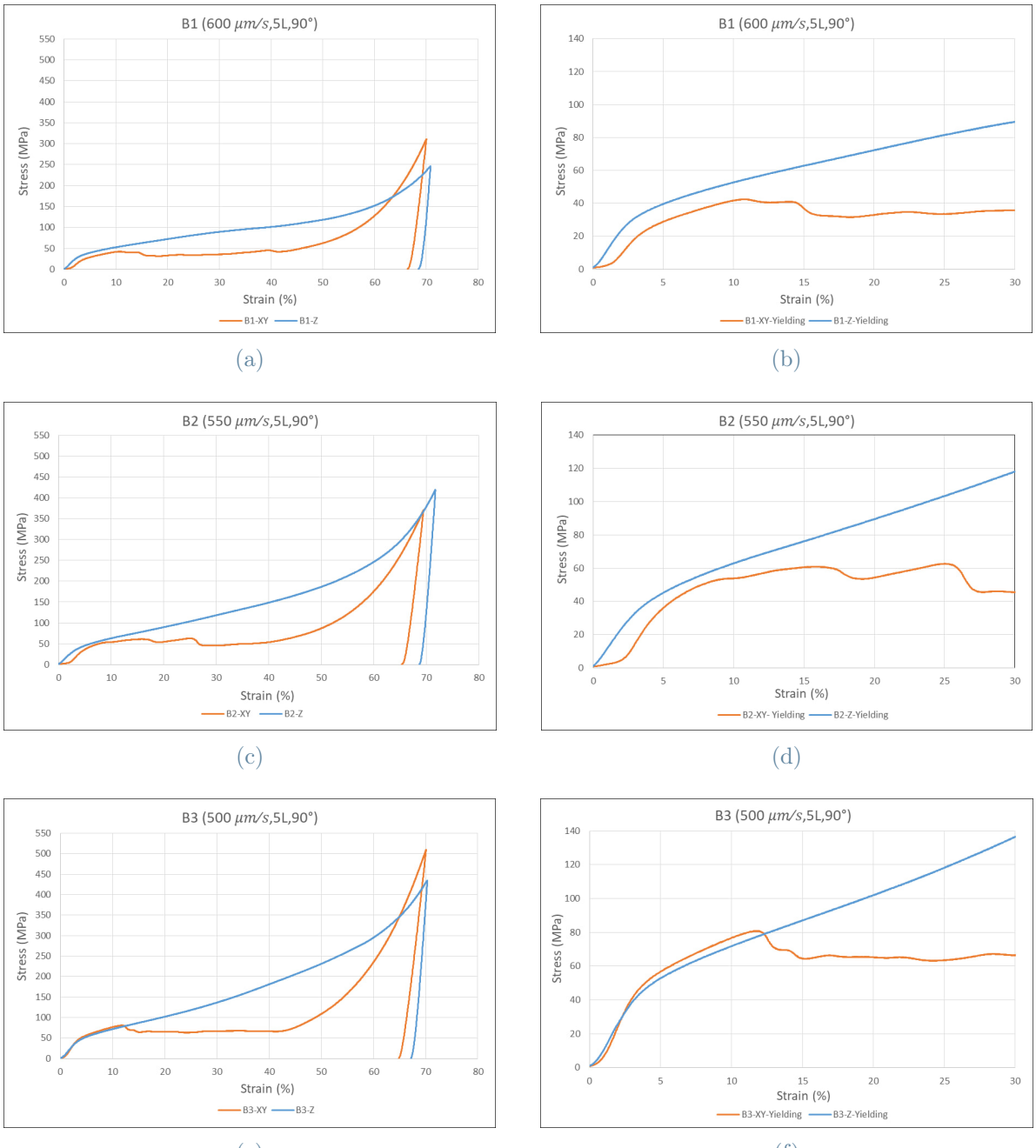

Figure A.6: Speed Effect Compression Test Serie B

Compression Test along Z direction (Building direction), Layer Effect, Series A and B:

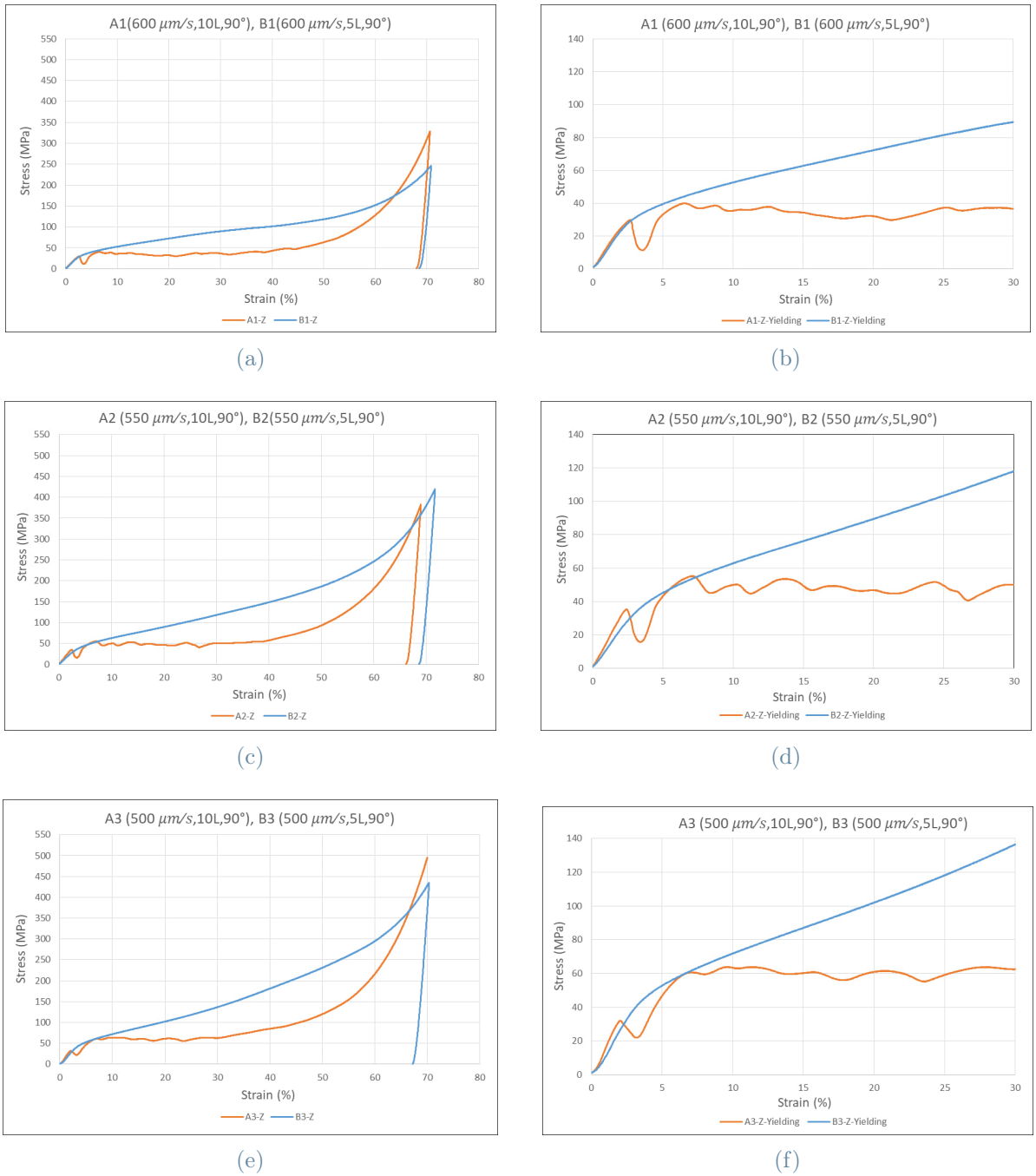

Figure A.7: Layer Effect on Compression Test along Z axis for Series A and B

Compression Test along X/Y direction (Lateral Surfacce), Layer Effect, Series A and B:

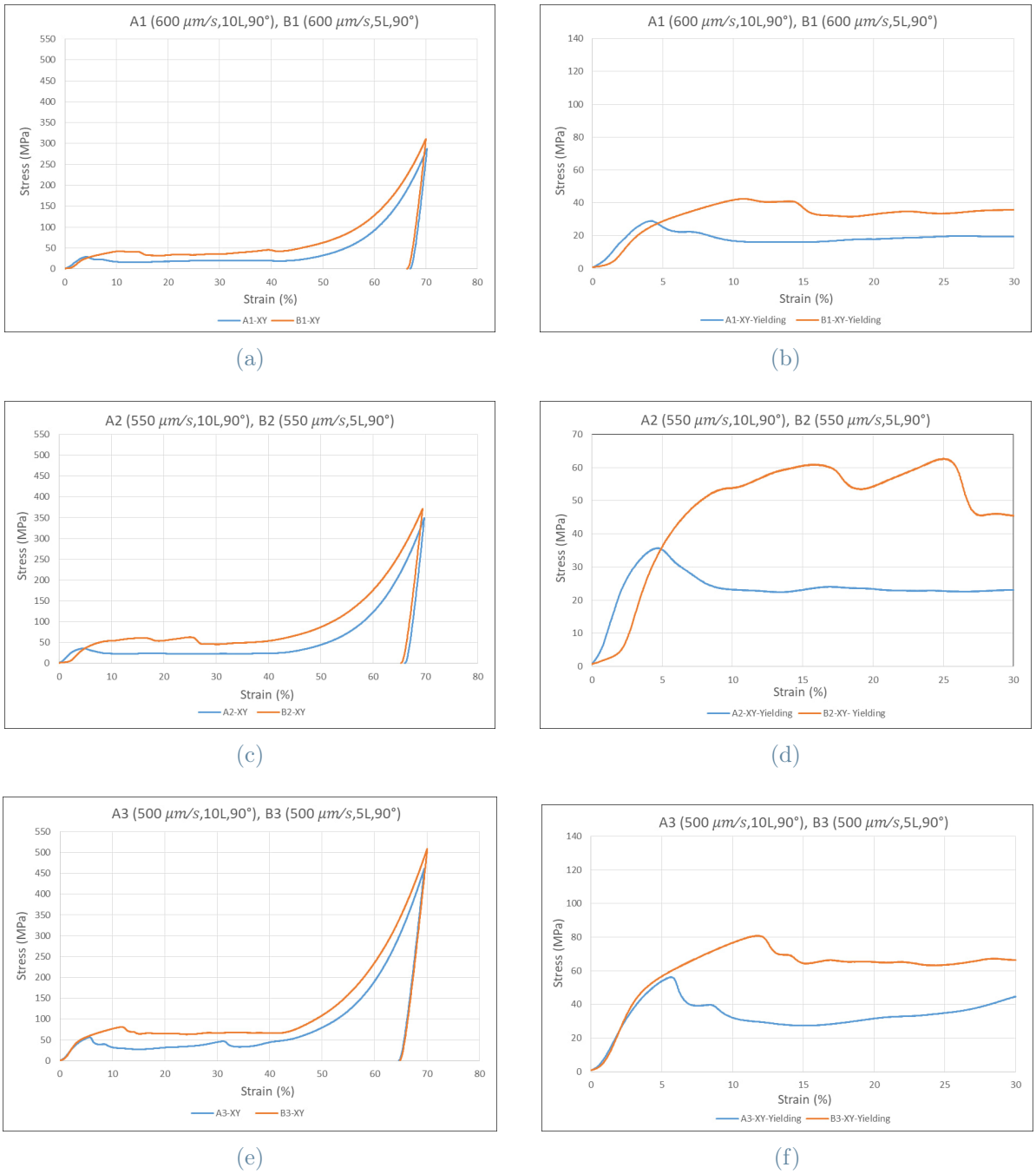

Figure A.8: Layer Effect on Compression Test along X/Y axis for Series A and B

Compression Test along Z direction 30% of initial height (DIC Test), series A and B:

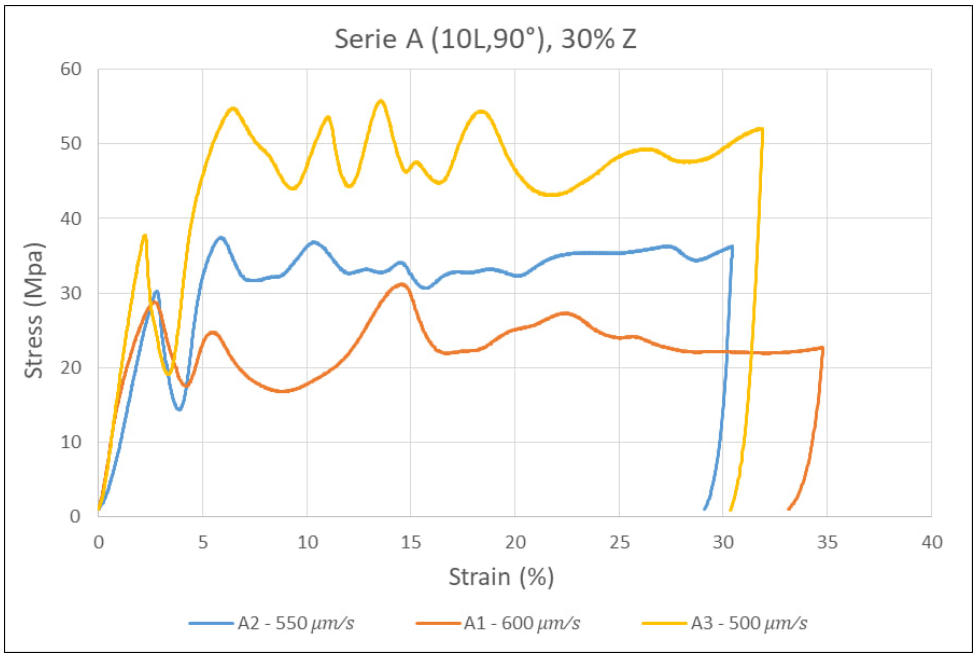

Figure A.9: Serie A 30% Compression along Z Direction

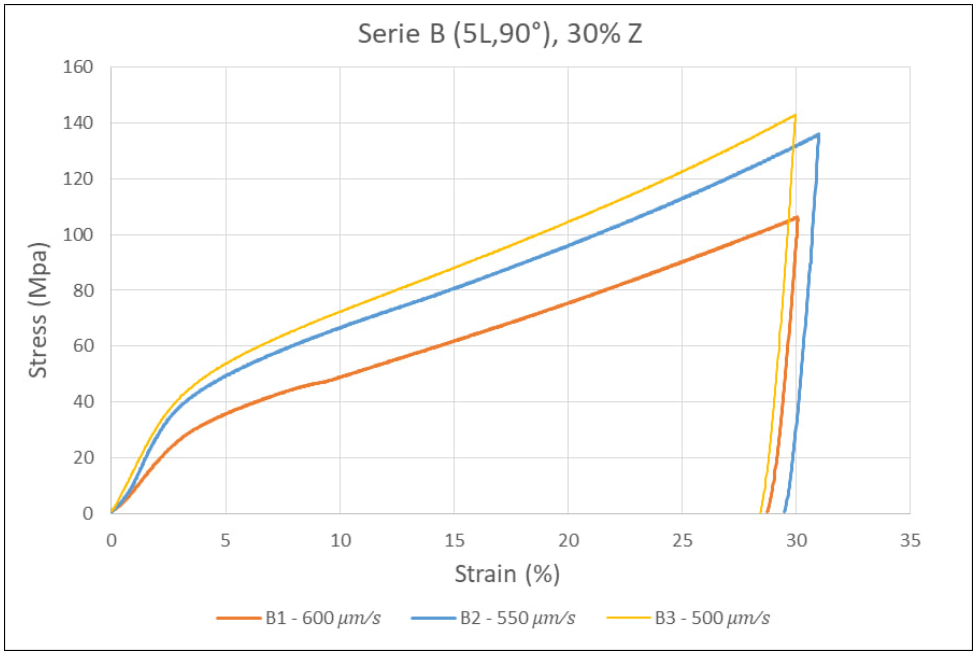

Figure A.10: Serie B 30% Compression along Z Direction